A Test setup for characterizing high-temperature thermoelectric modules

Satchit Mahajan

A Test Setup for Characterizing High-Temperature Thermoelectric Modules

by

Satchit B. Mahajan

A Thesis Submitted in Partial Fulfillment of the Requirements for the Degree of

Master of Science in Mechanical Engineering

Approved by:

Dr. Robert J. Stevens
Department of Mechanical Engineering

_____
(Thesis Advisor)

Dr. Satish G. Kandlikar
Department of Mechanical Engineering

_____
(Committee Member)

Dr. Michael G. Schrlau
Department of Mechanical Engineering

_____
(Committee Member)

Dr. Wayne W. Walter
Department of Mechanical Engineering

_____
(Department Representative)

Sustainable Energy Systems Lab
Department of Mechanical Engineering
Kate Gleason College of Engineering
Rochester Institute of Technology
July 2013

Abstract

With the tremendous growth in demand for energy resources, there is a growing need to adopt alternative energy technologies, including ones that tap renewable energy sources as well as use non-renewable sources more efficiently. Thermoelectric energy generation is one such emerging technology. Thermoelectrics can convert waste heat from various sources—significantly, many industrial processes as well as vehicles—directly into electrical power. Thermoelectric devices can generate power when a temperature difference is applied across them. Major barriers to mainstream adoption of thermoelectric devices are their low efficiency and high cost. These are mostly limited by the properties of the constituent materials of the device(s) and the operating temperatures. In the past decade there have been significant advancements in thermoelectric materials that can be used at higher temperatures. The properties of thermoelectric materials are temperature dependent, and may also vary from bulk material to device level. Right now, devices with higher working temperatures are not available. According to feedback from laboratories working on high-temperature modules, the next stage in the development of thermoelectric devices would go up to 650°C.

The main focus of this project is to design and develop a test stand to evaluate the properties of all such high-temperature devices. One of the critical challenges in testing modules, especially at high temperatures, is being able to accurately control and measure heat rates transferred across a module. Many of the current characterization techniques are limited to solely measuring the electrical response and ignoring the heat transfer. A new testing technique, "rapid steady state," was developed, which is able to accurately measure the three key characteristic properties—the Seebeck coefficient, electrical resistance, and thermal conductance—of a thermoelectric module

over temperature ranges from 50 to 650°C. To ensure isothermal surfaces and minimize heat rate errors, a primary heater is encased in a guard heater. Rapid pulsed electronic loading allows for rapid voltage-current scans while avoiding thermal drift. The thermal conductivity of a reference material is used to validate the performance of the guard heater assembly and heat-monitoring setup.

Acknowledgements

First and foremost I offer my sincere gratitude to my adviser Dr. Stevens for his knowledge, understanding and most importantly patience while guiding me. He had faith in me even at times when I did not. This project would never have been completed had it not been for his help. I am not sure how many graduate students are fortunate enough to be given the freedom that you gave me. For everything you've done for me, Dr. Stevens I thank you. I could not have wished for a better adviser, as a teacher and a person.

I would like to thank NYSP2I for the Research and Development grant which helped fund the project. I would also like to thank the members of my thesis committee for all their input and ideas while designing the project. I want to thank Dr. Kandlikar for providing me my first exposure to experimental testing and Dr. Schrlau for his ideas and insights.

I would like to thank Jan Maneti and especially Rob Kraynik at the Mechanical Engineering machine shop for their immense help in building the test stand. I would be lost without their help. I am also thankful to Dr. Hensel and everyone at the ME office for their guidance and support during my time here at RIT. A special thank you goes to Dhruvang and Reggie, my lab members for all of their help in completing my project and Sheryl who helped me polish my thesis.

Finally, I want to thank my family, for always believing in me. They have always been a pillar of unwavering support and gave me the strength to continue in the face of hardships. I hope that one day I become at least half the person you thought I would be. I want to also thank my friends Aditya and Zeeshan, my days in Rochester would be colorless without you. And last I want to thank my girlfriend Devyani, for being my closest friend, confidant and my silver lining. I cannot imagine being where I am now without your support.

Table of Contents

List of Figures

List of Tables

Nomenclature

Symbol	Parameter
A	Surface Area, m^2
I	Current flowing through the leg pair or module, A
K	Thermal conductance, W/K
$K*$	Coverage Factor
P	Power generated by a leg pair or module, W
Q	Heat rate, W
R	Electrical resistance of a module, Ω
R_{TH}	Thermal Resistance, K/W
T	Temperature, K or °C
U	Uncertainty in a measured quantity, %
V	Voltage across a leg pair or module, V/K
ZT	Figure of merit, dimensionless

Symbol	Parameter
α	Seebeck coefficient, V
β	Thompson coefficient, W/mAK
ΔT	Temperature difference across the module, °C
η	Module efficiency, %
λ	Thermal conductivity, W/mK
π	Peltier coefficient, W/A
ρ	Electrical resistivity, Ωm
σ	Standard deviation in measurement, takes dimension of measured quantity

Subscript	Parameter
$\overline{()}$	Averaged result for tests carried out using positive and negative current
$(')$	Property measured during negative current test
Al	Property of aluminium block
C	Cold side, K or °C
CP	Cold plate properties
H	Hot side, K or °C
L	Property evaluated after applying electrical loading
OC	Open circuit
SC	Short circuit
TEM	Thermoelectric module
am	Property measured at ambient condition
$bypass$	Properties of thermal bypass
cer	Properties of ceramic plate
eq	Equivalent
i	Property along insulation
int	Properties of the interconnect material
mod	Module property
n	Property of a n-leg
o	Seebeck component
p	Property of a p-leg
p,n	Overall property over p-leg and n-leg
r	Resistive component
r	Component of Random uncertainty
s	Component of Systematic uncertainty
$shunt$	Properties of Shunt resistor
t	Uncertainty component of temperature

v Uncertainty component of voltage

λ Module conduction losses

Chapter 1.   Introduction to Thermoelectrics

1.1 Introduction

In the year 2008, total world requirement for energy was 500 quadrillion BTU [1], approximately 50% of which was dumped into the environment in the form of waste heat. Waste heat is heat generated in a process by way of fuel combustion or chemical reaction, then "dumped" into the environment even though it could still be reused for some useful and economic purpose. In the industrial sector 20–50% of the energy input is lost as waste heat [2].

The energy lost in waste heat cannot be fully recovered because it is often low-grade heat and dispersed. With the world's population growing at the rate of 1.1% per year, the energy requirement is expected to double by 2020 [3]. Coupled with this is the rapid depletion of fossil fuel global reserves. There is a widespread need for alternative sources of energy and energy conversion technologies.

The use of thermoelectrics is potentially one such opportunity. Thermoelectric modules (TEMs) can generate power when placed between a heat source and a heat sink. TEMs are increasingly finding application in waste heat regeneration such as automobiles, industrial processes, and power plants. This is a process wherein heat energy that would have been dissipated into the atmosphere is utilized for generating power. Thermoelectrics are also environmentally friendly and generate no emissions.

Another important application of thermoelectrics is as Peltier coolers. These are extensively used in electronic devices that have specified cooling requirements. Precise temperature control and the abbility to cool below atmospheric temperatures make them an ideal candidate in computer electronics.

1.2 Advantages

There are many advantages to using thermoelectrics. These are summarized as follows:

No moving parts: Thermoelectrics can generate electricity directly without any moving parts so they are virtually maintenance free. In fact, one of the first applications of thermoelectrics was and still is to power deep space probes using radioisotopes as heat sources. These systems have functioned for decades with no maintenance [4].

Small size and weight: The overall thermoelectric cooling system is much smaller and lighter than a comparable mechanical system. In addition, a variety of standard and special sizes and configurations is available to meet strict application requirements. Thermoelectrics are modular and can be used for a range of applications. Current systems operate over a wide range, from mW to KW.

High reliability: Thermoelectrics exhibit very high reliability due to their solid state construction. Although reliability is somewhat application dependent, the life of typical thermoelectric coolers is rated to be greater than 200,000 hours. The actual life of the modules may be much longer. In fact, the modules used by NASA in their long-range satellites are still functioning with no maintenance even after several decades in operation.

Operational conditions: Thermoelectrics can be used in any orientation and adverse environments, as well as over a large range of temperatures. This makes them ideal for applications based on waste heat utilization.

Transient heat sources: TEMs can be used in applications where the heat source is not constant. This is a huge benefit in applications like waste heat utilization of automobile exhaust, where the heat source is variable and where other power recovery technologies are not feasible.

1.3 Disadvantages

Though thermoelectrics have many advantages, there are drawbacks in the technology. These are summarized as:

Low efficiency: This is a major drawback facing the thermoelectric industry. Current off-the-shelf thermoelectric devices efficiencies are typically in the range of 2–8%. Thermoelectrics have been mainly confined to low-energy applications or where the heat source is free, and are unable to compete for large-scale power generation applications.

Susceptibility to shock loading: Thermoelectrics can handle transient heat loads, but the life of thermoelectric devices decreases considerably after receiving thermal shock loading. In the case of mechanical loading, they can withstand up to 1000 psi but only to the standard loading—around 200psi—in compression. They are weakest in shear loading [5].

Cost: Owing to the novelty of the technology, the cost per watt of the device is much higher than with the conventional power generation technologies. As newer and cheaper materials with higher power ratings are developed and manufacturing techniques are improved, the cost per unit power is certain to decrease.

1.4 Applications

Peltier cooling

Peltier cooler is a thermoelectric operating in heat pumping mode. As current is passed through a thermoelectric device, a temperature difference develops across it. The cold side of the device is thermally coupled with the component being cooled, while the hot side of the device needs to be cooled externally using a heat sink or forced convection. Peltier coolers have an important role in electronics, especially in cases where conventional cooling systems cannot be implemented. Their small size, silent operation, and the ability to maintain the temperature accurately make them especially attractive for use as CPU coolers [6].

Thermoelectrics are also used in microelectronics where localized cooling is required. Gupta et al. [7] investigated the operation of a ultrathin thermoelectric cooler for cooling of localized hot spots on a chip. They found the device to be very effective for low-current operations. However, as the current increased over 4A, back heat flow due to the temperature difference generated countered the cooling effect.

Other niche applications include refrigeration, in wine coolers, car refrigerators, and beverage can coolers. Thermoelectrics are also used in NEMA enclosures to regulate temperatures and applications where cryogenic cooling is required.

Power generation

While thermoelectrics are not currently used in a wide range of power generation applications, their most important application will undoubtedly be in power generation. An important factor is that TEMs can utilize waste heat from a large number of processes for power generation. The

energy conversion efficiency is low compared to other power conversion technologies, which is the main hurdle to be crossed before thermoelectric moves from a niche to mainstream power generation applications.

Low-power applications include powering watches, calculators, and remote sensing. The "Thermic" [8] designed by Seiko used body heat for its working. Thin film micro generators producing power at milliwatt and microwatt level are used in electronic applications. Kim [9] fabricated one such device generating 4.3nW/K. These can be coupled easily with photovoltaic cells as well.

Thermoelectrics have found application in high-power generation as well, but the major drawback is the low efficiency. They are mainly used in waste heat applications, where the supply of heat is free. Commercially, modules generating up to 550W are available. Standalone thermoelectric generators are mainly used in extreme environments.

Thermoelectrics have been critical in enabling continuous powering of deep space probes where the use of solar and other power generation technologies is not feasible. For example, thermoelectrics are used in radioisotope thermoelectric generator (RTG) where power is generated using heat from the decay of radioactive material, like plutonium-238. Over the last four decades, 26 missions have used RTGs. The RTG installed on the Mars rover is expected to operate for at least one Mars year or 687 Earth-days.

1.5 Background and Theory

Thermoelectric devices are basically solid state devices that can convert energy from heat to electricity or vice versa. Devices are normally made up of semiconductor materials, the most

common being bismuth telluride. A typical configuration of a thermoelectric module consists of many leg pairs made of semiconductor pellets, joined together using contact tabs made of high conductivity materials.

Seebeck Effect

The principle behind the working of the thermoelectric module is the Seebeck effect. In 1821 Thomas Johann Seebeck observed that when two dissimilar metals with junctions at different temperatures are connected in a circuit, a magnetic needle would be deflected. Seebeck initially attributed this phenomenon to magnetism. However, it was quickly realized that it was an induced electrical current that deflects the magnet [10]. In a thermoelectric module, the two dissimilar conductors are connected electrically in series and thermally in parallel. When the two junctions are maintained at temperatures T_H and T_C respectively, and $T_H > T_C$, an open circuit electromotive force (V) is developed between the junctions, as seen in Fig. 1.1.
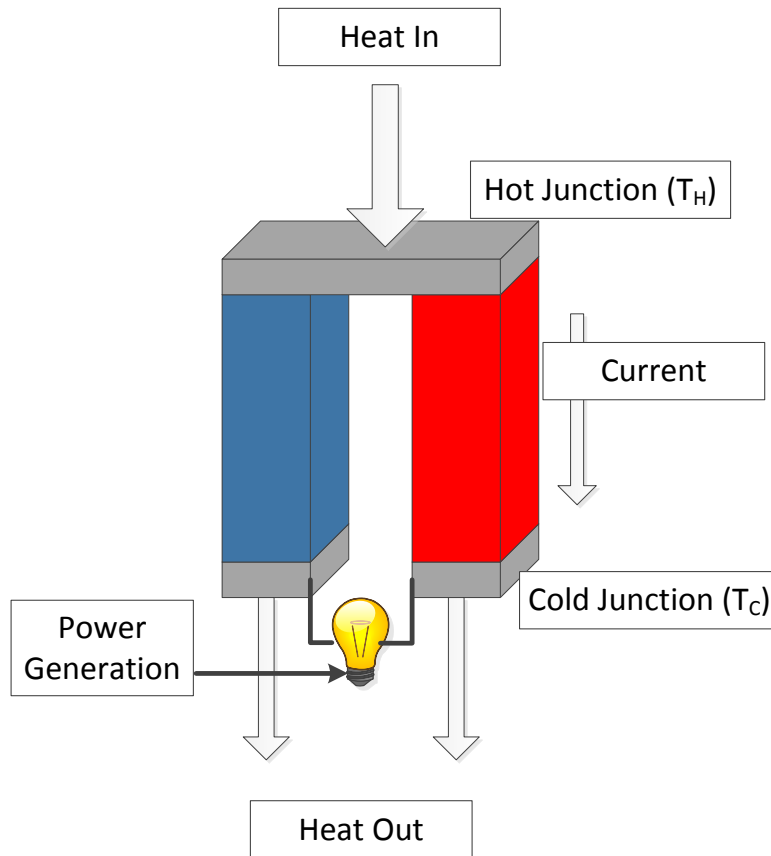
Figure 1.1: Seebeck Effect

The voltage produced is proportional to the temperature difference between the two junctions. This is given by:

$$V = \alpha(T_H - T_C) \tag{1.1}$$

The proportionality constant, α, is the difference between the Seebeck coefficients of the two materials forming the junction. This is known as the overall Seebeck coefficient, and often referred to as the thermoelectric power or thermo power. The Seebeck voltage does not depend on the distribution of temperatures along the material between the junctions. This phenomenon is what is used to measure temperatures using thermocouples.

Peltier Effect

The converse of the Seebeck effect was discovered independently by Jean-Charles Peltier in 1834. When current is made to flow through a junction of dissimilar materials, a rate of heating occurs at one junction while heat is absorbed at the other junction [10]. Although it is the converse of the Seebeck effect, Peltier failed to make the connection when he discovered the phenomenon. In Fig. 1.2 it can be seen that when a current is passed through the junction, one side is heated and the other is cooled.
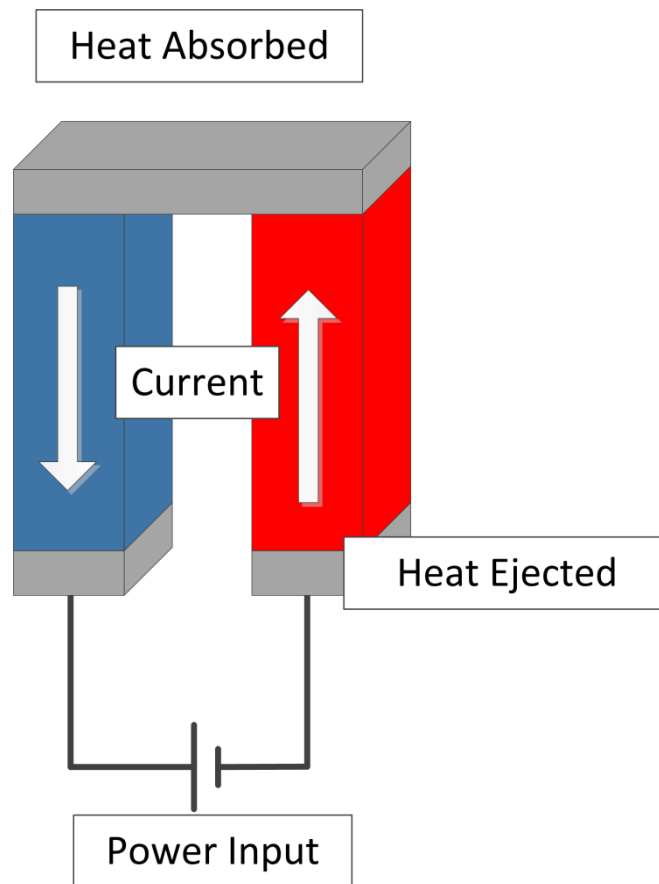
Figure 1.2: Peltier Effect

The Peltier co-efficient is defined as:

$$Q = \pi I \tag{1.2}$$

where Q is the rate of heating or cooling and I is current passing through the junction. The Peltier coefficients represent how much heat current is carried per unit charge through a given material [10].

Thomson effect

The Thomson effect was observed by Sir William Thomson in 1851. It relates to the rate of heating or cooling resulting from the passage of current through a current-carrying conductor with a temperature gradient applied across it, and is defined as the evolution or absorption of heat when electric current passes through a circuit composed of a single material that has a temperature difference along its length. If (ΔT) is the temperature difference generated across a conductor carrying current (I), then heat generated per unit length ($\bar{Q}$) is given by

$$\bar{Q} = \beta I \Delta T \tag{1.3}$$

where β is the Thomson coefficient.

The Kelvin Relationships

Lord Kelvin developed relationships between the above three thermoelectric coefficients. The relationships were tested for many thermoelectric materials and it is assumed that they hold true for all materials used in thermoelectric applications.

The relationships can be written as:

$$\alpha = \pi/T \tag{1.4}$$

$$\frac{d\alpha}{dT} = \frac{\beta}{T} \tag{1.5}$$

where T is the absolute temperature.

1.6 Significant Parameters

The most important parameters in a thermoelectric material are the "Seebeck coefficient" and "figure of merit." The Seebeck coefficient is a measure of the transported entropy per charge carrier. The figure of merit is a non-dimensional measure of performance of the material. It gives the theoretically possible maximum efficiency of a thermoelectric.

The figure of merit *(ZT)* is expressed as

$$ZT = \frac{\alpha^2 \sigma}{k} T \tag{1.6}$$

The figure of merit varies directly with the Seebeck coefficient and electrical conductivity and inversely with thermal conductivity. An increase in electrical conductivity reduces the losses caused due to Joule heating. A decrease in the thermal conductivity would limit the amount of heat passing through the module without being converted into power. The theoretical maximum efficiency of thermoelectric material depends on the figure of merit, and there are no theoretical upper limits for the figure of merit. Most materials currently used have thermoelectrics of approximately one or less. Figure 1.3 shows the relationship between the TZ values of different materials and temperature.
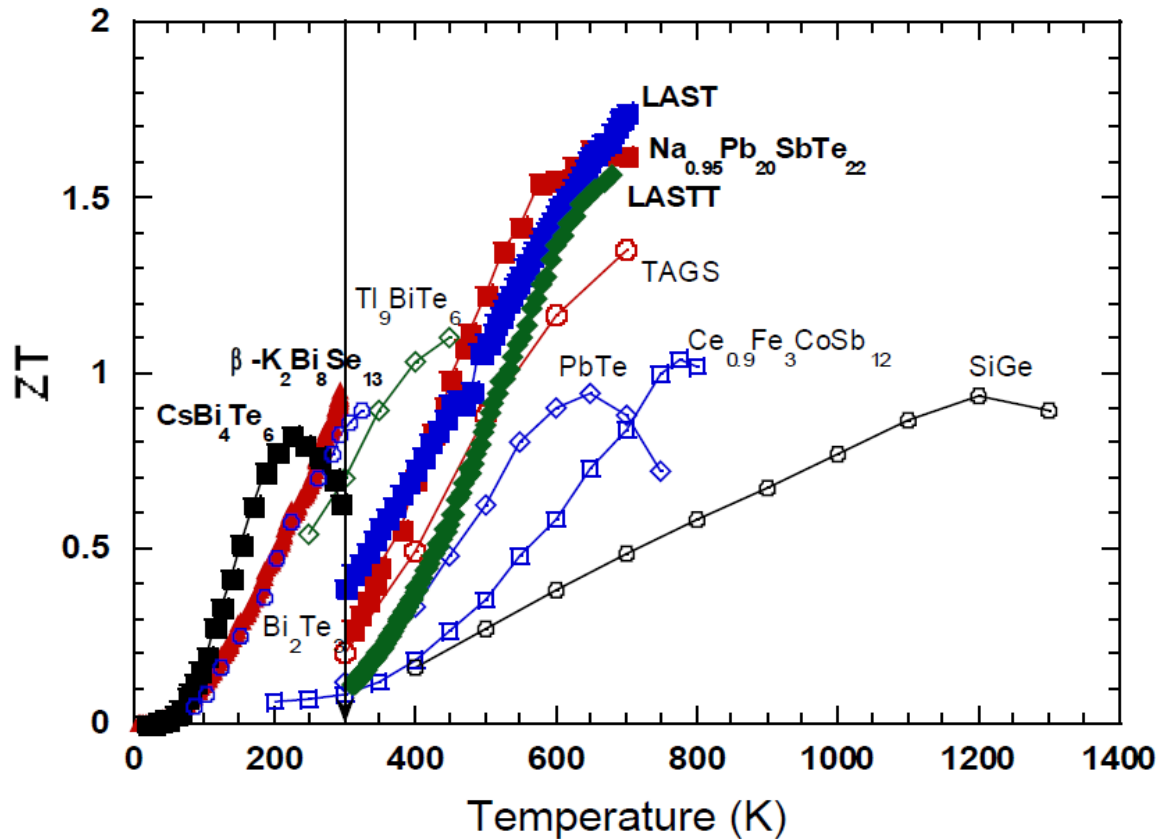
Figure 1.3: Variation of ZT with temperature for different materials [11]

Though the *ZT* value is the measure of a Carnot performance, it does not exactly translate to the module efficiency. The efficiency actually is based on the amount of heat flowing through the module itself, not the amount of heat available. A clear trend is observed, where ZT for a given material increases as its temperature increases. Currently, the best thermoelectric materials developed in the lab have values between one and three[11], but these are yet to be used in practical devices.

1.7 Thermoelectric Materials

Low efficiency of the thermoelectric modules is a significant drawback hindering the use of thermoelectric modules in everyday applications. As seen in the previous section, a higher ZT

begets better efficiency. Hence, extensive research is being carried out to find a material with high ZT and to improve the ZT values of existing materials.

In the literature today, the best materials currently used in most thermoelectric devices have ZT values between zero and three. Some of the most popular materials have been bismuth telluride ($Bi_2 Te_3$ system) and silicon-germanium combinations. Much research has been carried out on these materials and the scope of improvement is small. Consequently, newer and better materials are being investigated, primarily by nano-engineering materials. Figure 1.4 below shows a plot of ZT as a function of temperature for the various nanostructured bulk materials being developed in labs. There have been tremendous improvements in thermoelectric materials, primarily driven by improved understanding of thermal transport at the nanoscale and improved nanostructure fabrication techniques [12].
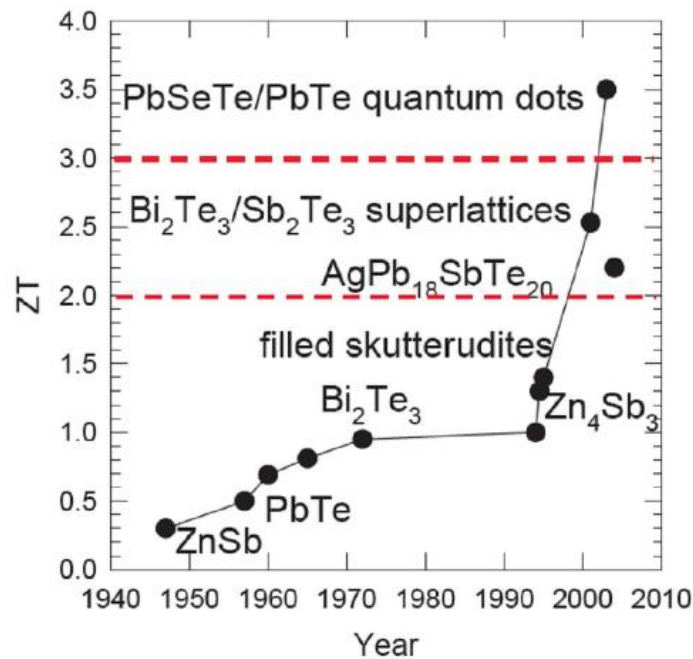
Figure 1.4: Development of ZT since 1940 [13]

1.8 TEM Construction and Configuration

A typical thermoelectric module is made of multiple leg pairs, where each leg pair is made of two semiconductor materials made from p and n type semiconductor materials. The combination of these multiple leg pairs is held together by a top and bottom plate, typically made of a ceramic-like aluminum nitride (AIN). This ensures electrical insulation and structural support. The leg pairs are connected in such a way that they are in series electrically and in parallel thermally. The pellets, tabs, and ceramic plates form a layered configuration, as seen in Fig 1.5.
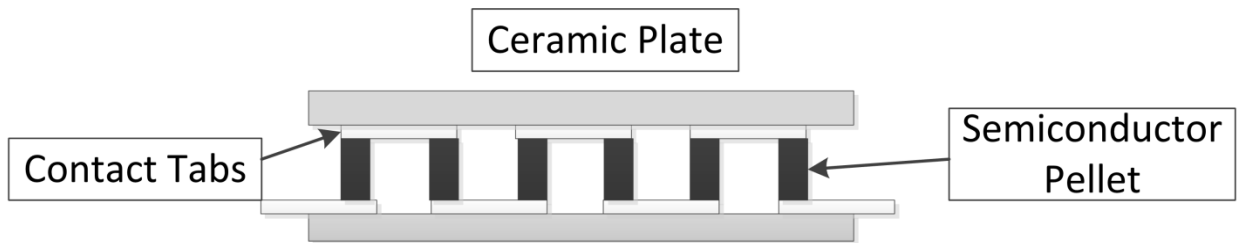
Figure 1.5: Typical thermoelectric module in heat pumping configuration

Generally the individual legs are made of a single material. But as newer technologies are developed, leg pairs made up of multiple materials are being developed.
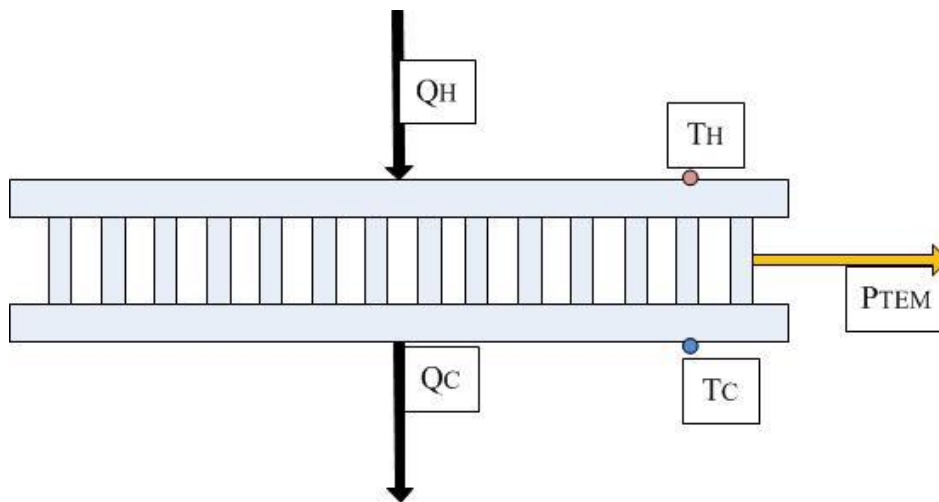
Figure 1.6: A typical TEM in power generation configuration

Figure 1.6 shows a module in a power generation arrangement where heat enters the hot side of the module and is rejected from the cold side of the module. The most commonly used approach for calculating power generation is a one-dimensional approach. Using the model developed by Angrist [14] , the heat flow into the hot side of the module, Q_H, is expressed as

$$Q_H = I\alpha_{p,n}T_H + K(T_H - T_c) - I^2\,R/2 \tag{1.7}$$

where I is the current flowing through the module and $\alpha_{p,n}$ is the overall Seebeck coefficient, which is the product of the difference of the individual Seebeck coefficients of the two constituent materials and the number of leg pairs. T_H and T_C are the temperatures on the hot and cold sides of the module. K is the thermal conductance, which is the inverse of the thermal resistance across the entire device. This includes the thermal resistance of the legs as well as the thermal resistance of the substrate and thermal leakage across the device. R is the electrical resistance, which includes the leg and metal connector contact resistance. The heat flow out of the module (Q_C) is given by

$$Q_C = I\alpha_{p,n}T_C + K(T_H - T_c) - I^2\,R/2 \tag{1.8}$$

These expressions are developed by solving the heat diffusion equation in the device and applying a fixed temperature and the Peltier effect model at the surfaces. From energy conservation, the electrical power output of a thermoelectric module is expressed as

$$P_{TEM} = (Q_H - Q_C) \tag{1.9}$$

$$P_{TEM} = I\alpha_{p,n}(T_H - T_c) - I^2R \tag{1.10}$$

The efficiency of the module can be expressed as the ratio of the power output to the heat input, and is given as

$$\eta = \frac{P_{TEM}}{Q_H} \tag{1.11}$$

$$\eta = \frac{I\alpha_{p,n}(T_H - T_c) - I^2 R}{I\alpha_{p,n}T_H + K(T_H - T_c) - I^2R/2} \tag{1.12}$$

Most of the modules commercially available today can be classified as "low temperature." Research conducted on low-temperature waste heat recovery systems [15–19] has demonstrated the potential viability of thermoelectric systems. However, the primary reasons that thermoelectrics have not been adopted in mainstream applications are low efficiency and high cost. The efficiency of the module generally increases as the temperature difference applied across it increases. To achieve improved efficiency, there is interest in developing high-temperature materials to enable operation of modules at higher temperature differences than those reached with typical BiTe-based devices.

In conclusion, over the past decade there have been significant advancements in thermoelectric materials that can be used at high temperatures [20–24]. More recently, TEMs based on these materials have also been developed. Thus, developing the capability to test high-temperature thermoelectric devices is desperately needed to support the development of ceramic oxide-based thermoelectrics. Such capabilities do not currently exist. The testing system proposed in this thesis will provide the ability to demonstrate proof of concept of the next generation of thermoelectric devices using oxides and other high-temperature materials, provide experimental data to validate and improve device models, and characterize devices for system design

purposes. The testing capabilities will also allow for an efficient means of optimizing devices

and a better understanding of the impact of various material interface and fabrication options.

Chapter 2.   Testing Approaches

In the field of thermoelectrics, there are two categories of testing. The first is testing of materials, and the second is testing of modules or devices. A wealth of research on the testing and characterization of thermoelectric materials exists. However, little has been done to test complete power generation modules. Material testing cannot account for different performance effects such as diffusion losses, contact resistance, thermal strain, and thermal cycling that occur in power generation modules. Module level testing is also vital for quantifying device performance, validating existing models, and optimizing module design, as well as testing for longevity and reliability of a device.

There have been two main approaches used for characterizing modules in the literature: the Harman approach and the steady-state approach. Both approaches have been utilized for low- and high-temperature testing in literature. This chapter describes some of the setups and analysis used for testing modules as well as bulk materials.

2.1 Harman Approach

The Harman approach [25] was initially developed for bulk material testing, but has been adopted and used for module testing. The technique is based on the Peltier effect of a thermoelectric material, specifically the heating and cooling at the module interfaces when a current is applied. When a current is passed through a module, the voltage across the module rises instantaneously to the electrical resistance component of the module, and then

asymptotically increases to the steady-state voltage, which is the sum of the resistive and Seebeck voltage. The Seebeck voltage is caused by the temperature difference developed in the device due to the Peltier cooling. The voltage is given by Eq. (1.1). When the current is removed from the module, the voltage drops instantaneously to the Seebeck component of the voltage and then decays to zero as heat conducts across the module and returns to being isothermal. The various properties are calculated using these voltages and resulting temperatures, and is described in detail in Section (3.2).

The method initially developed by Harman [25] uses the difference between the total voltage and the electrical resistance component of the voltage to calculate the Seebeck coefficient for the module. The method does not take into account effects like Thomson heating and joule heating, and heat losses due to conduction are assumed to be negligible. The method was validated by comparing values of properties with a reference material. A variation of this method was developed by Buist [26]. It uses the Seebeck component of voltage measured; specifically, the voltage immediately after the applied current is removed, to calculate the Seebeck coefficient. The approach called for bipolar testing to reduce errors and maximize accuracy of the results. This is explained in detail in Section (4.2). The method also includes a correction factor for the various heat losses.

Mitrani et al. [27] successfully used Buist's method to calculate module performance parameters. Instead of performing an energy balance, they used a reference material (aluminum) to calculate the thermal conductance of the module. The results were found to match the ones from steady-state testing as well as from electrothermal modeling in SPICE. A drawback of this general set of approaches is that it is difficult to measure thermoelectric properties above room temperature. This is because heat losses to the environment increase as the temperature increases above that of

the ambient, which makes it difficult to maintain adiabatic conditions on the module. Figure 2.1 shows the schematic of the test setup used.
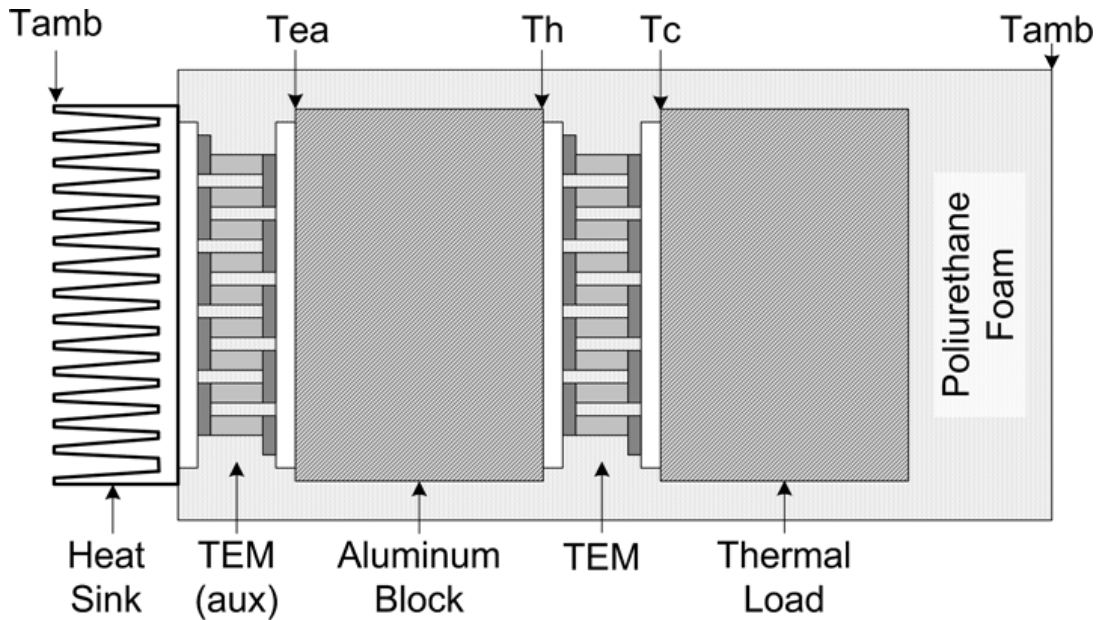
Figure 2.1: Schematic of the test setup used by Mitrani et al. [27]

Fujimoto et al. [28] attempted to overcome the issues with high-temperature testing by reducing thermal heat flow from the environment with a thermal anchor and a thermal reflector. They also accounted for heat losses from wire conduction and ambient radiation. An important discovery made while testing was that the largest cause of contact resistance was improper soldering at contacts. They applied corrections to better account for the effect of contact resistance, and reduced it by using a particular soldering technique.

The Harman approach can overlook convection losses by using a low vacuum. In cases where a vacuum is not used, a correction factor was developed by Lau [29] to account for convection effects. The correction factor was obtained by testing a module in both air and a vacuum and comparing the results. However, even with the correction factor, it was observed that some effects cannot be completely accounted for. Although this approach is extensively used with

materials with good, repeatable results, most of the testing is performed at room temperature. Consequently, one of the downsides is that modules are not tested under typical operating conditions.

2.2 Steady-State Approach

The second approach, the steady-state approach, ensures modules are tested under more realistic operating conditions. The testing approach is for a steady setup is relatively straightforward and the most common approach for module testing. One of the surfaces of the module is maintained at a high temperature while the other is maintained at a lower temperature. According to the laws of thermoelectricity, specifically the Seebeck effect, a potential difference is developed across the module. By measuring the heat flows into or out of the module along with the voltage and current, the module parameters can be estimated. An important assumption for the steady-state approach is that all heat losses are measurable and accounted for. Measuring the exact amount of heat rate flowing into or from the module is of utmost importance. However, obtaining an accurate measurement is often challenging. As this is such an important part of the approach, the various test stands in literature have been classified based on how they account for heat losses. They are classified as basic setups, where the heat losses are considered negligible because the setup is insulated well; passive accounting, where the heat losses are accurately measured and accounted for; and active accounting, where the heat losses are measured as well as minimized by using special guards.

Basic setups

Vazquez et al. [30] describe one such test stand for temperatures up to 300°C. The temperature limit was a result of the heater material selected, Duralumin. Two types of tests were performed;

one varied the hot side temperature and the second varied the hot side heat flux. The cold side was kept at a constant temperature. The various properties were calculated by loading the module with various resistors and plotting the relationship of the voltage versus the current. One drawback of the setup is that it does not account for any heat losses. The schematic of the setup is shown in Fig. 2.2.
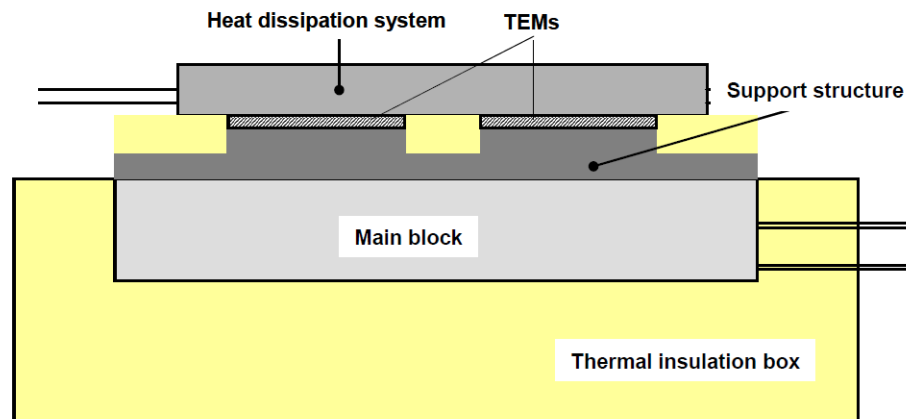
Figure 2.2: Schematic of the test setup developed by Vazquez et al. [30]

Tanji et al. [31] developed a steady-state test setup for testing of modules developed by a new type of assembly method. The setup observes the importance of applied pressure on the module and the effect of contact resistance. To reduce the contact resistance, they used a metallic paste of liquid InGa and solid Zn.

Another setup was developed by Hsu et al. [32] for modules up to 250°C. Although they did not account for heat losses, they provided a good explanation for the difference between material and module properties. They also observed the effect of loading pressure on the measured module parameters. Furthermore, an important method of relating the measured and theoretical properties was developed. The properties discussed in the previous literature were material properties, and the authors found large discrepancies when they were compared with their

experimental results. The main reason for the discrepancy was the effect of the temperature gradient across the components of the module. This gradient was accounted for by using thermal resistances across each component to determine the actual temperature gradient across the thermoelectric module.

Passive accounting

Anatychuk and Havrylyuk [33] developed a test stand for measuring parameters up to 600°C that accounts for heat losses from the hot side to the surrounding environment. The test stand uses a heat meter attached to the cold side heat exchanger, which measures the heat flux flowing out of the module. The heat meter used was a reference material of known conductivity such that the exact heat rate could be calculated using the temperature difference measurement. At steady-state conditions, it was assumed that the amount of heat flowing in will be equal to the amount of heat flowing out of the module. In order to accommodate different-sized modules, the setup employed interchangeable heat meters with an area resembling the module being tested. To minimize errors, the hot side was well calibrated using a protective heater. The authors also calculated the uncertainty in measurement, which was found to be 3%.

Another test stand was created by Sandoz-Rosado and Stevens [34] to characterize modules up to 500°C. The heat losses through the insulation on the top and sides of the heater as well as through the insulation surrounding the sides of the module were measured. A power analyzer measured the power input to the heaters. The authors also accounted for the effect of contact resistance by loading the module with different pressures to measure its performance. Figure 2.3 shows a schematic of the setup.
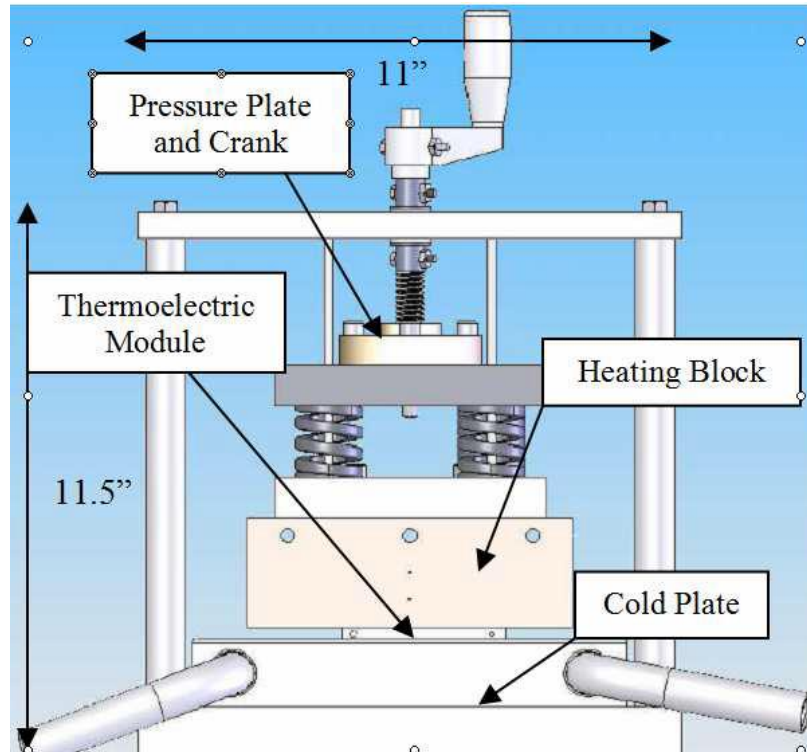
Figure 2.3: Experimental setup developed by Sandoz-Rosado and Stevens [34]

Muto et al. [35] developed a setup used to measure properties of bulk materials for temperatures up to 200°C with low uncertainty. These measurements also included the effects of side wall radiation and contact resistance. The researchers encountered large heat losses from the hot side assembly. To overcome this issue, they used a well-calibrated flux sensor on the cold side to measure the heat flux, which accounted for heat losses by calibrating the flux sensors. The authors used both approaches of the passive accounting—calculating heat losses and using a heat meter—to verify their calculations.

Although these techniques are used extensively at lower temperatures, calculating heat losses at higher temperatures leads to large uncertainties in measurements. The use of a reference material also has certain drawbacks, the most important being the accuracy of data available for the reference materials, which has an uncertainty of at least 5%. Other problems include difficulty in

measuring accurate temperature gradients within the reference material as well as calculating heat losses from the reference material.

Active accounting

To overcome the inherent errors in using passive accounting techniques, researchers have used radiation shields and shielding heaters to minimize heat losses. Rauscher et al. [36,37] use a shielding heater to minimize heat losses. The principle behind this approach is that any heat loss is related to a temperature difference in the system. If this difference is minimized, the losses can be minimized. A shielding heater is basically an outer heater that surrounds the heater in contact with the thermoelectric module. This ensures that all the heat supplied to the main heater block passes through the module and not to the surroundings. A similar approach was used by Takazawa et al. [38] in their setup to test modules up to 550K. They utilized a radiation shield to reduce heat losses at the upper temperature limits.

2.3 Other Testing Approaches

Apart from the two main approaches described above, researchers have also experimented with other methodologies to measure thermoelectric module parameters. Min and Rowe [39–41] developed a testing method based on the steady state but eliminating the need to measure the heat fluxes. This novel method utilizes an open-circuit and short circuit measurement to calculate module parameters. Even though it is steady state, it does not require the measurement of the exact amount of heat flowing through the module. This makes it especially attractive at high temperatures, where this measurement is difficult by traditional means. To investigate its application at high temperature, a detailed analysis was performed which is described in Section (3.3).

Similar to the Harman method, a transient method was developed by Middleton and Scanlon [42]. They used the method to measure the thermoelectric properties of germanium from 78–925K. The Seebeck coefficient was calculated using the change in voltage brought about by the change in temperature. To calculate the electrical resistance, the voltage response on the passage of current was used. This approach is known as the differential approach and was developed specifically for bulk materials. Sharath Chandra et al. [43] and Paul [44] developed high accuracy setups based on this approach. The setup developed by Ponnambalam et al. [22] is shown in Fig. 2.4.
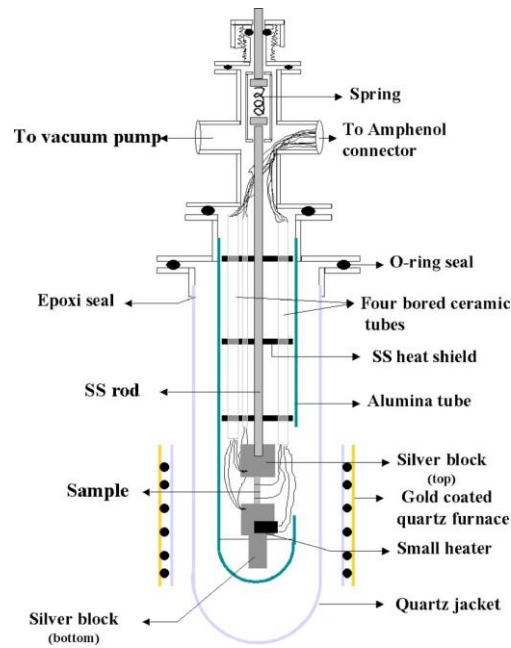
Figure 2.4: Sectional view of the setup used by Ponnambalam et al. [22]

Table 2.1 shows a brief summary of the different testing methods reported in the literature along with temperature ranges and device materials tested.

Author	Approach	Temp. Range	Material	Vacuum
Harman, T. C. [25]	Harman	300K	Bismuth telluride	Low vacuum
Buist and Richard [26]	Harman	<330K	N-type bismuth telluride	—
Mitrani et al. [27]	Harman	300K	Module	—
Fujimoto et al. [28]	Harman	<600K	N-type bismuth telluride	Low vacuum
Lau [29]	Harman	300K	Module	Low vacuum, air
Vazquez et al. [30]	Steady state	<573K	Module	—
Tanji et al. [31]	Steady state	<573K	Module	—
Hsu et al. [32]	Steady state	<523K	Module	—
Anatychuk and Havrylyuk [33]	Steady state	<873K	Module	—
Sandoz-Rosado and Stevens [34]	Steady state	<773K	Module	—
Muto et al. [35]	Steady state	<473K	P-type bismuth telluride	5×10^{-5} Torr
Rauscher et al. [36]	Steady state	<573K	Module	Low vacuum
Rauscher et al. [37]	Steady state	<573K	Module	7.5×10^{-5} Torr
Takazawa et al. [38]	Steady state	<550K	Module	7.5×10^{-5} Torr
Ahiska and Ahiska [45]	Steady state	<573K	Module	1×10^{-4} Torr

Author	Approach	Temp. Range	Material	Vacuum
Ciylan and Yilmaz [46]	Steady state	<373K	Module	—
Min and Rowe [39–41]	Steady-state based	<373K	Module	—
Iwasaki et al. [47]	Harman based	<315K	Module	1×10^{-7} Torr
Middleton and Scanlon [42]	Differential	78–925K	Germanium	High vacuum
Paul [44]	Differential	100–600K	P-type PbTe	5×10^{-5} Torr
Sharath Chandra et al. [43]	Differential	300K	Al doped FeSi platinum	1×10^{-4} Torr

From the literature review, it is clear that gaps exist in the area of high-temperature testing of modules. The main reason for this is modules that can be tested at high temperatures have yet to be developed. The high temperature setups developed are also found to yield fairly inconsistent results because of a lack of standardized guidelines for the measurement procedure [22,48]. This makes the selection of testing approach very difficult.

In summary, the popular choice for module testing seems to be the steady-state approach, but high temperature testing will encumber active accounting of heat losses. The Harman approach, though not extensively used for module testing at high temperatures, was the most used for testing of material properties. The Gao Min approach is also a possible choice as it does not require any measurements of the heat rates.

Chapter 3.   Preliminary Testing

Preliminary testing is important gauging response time of the setup, determine ability to maintain operating conditions and determine accuracy of instrumentation required. Of the various approaches discussed in the literature for measuring module parameters, three were narrowed down as candidates for the proposed high-temperature testing system. To determine the best overall testing system, three preliminary setups based on the principles of the steady-state [34] approach, Harman [26] approach, and the Gao Min [39] approach were developed to better understand the various issues associated with each method before designing the high-temperature test setup, the primary goal of this research.

The results from the three setups were compared for modules at low temperatures. Information about module parameters is readily available for low temperatures, making comparison easy. A commercially available BiTe module (Thermonamic Electronics TEP1-1264-1.5) with 126 leg pairs was used. The size of the module was 40mm x 40mm, with 50% fill area, meaning 50% of the module was air. Tests were conducted at a constant loading pressure and with thermal grease on both sides of the module. Considering the rudimentary design, an uncertainty of 10% was assumed. All the tests were performed at an average temperature of 100°C to keep the results comparable. Multiple tests were performed on the same module to ensure repeatability in measurements. All measurements were made using the same DAQ devices: NI–USB 6008 for voltage and current readings and NI–TC 2095 for temperature readings.

3.1 Steady-State Method

The test setup developed by Sandoz-Rosado and Stevens [34] was successful as a tool for characterization of module performance. The major achievement in the setup was to quantify the heat transfer to the hot side of the module while adjusting the temperature difference across devices under a wide range of electrical loads. Using measurements of the current, voltage, and the hot side and cold side temperatures, the Seebeck level of the device, electrical resistance, and thermal conductance parameters can be determined. Tests were carried out at various loading pressures and temperatures, and a platform for characterizing module performance was developed. Working with this test setup provided an insight into the various problems that may arise, albeit only for low temperatures. A simplified schematic of the steady-state approach can be seen in Fig. 3.1.
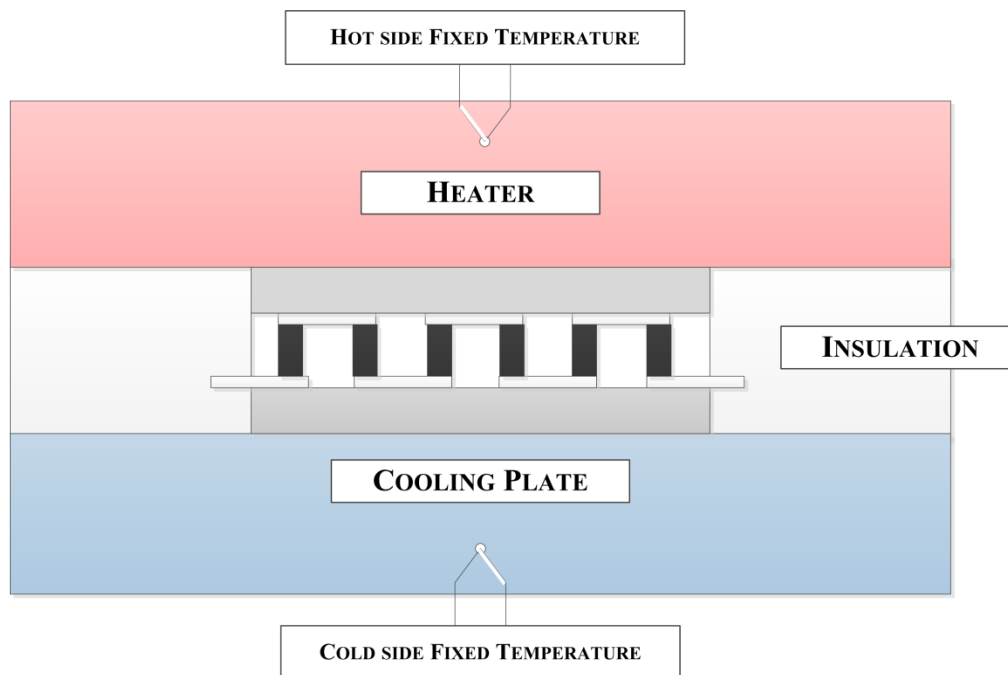
Figure 3.1: A simplified schematic of the steady-state approach

The size of the module to be tested was much smaller than the size of the heater. The model developed by Rosado-Sandoz and Stevens [34] was used in calculating the heat loss from the heater.

A typical test involves a device subjected to a fixed temperature difference and held until temperatures and the heat flux have stabilized, which typically takes nearly an hour to reach a steady state. Once a steady state is reached, a scan at different electrical loads is performed. Although one could extract the electrical resistance and fully characterize the device using only a short-circuit current and open-circuit voltage measurement, a scan over many operating points along the voltage-current curve will improve confidence in the device's parameter calculations.

For a scan, the module is connected to an automated electrical loading box and 12 different loads are automatically applied to try to sweep the entire current-voltage curve for the device. Between each of the 12 steps, the module is allowed to reach a steady state. The time for these varies because heat rates change as a function of the operating current, as can be seen in Equations (1.7) and (1.8). This scan of voltage-current data provides the basis for calculation of thermoelectric performance parameters of a device. The scan obtained from the test setup is exported into Excel for further analysis. The properties are calculated by two different means and then compared. The three required module parameters are the device-level Seebeck coefficient, electrical resistance, and thermal resistance.

The principal approach to extracting module parameters is to minimize the residuals between the measured values of voltages and hot side heat rates and their theoretical values by varying the three module parameters. A scan can be seen in Fig. 3.2.
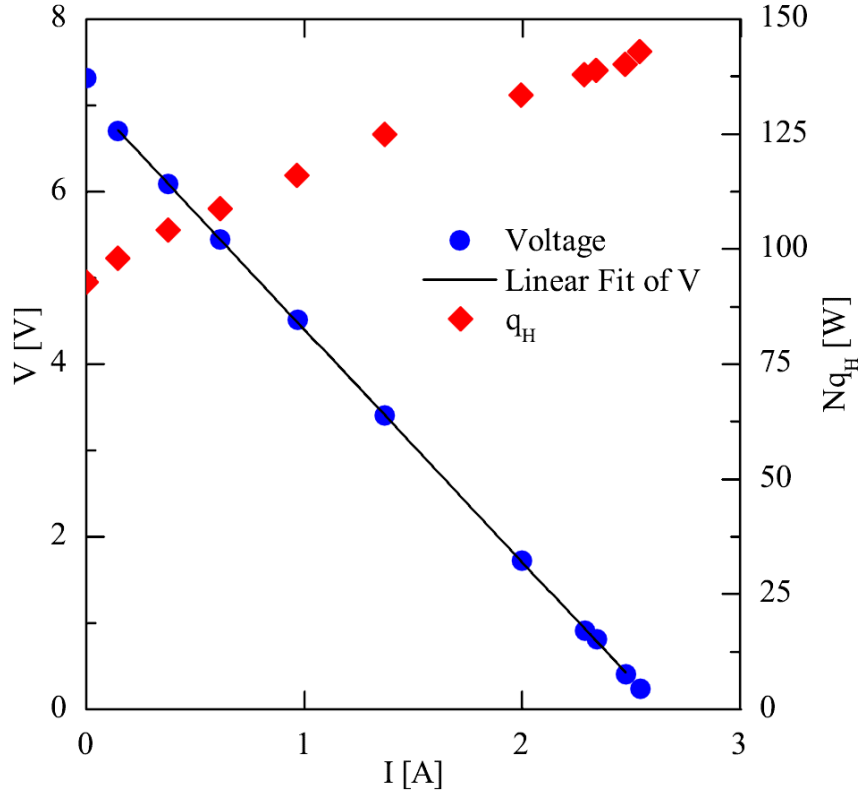
Figure 3.2: Module scan for steady-state approach [49]

The theoretical heat rate is given by Eqn. (1.7) and the theoretical voltage can be obtained by dividing the power Equation (1.10) by the current to give the voltage as:

$$V = \alpha\Delta T - IR^2 \qquad (3.1)$$

Residuals are measured as the square of the difference between the two values to account for positive and negative errors. The minimization provides one set of the values of the module's parameters, the slope, and the y-intercept of the current-voltage line.

The y intercept gives the open-circuit voltage (V_{OC}) and the slope of the plot is equivalent to the electrical resistance (R). The Seebeck coefficient (α) is calculated as:

$$\alpha = \frac{V_{OC}}{\Delta T} \qquad (3.2)$$

The thermal conductance of the module can be expressed as the ratio of the actual heat to the hot side of the module under open-circuit conditions to the temperature difference across the module:

$$K = \frac{Q_H}{T_H - T_C} \quad\quad (3.3)$$

The module effective figure of merit, *ZT,* is calculated as:

$$ZT = \frac{\alpha^2 T_{AV}}{RK} \qu\quad (3.4)$$

The values obtained from Eqns. (3.2) - (3.4), and the slope of the line (R), are compared with the values from the minimization scheme. The two sets of values are found to be in agreement with a difference of less than 5%.

The tests were carried out multiple times to test for repeatability. The results, averaged over multiple tests, were tabulated as seen in Table 3.1.

Table 3.1: Steady-State Results for T_H = 150°C and T_C = 50°C

Properties	Steady State (397K)
α (V/K)	0.044
R (Ω)	2.42
K (W/K)	0.63
ZT	0.47

As mentioned earlier, as this setup is the most developed one, it will be used for low-temperature benchmarking of the preliminary setups of the two other approaches.

3.2 Harman Method

To obtain accurate results, the steady-state approach requires careful estimation of all possible heat losses, which becomes challenging at high temperatures. The experimental time is also significant. An alternative to the steady-state setup is the Harman approach. The key to this method is a computer-driven, high speed, high resolution, integrating voltage measurement system capable of accurately resolving the voltage components in an active thermoelectric device or sample [26]. In order to determine the effectiveness of this approach, a prototype of such a setup was built and a model tested at low temperatures as a proof of concept.

This approach has many advantages over the steady state. It provides for the measurement of all the parameters needed to characterize the thermoelectric properties of a module. The current requirement for Harman approach is very low. For low-temperature applications, it was observed that the transient setup requires a current 1/50th of that required for the steady-state setup [50,51]. Another advantage is that it can be used to potentially determine the cause of the failure of a device.

To accurately test properties of a module, the arrangement used was the "heat sunk" configuration. This involves maintaining adiabatic conditions on the cold side to control the temperature, as seen in Fig. 3.3. Advantages of this configuration include potentially quicker testing and simplicity of the connections. There were four quantities that need to be measured to characterize a thermoelectric device: the Seebeck voltage (V_O), the steady-state current (I) under a specific electrical load, and the hot and cold side temperatures (T_H) and (T_C) respectively.
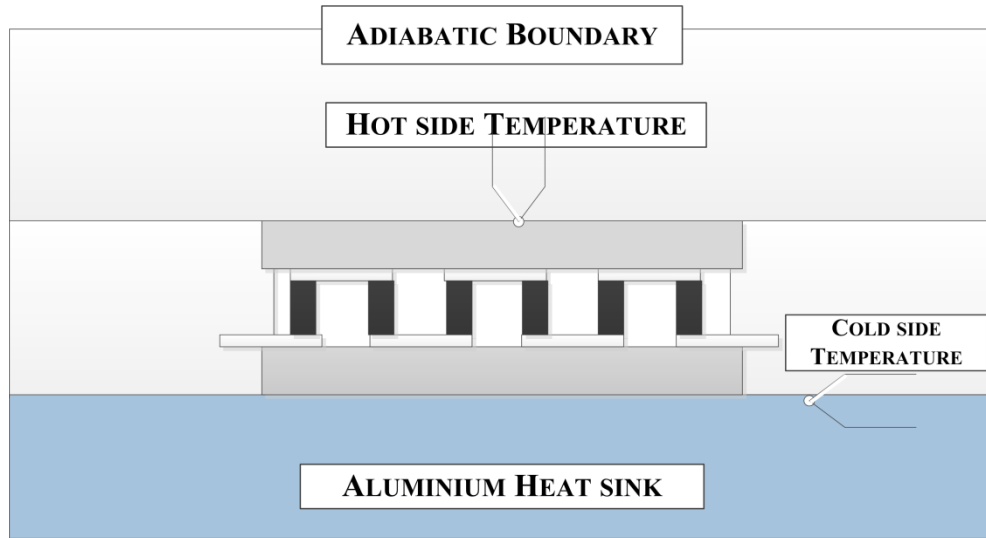
When a current is applied to a thermoelectric device, a voltage develops across it. This voltage is a combination of the resistive voltage (V_r) and the Seebeck voltage (V_O). The applied current also generates a small temperature difference across the module (ΔT).

The total potential difference across the module can be written as:

$$V_i = V_o + V_r \tag{3.5}$$

where

$$V_o = \alpha \times \Delta T \tag{3.6}$$

$$V_r = I \times R \tag{3.7}$$

The Seebeck coefficient and electrical resistance are calculated as

$$\alpha = \frac{V_o}{\Delta T} \tag{3.8}$$

$$R = \frac{V_r}{I} \tag{3.9}$$

where I is the applied current. The thermal conductance (K) is calculated using the energy balance, which is discussed later.

The test to determine the module properties is based on the measurement of V_O. When a current is applied to an isothermal module, the voltage rises instantaneously to value V_r and then asymptotically increases to V_i, as a temperature difference develops across the device because of the Peltier cooling and heating at the two interfaces. When the current is turned off, the voltage instantaneously drops to V_O and then decays to zero as the module become isothermal over time due to conduction [50]. The measurement of the value V_O is the basis of the *modified* Harman approach. Figure 3.4 shows the nature of the current applied and its corresponding output voltage. The figure uses S as an abbreviation for the Seebeck coefficient, whereas the symbol used henceforth is α.
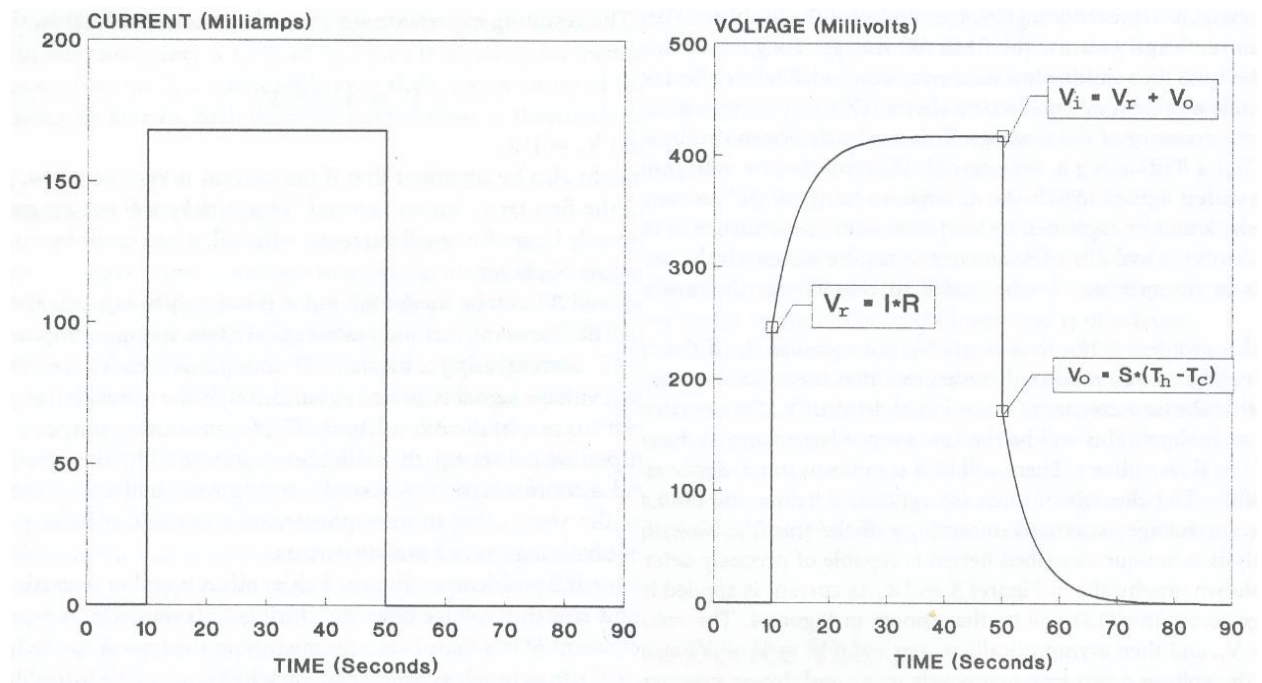
Figure 3.4: Current pulse applied to a TEM and the transient voltage generated due to it [50]

The tests conducted are bipolar processes. The test is carried out using one polarity of the current; the current is then reversed and the test repeated [50]. Bipolar testing is essential as it can remove many errors in testing, with the primary purposes being to minimize the uncertainties

associated with Joule heating, and wire losses, and to reduce the magnitude of a correction factor. In the modified Harman method, it is assumed that the thermocouples used are perfectly identical. If this is not the case, additional errors may be encountered. Bipolar testing process corrects for any imperfections caused by non-identical thermocouples.

Derivation for the heat sunk case

The calculation of the Seebeck coefficient (α) and the electrical resistance (R) is straightforward. To calculate thermal conductance (K), the model developed by Buist [50] was used by modifying it to suit the heat sunk case. The figure of merit can be calculated with the help of the standard equation. Figure 3.5 shows a schematic of the test setup. A module is attached to a heated aluminum block, which acts as a heat sink with the help of thermal grease. The other side of the module is well insulated to maintain adiabatic conditions. The temperature of the aluminum block is maintained at the required average temperature, in this case 100°C.
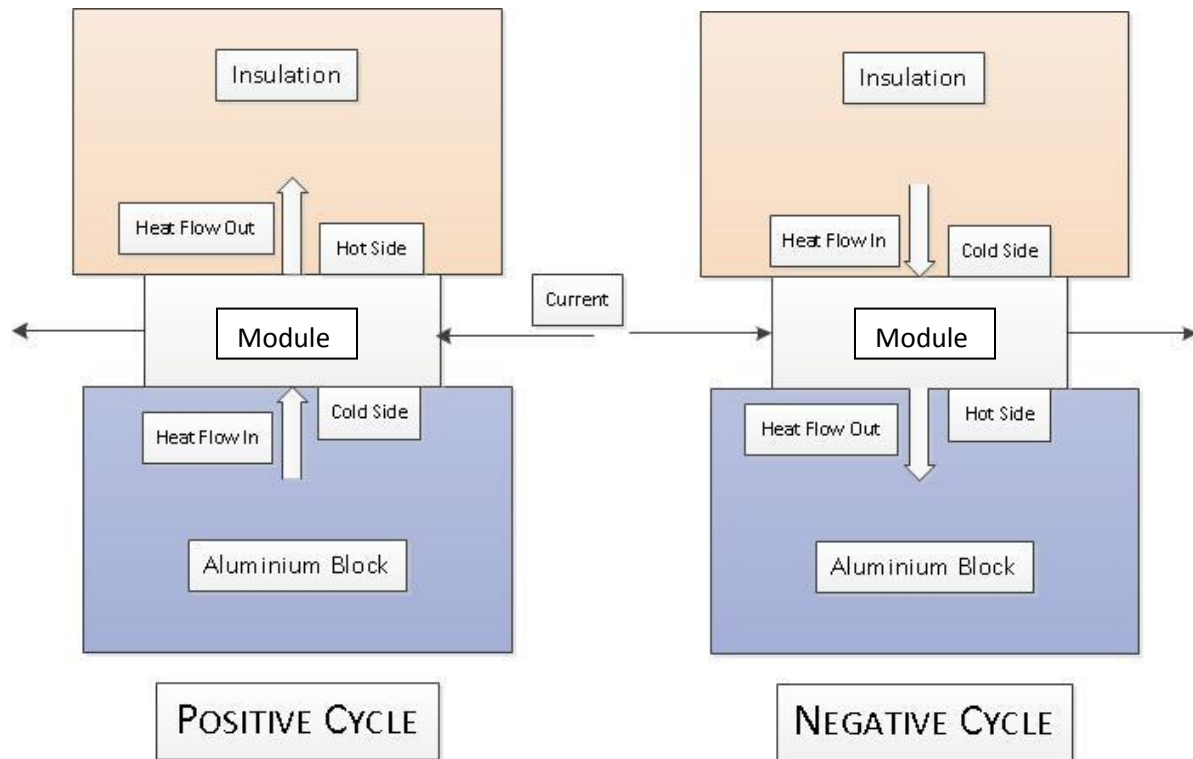
Figure 3.5: Schematic of the experimental setup for the positive and negative tests showing the flow of heat from and into the module

A current is passed through the module, which produces a voltage and corresponding temperature difference. The flow of heat into and out of the module depends on the direction of the current. In our test, when the temperature of the aluminum block was lower than the adiabatic surface, it was called a positive cycle, and when the temperature of the block was higher, it was called a negative cycle. All terms with a prime ($'$) notation refer to the negative cycle.

The ($\overline{\quad}$) for any term indicates that it is averaged over the bipolar tests. Note that the sign convention defined in Fig. 3.5 is that positive values for heat flow on the cold side represent heat flowing into the cold surface, while positive values on the hot side represent heat leaving the hot surface.

All measurements are taken at a steady state when there is no significant change in voltage and temperature differences.

In all equations, $\Delta T = T_h - T_c$ and $\Delta T' = T'_h - T'_c$. T_{am} is the ambient temperature.

The components of the heat flow, which can be seen in Fig. 3.6, can be expressed as:
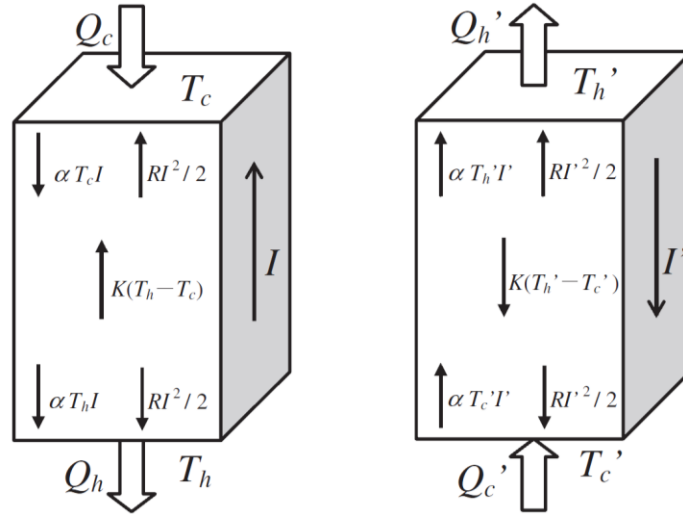
Figure 3.6: Thermal modeling when current is applied in thermal equilibrium [28]

$\boldsymbol{Q_P} = \boldsymbol{Module\ Peltier}$ **(sum of module Peltier heating and cooling for both current**

directions)

Positive Test: Cold Side $= -\alpha I T_c$

Hot Side $= -\alpha I T_h$

Negative Test: Cold Side $= -\alpha I T'_c$

Hot Side $= -\alpha I T'_h$

$$Q_P = -\alpha[I(T_h + T_c) + I'(T'_h + T'_c)] \tag{3.10}$$

$Q_\lambda = Module\ conduction$(sum of all module internal conduction heat transfers)

Positive Test: Cold Side $= \frac{\lambda_{mod}A_{mod}}{L}\Delta T$

Hot Side $= \frac{\lambda_{mod}A_{mod}}{L}\Delta T$

Negative Test: Cold Side $= \frac{\lambda_{mod}A_{mod}}{L}\Delta T'$

Hot Side $= \frac{\lambda_{mod}A_{mod}}{L}\Delta T'$

$Q_\lambda = \frac{2\lambda_{mod}A_{mod}}{L}(\Delta T + \Delta T')$

If K is the effective conductance of the module, A_{mod} the surface area of the module, and L the thickness of the module,

then $\frac{\lambda_{mod}A_{mod}}{L} = K_{mod}$

$$Q_\lambda = 2K_{mod}(\Delta T + \Delta T') \tag{3.11}$$

$Q_i = Conduction\ through\ insulation$

Positive Test: Cold Side $= 0$

Hot Side $= \frac{\lambda_i A_{mod}}{L_i}(T_h - T_i)$

Negative Test: Cold Side $= \frac{\lambda_i A_{mod}}{L_i}(T'_i - T'_c)$

Hot Side $= 0$

Where λ_i is the conductivity of the insulation material and L_i is the thickness of the insulation,

$$Q_i = \frac{\lambda_i A_{mod}}{L_i}(T_h - T'_c + T'_i - T_i) \tag{3.12}$$

Q_{Al} = Heat conducted from module to aluminium block

Positive Test: Cold Side $= \frac{\lambda_{Al}A_{Al}}{L_{Al}}(T_{am} - T_c)$

$\quad\quad\quad\quad\quad$ Hot Side $= 0$

Negative Test: Cold Side $= 0$

$\quad\quad\quad\quad\quad$ Hot Side $= \frac{K_{Al}A_{Al}}{L_{Al}}(T'_h - T_{am})$

Where λ_{Al} is the conductivity of the aluminum block, A_{Al} is the surface area of the aluminum

block, and L_{Al} is the thickness of the aluminum block,

$$Q_{Al} = \frac{\lambda_{Al}A_{Al}}{L_{Al}}(T'_h - T_c)$$

Let $\frac{\lambda_{Al}A_{Al}}{L_{Al}}$ be denoted as the effective conductance, K_{block}:

$$Q_{Al} = K_{block}(T'_h - T_c) \quad\quad\quad\quad (3.13)$$

Q_j = Joule heating

Positive Test: Cold Side $= I^2 \, R/2$

$\quad\quad\quad\quad\quad$ Hot Side $= -I^2 \, R/2$

Negative Test: Cold Side $= I'^2 \, R/2$

$\quad\quad\quad\quad\quad$ Hot Side $= -I'^2 \, R/2$

$$Q_j = 0 \quad\quad\quad\quad (3.14)$$

Two other sources corresponding to wire conduction and wire joule heating are neglected owing

to very low resistance when compared to the module.

Now, at a steady state, the sum of all expressions is

$$Q_P + Q_\lambda + Q_{Al} + Q_j = 0 \qu\quad\quad\quad (3.15)$$

By manipulating the expression, one can obtain

$$-Q_P = Q_\lambda + Q_{eq} + Q_{Al} \tag{3.16}$$

$$-Q_P = Q_\lambda(\frac{Q_{eq}}{Q_\lambda} + \frac{Q_{Al}}{Q_\lambda})$$

Let $A = \frac{Q_{eq}}{Q_\lambda}, B = \frac{Q_{Al}}{Q_\lambda}$.

In solving for B,

$$B = \frac{Q_{Al}}{Q_\lambda} = \frac{K_{block}(T'_h - T_c)}{2K(\Delta T + \Delta T')} \tag{3.17}$$

because $(T'_h - T_c) \approx 0$ when the module is in a steady state for both bipolar tests. This

assumption is valid as it represents the temperature of the aluminum block. In both cases, this

temperature is manually controlled.

Thus, we can assume that B $\approx$ 0 for proof of concept testing, but more extensive analysis will

need to be made for full and critical testing.

Let $C = 1 + A$

where A is the correction factor for the equivalent heat losses and C is the overall correction

factor.

$$-Q_P = Q_\lambda C \tag{3.18}$$

Now, solving for α,

$$\alpha = \frac{Q_\lambda H}{I(T_h + T_c) + I'(T'_h + T'_c)} = K \frac{(\Delta T + \Delta T')C}{I(T_h + T_c) + I'(T'_h + T'_c)} \tag{3.19}$$

But, from the voltage equations of a TEM, we know

$$V_o = \alpha(T_h + T_c) \text{ and } V'_o = \alpha(T'_h + T'_c)$$

Hence,

$$\alpha = \frac{V_{oa}}{(\Delta T + \Delta T')} \tag{3.20}$$

where $\bar{V}_o = \frac{V_o + V_o'}{2}$

By equating Eqns. (3.19) and (3.20), we can calculate the value for conductance:

$$K = \frac{\bar{V}_o[I(T_h+T_c)+I'(T\prime_h+T\prime_c)]}{C(\Delta T + \Delta T')^2} \tag{3.21}$$

The resistance is calculated using the resistive component of voltage and is very straightforward:

$$R = \frac{\bar{V}_r}{\bar{I}} = \frac{\bar{V}_l - \bar{V}_o}{\bar{I}} \tag{3.22}$$

To calculate the dimensionless quantity figure of merit, we use the standard formula

$$ZT = \frac{\alpha^2 T_{av}}{RK} \tag{3.23}$$

By substituting Eqns. (3.20), (3.21), and (3.22) in (3.23),

$$ZT = \frac{\left[\frac{\bar{V}_O}{(\Delta T + \Delta T')}\right]^2 T_{av}}{\left(\frac{\bar{V}_l - \bar{V}_o}{\bar{I}}\right)\left(\frac{\bar{V}_O[I(T_h+T_c)+I'(T\prime_h+T\prime_c)]}{C(\Delta T + \Delta T')^2}\right)} \tag{3.24}$$

In solving, we get

$$ZT = \frac{\bar{V}_o T_{av} \bar{I}}{(\bar{V}_l - \bar{V}_o)[I(T_h+T_c)+I'(T\prime_h+T\prime_c)]} \tag{3.25}$$

Equations (3.20) - (3.22), and (3.25) fully characterize a thermoelectric device based on voltage, current, and temperature measurements. This approach is known as the *modified* Harman method. Note that no heat rate measurement is required, which is typically the case for steady-state testing methods. Thus, using this approach eliminates the uncertainty of measuring heat rates.

Preliminary experimental setup

The experimental setup consists of a power supply, a shunt resistor, an aluminum heat sink, and a couple of thermocouples to measure the temperatures. The data from the thermocouples as well as the current and voltage sensors is recorded with the help of a DAQ board. The block diagram of the setup is depicted in Fig. 3.7.
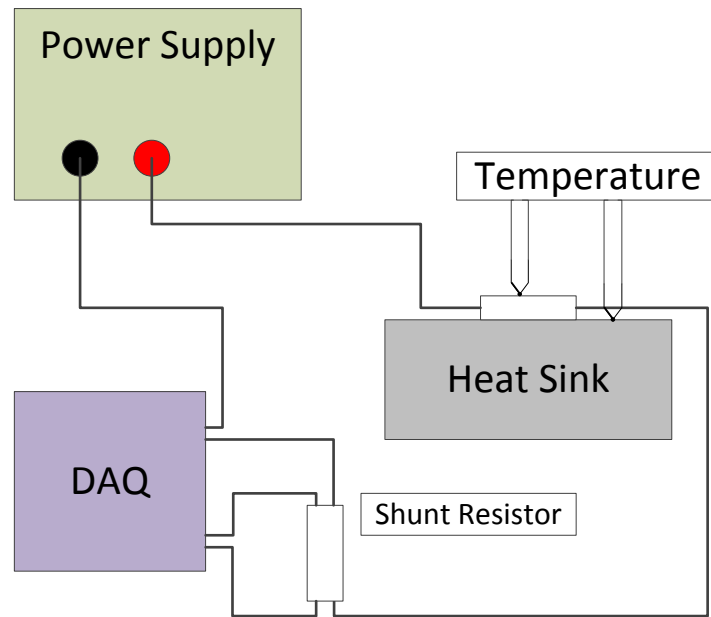
Figure 3.7: Block Diagram of the experimental setup for Harman method

One of the major advantages of the modified Harman method is the need for only a low current, which is typically 10% [50] of the short-circuit current of the module. For the comparison test, the current is set at 0.5A, and varied to check its effect on the properties. A 0.05Ω shunt resistor is connected in the circuit to assist in the measurement of the current and voltage. Two thermocouples are used to measure the hot side and cold side temperatures of the module.

Experimental data

To ensure repeatability of the test, a standard procedure was developed. The experimental

procedure was as follows:

- No current was passed for the first 75 seconds on an isothermal module.

- The selected value of the current was passed for 300 seconds.

- No current was passed for the next 300 seconds.

The timed steps above were selected by keeping in mind that the module must reach a steady

state when the measurements are taken. Figure 3.8 shows the display for the voltage and current

versus time for a sample test sequence. The USB DAQ device had a lot of noise in the current

readings, which was dampened before calculating properties.
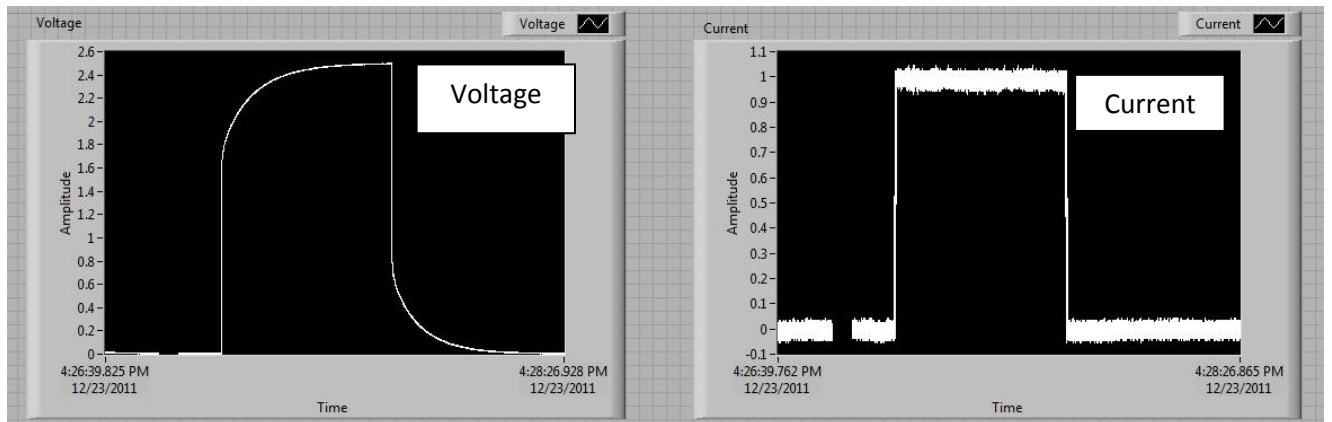
<div align="center">Figure 3.8: The plots for voltage and current</div>

The data obtained from the DAQ was used to obtain the key module parameters using

Equations (3.20) - (3.22), and (3.25) above and compared with the data from the steady-state

experiments. Table 3.2 shows a comparison of the measured parameters using the two

techniques.

Property Measured	Modified Harman Method (373K)	Steady State (373K)
α (V/K)	0.054	0.044
R (Ω)	2.21	2.42
K (W/K)	0.892	0.63
ZT	0.54	0.47

Temperature correction

For effective comparison of properties with the steady-state method, a temperature correction must be applied to the modified Harman results. Because the Harman approach was developed for material testing and adapted for modules, it does not include the temperature gradient between the thermoelectric pellet and the ceramic face, where the thermocouples are attached to take measurements. This can be seen in fig. 3.9. This will cause the temperature difference to be overestimated. To compensate for this, a correction factor needs to be applied to the temperature readings from the Harman approach.
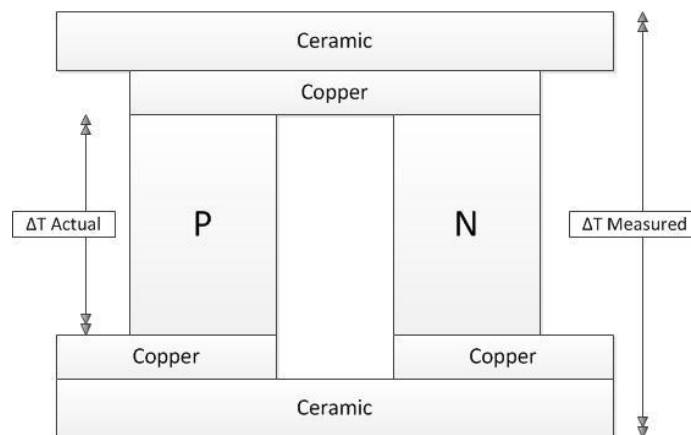
Figure 3.9: The difference of the temperature readings

Evaluation of the multiplying factor

The factor can be calculated by considering the module as a set of thermal resistances, as shown in Fig. 3.10.
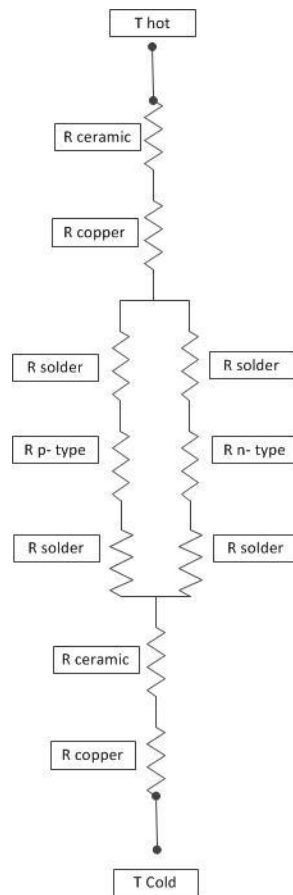
Figure 3.10: Thermal resistances in a TEM

Using the standard values of materials available in the literature, we can compute each thermal resistance, as shown in Table 3.3.

Material	Length (m)	Conductivity (W/m-K)	Cross-sectional Area (m²)	Thermal Resistance (K/W)
Copper	0.00052	385	2.32E-06	0.583
Ceramic	0.00111	22	2.32E-06	21.792
P-type thermoelectric material	0.00129	1.545	1.10E-06	757.325
N-type thermoelectric material	0.00129	1.54	1.10E-06	759.784
Solder	0.00005	50	1.10E-06	0.907

We can now calculate the multiplying factor as

$$MF = \frac{(R_{eq})_{TE-material}}{(R_{eq})_{entire\ module}}.$$ (3.26)

Thus, MF = 0.8946.

Using this multiplying factor, the results from the forward and reverse tests were compared again with the steady-state results, as seen in Table 3.4.

Properties	Modified Harman (397K)	Steady State (397K)
α (V/K)	0.048	0.044
R (Ω)	2.25	2.42
K (W/K)	0.7	0.63
ZT	0.541	0.47

Testing with different temperatures showed that the module properties are highly temperature dependent. The trend for the Seebeck coefficient was observed to be the reverse of the trend in the steady-state results. Upon comparison, the properties varied by about 15% from the steady-state results.

This difference was observed on repeated testing on different modules. Due to the fundamental differences in the two methods of testing, a third approach, an offshoot of the steady-state method, was investigated.

3.3 Gao Min Method

The Gao Min method is simple to implement and also allows for simultaneous measurements of the thermoelectric properties [39–41]. It uses a novel open-circuit/closed-circuit measurement technique. The experimental time is longer than that of the modified Harman approach, as the properties are measured at a steady state. The primary difference between the Gao Min approach and the steady-state approach is in that the hot side is controlled. In the Gao Min method, a constant heat rate is applied on the hot side, while for the steady-state case the heat rate varies and the hot side temperature is held constant.

Figure 3.11 shows the configuration schematic. The setup has a thermoelectric module sandwiched between a heater running at a constant heat flux and a cold plate of a fixed temperature. All other sides are well insulated to prevent heat loss.
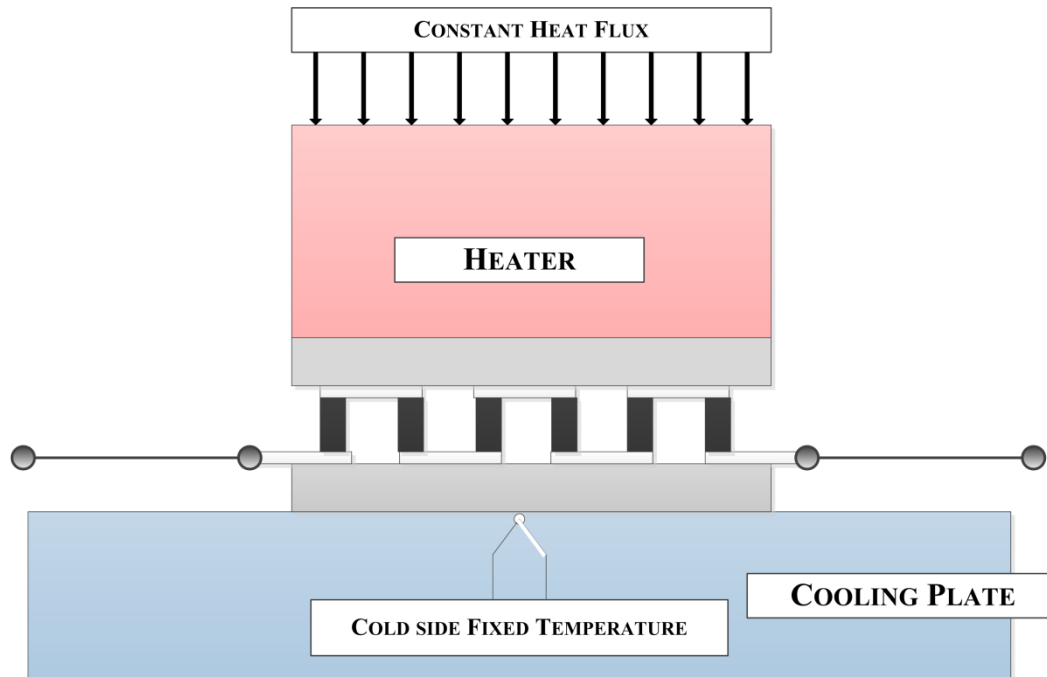
The test is first carried out in an open-circuit condition with no load. When a temperature difference is applied across a module, a voltage is generated across it. At a steady state and when the module is in open-circuit conditions, V_{OC} is the voltage generated due to an applied temperature difference of ΔT_{OC}. The module is then short-circuited. A current due to the Seebeck voltage flows through the specimen, resulting in additional heat flow due to the Peltier effect [39]. As the heat flux being applied remains the same, a new temperature difference, $\Delta T_{SC,}$ is generated across the module.

There are four quantities that need to be measured, with the first three being the open-circuit voltage (V_{OC}), the open-circuit temperature difference (ΔT_{OC}), and the short-circuit temperature

difference (ΔT_{SC}). All these values are measured at a steady-state condition. To obtain the fourth measurement, that of resistance (R), which is the voltage reading that occurs instantly upon loading, (V_L) is required.

This test is used to calculate the Seebeck coefficient and the figure of merit. To calculate the electrical resistance, a second test is carried out using resistors of known values. As soon as the module is loaded with a known load resistance (R_L), the instantaneous voltage response (V_L) of the module is recorded. The load is immediately removed to ensure that there is no thermal response from the module. The Seebeck coefficient (α), electrical resistance (R), and figure of merit (ZT) can be calculated using:

$$\alpha = \frac{V_{OC}}{\Delta T_{OC}} \tag{3.27}$$

$$R = R_L\left(\frac{V_{OC}}{V_L} - 1\right) \tag{3.28}$$

$$ZT = \frac{\Delta T_{OC}}{\Delta T_{SC}} - 1 \tag{3.29}$$

The derivation for calculating the properties is described as follows.

Derivation

To determine the thermoelectric module properties, the measurements of V_{OC}, V_L, ΔT_{OC}, and ΔT_{SC} are used. The Seebeck coefficient, thermal conductance, and electrical resistance were calculated as per the model developed by Min [39]. Under a steady-state condition with the module at open circuit, the voltage generated is solely due to the Seebeck effect, so

$$V_{OC} = \alpha\Delta T_{OC}. \tag{3.30}$$

The heat rate entering the hot side (Q_H) is given by

$$(Q_H)_{OC} = I_{OC}\alpha T_H - \frac{1}{2}I_{OC}^2 R + K\Delta T_{OC} \tag{3.31}$$

But for an open circuit, $I_{OC} = 0$

$$(Q_H)_{OC} = K\Delta T_{OC} \tag{3.32}$$

$$(Q_C)_{OC} = K\Delta T_{OC} \tag{3.33}$$

By subtracting (3.33) from (3.32), we get

$$(Q)_{OC} = 0 \tag{3.34}$$

When the circuit closed, the current due to the Seebeck voltage will flow through the module, causing more heat flow across the module:

$$(Q_H)_{SC} = I_{SC}\alpha(T_H)_{SC} - \frac{1}{2}I_{SC}^2 R + K\Delta T_{SC} \tag{3.35}$$

$$(Q_C)_{SC} = I_{SC}\alpha(T_C)_{SC} + \frac{1}{2}I_{SC}^2 R + K\Delta T_{SC} \tag{3.36}$$

By subtracting (3.36) from (3.35), we get

$$(Q)_{SC} = I_{SC}\alpha\Delta T_{SC} - I_{SC}^2 R \tag{3.37}$$

But at a steady state, $(Q)_{SC} = 0$, so

$$I_{SC}\alpha\Delta T_{SC} = I_{SC}^2 R \tag{3.38}$$

$$\alpha = \frac{I_{SC}R}{\Delta T_{SC}} \tag{3.39}$$

The heat input is constant for both cases, so

$$(Q_H)_{OC} = (Q_H)_{SC} \tag{3.40}$$

Hence,

$$K\Delta T_{OC} = I_{SC}\alpha(T_H)_{SC} - \frac{1}{2}{I_{SC}}^2 R + K\Delta T_{SC} \tag{3.41}$$

By substituting the value of α from (3.39) in (3.41),

$$K\Delta T_{OC} = \left(\frac{I_{SC}R}{\Delta T_{SC}}\right)I_{SC}(T_H)_{SC} - \frac{1}{2}{I_{SC}}^2 R + K\Delta T_{SC} \tag{3.42}$$

$$K\Delta T_{OC} - K\Delta T_{SC} = (I_{SC})^2 R\left[\frac{(T_H)_{SC}}{\Delta T_{SC}} - \frac{1}{2}\right] \tag{3.43}$$

$$K(\Delta T_{OC} - \Delta T_{SC}) = \frac{\alpha^2 {\Delta T_{SC}}^2}{R}\left[\frac{(T_H)_{SC}}{\Delta T_{SC}} - \frac{1}{2}\right] \tag{3.44}$$

$$\frac{(\Delta T_{OC} - \Delta T_{SC})}{{\Delta T_{SC}}^2\left[\frac{(T_H)_{SC}}{\Delta T_{SC}} - \frac{1}{2}\right]} = \frac{\alpha^2}{RK} \tag{3.45}$$

$$\frac{(\Delta T_{OC} - \Delta T_{SC})}{(\bar{T})_{SC}\Delta T_{SC}} = \frac{\alpha^2}{RK} \tag{3.46}$$

$$\frac{(\Delta T_{OC} - \Delta T_{SC})}{\Delta T_{SC}} = \frac{\alpha^2(\bar{T})_{SC}}{RK} = Z(\bar{T})_{SC} \tag{3.47}$$

Hence,

$$ZT = \frac{\Delta T_{OC}}{\Delta T_{SC}} - 1 \tag{3.48}$$

From (3.30) we have

$$\alpha = \frac{V_{OC}}{\Delta T_{OC}} \tag{3.49}$$

To calculate the resistance, a load resistor of known value is connected in series with the circuit, as shown in Fig.3.12.

Let R_L be the load resistor connected in series and V_L be the voltage measured across the thermoelectric module immediately after loading the circuit from the open-circuit state. This is done, assuming that $\Delta T_{OC} \approx \Delta T_L$, where ΔT_L is the temperature difference immediately after electrical loading across the module as it is loaded with the resistor.
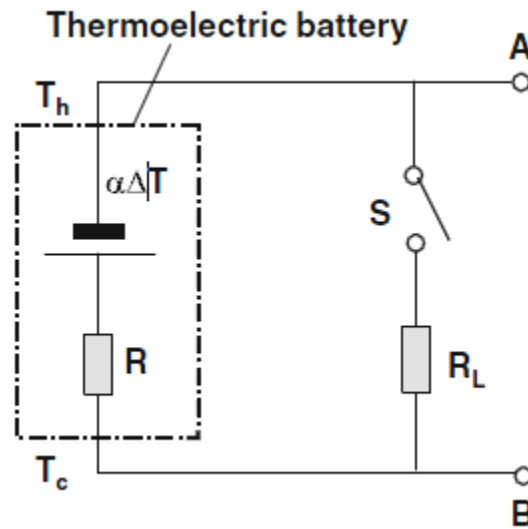
Figure 3.12: The equivalent circuit for calculating the resistance

As the current through the circuit is the same, we get

$$\frac{V_{OC}}{R+R_L} = \frac{V_L}{R} \tag{3.50}$$

$$RV_{OC} = V_L(R + R_L) \tag{3.51}$$

Hence we obtain

$$R = R_L \left(\frac{V_{OC}}{V_L} - 1\right) \tag{3.52}$$

The standard equation for ZT can be written as

$$ZT = \frac{\alpha^2 T}{RK} \tag{3.53}$$

By substituting (3.45), (3.46), and (3.49) in (3.50), and solving for the conductance, we get

$$K = \frac{(V_{OC})^2 \Delta T_{SC} V_L (\bar{T})_{SC}}{R_L (\Delta T_{OC})^2 (\Delta T_{OC} - \Delta T_{SC})(V_{OC} - V_L)} \tag{3.54}$$

Thus, all the parameters of a TEM can be calculated using the Gao Min method using Eqns. (3.48), (3.49), (3.52), and (3.53) by measuring ΔT_{OC}, ΔT_{SC}, V_{OC}, V_L, R_L, and $(\bar{T})_{SC}$.

Experimental setup

The setup consists of an aluminum heater block placed over the module on the hot side and a cooling plate, which uses water as a cooling liquid, on the cold side. The aluminum block is heated with the help of a cartridge heater that is controlled at a constant heat flux. The length and breadth of the block are the same dimensions as the module, to minimize parasitic bypass losses. Three thermocouples are placed in holes machined 2.5mm from the heater surface. The thermocouples are used to verify that an isothermal heater surface is maintained. The schematic of the setup can be seen in fig. 3.13.
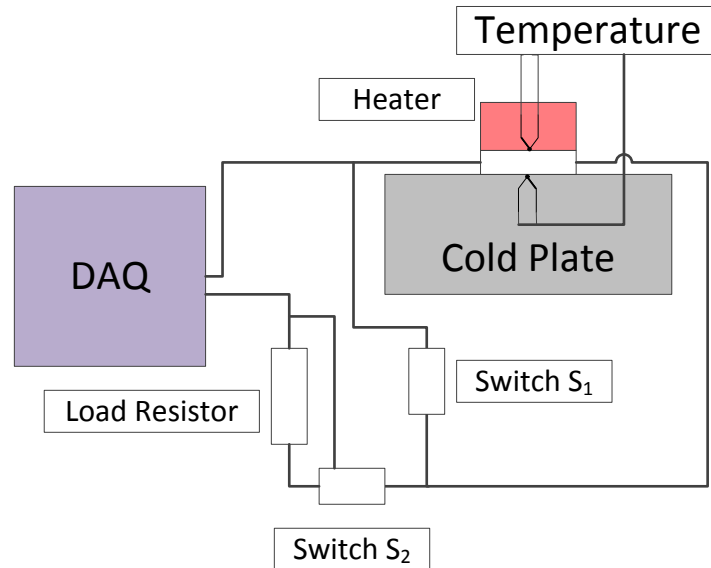
Figure 3.13: Schematic for the Gao Min approach

Voltages and temperatures are measured continuously using a DAQ system. The data obtained from the DAQ was compiled and compared with the data from the steady-state experiments. While the steady-state experiments were calculated applying a constant temperature difference across the module, in this case, the heater flux was adjusted so that the hot side temperature was maintained at 150ºC and the cold side temperature was controlled 50ºC under open-circuit conditions. The applied loading pressure was 690 kPa. These conditions mimic those used in the steady-state testing.

In comparing the results, the values of the figure of merit (ZT) and electrical resistance differ by 10–12%, while the value for conductivity differs by almost 25%. The Seebeck coefficient is almost the same, which can be explained by the fact that the method of calculation of the Seebeck coefficient in both methods is the same.

It was observed that two things would improve the accuracy of the results. The first was that better quality, well-calibrated components were necessary for accurate measurements of

electrical resistance. The second was that better control over the heater to maintain it at a constant heat flux was necessary.

Correcting the first issue was comparatively simple. Off-the-shelf and better quality components were used, and the experiment was carried with the same temperature difference (150–50ºC) and the same applied pressure (689kPa). The results were compared as follows:

Table 3.5: Comparison of Gao Min results with Steady state ones, showing the effect of well calibrated resistors

Property Measured	Gao Min Method	Gao Min Method (Calibrated)	Steady State
α (V/K)	0.045	0.046	0.044
R (Ω)	2.17	2.29	2.42
K (W/K)	0.85	0.67	0.63
ZT	0.43	0.43	0.47

The difference in results is much lower and within the acceptable range. Unfortunately, improved control of the heat rate was not possible for the preliminary test setup. This was an area of concern while transitioning to high temperatures. A high accuracy temperature control with power level control was necessary to achieve the required heat rate conditions.

3.4 Conclusion

Conducting preliminary testing was necessary to better understand the practical issues of the three different testing approaches, which in turn enabled determination of the the best approach for module characterization at high temperatures. The major problem with the steady-state approach is the difficulty in quantifying the heat losses to the surroundings, which will become increasingly more challenging at higher temperatures. A secondary issue with the steady-state approach is extremely long test times. The modified Harman method, which is based on passing

a current through the module, overcomes this issue, as it requires a shorter time to reach a steady-state condition. However, the biggest drawback to the modified Harman method is that it does not measure module parameters in actual working conditions. Another drawback is that the adiabatic conditions required for the "heat sunk" case will become increasingly difficult to maintain at higher temperatures.

On the other hand, the third approach using the Gao Min method was less problematic as it did not require the heat flux to be monitored but only maintained at a constant rate. However, this does have some of the same issues as the steady-state approaches where the heat losses to the environment could become significant at high-temperature testing. Controlling for this can be achieved more easily than maintaining a fixed temperature difference. Additionally, temperature differences can be measured more accurately. The drawbacks of this approach include long testing times and difficulty in judging whether the system has reached a steady state.

In conclusion, for high-temperature testing it was decided that a combination of the steady state and Gao Min methods would be utilized, thereby overcoming some of the challenges of both approaches. The new approach, called rapid steady state, is described further in the next chapter.

Chapter 4.   Design of the Test Apparatus

The focus of this chapter will be the thermal design of the system and description of the new approach developed the rapid steady-state approach. The new approach was based on the steady state, so similar limitations apply, with the most important one being accurate characterization of heat losses. The biggest advantage of the system was very short test times. This is especially important for long-term testing, where operating temperatures need to be maintained at a constant over a long period of time. Based on discussions with industrial partners, specifications for the new setup were created for successful testing of the next generation of thermoelectric devices.

4.1 Specifications

As modules at high temperatures have not yet been developed, the laboratories working on these modules were interested in a single setup that can accommodate a range of sizes. Prototypes developed by them were useful in determining the expected size and arrangement of the module. All the specifications provided are for the rapid steady-state approach.

Measurements

The measurements refer to the parameters that need to be calculated from the test. These will be used for comparison with the module properties. The measurements of interest are:

- Device level Seebeck coefficient (α)
- Device level overall electrical resistance (R)

- Device level overall thermal conductance (K)

- Peak power (P_{max})

Uncertainty

Uncertainty in a measurement is a parameter associated with the result of a measurement that characterizes the dispersion of the values that could reasonably be attributed to the quantity of interest [52]. In this case it is defined as an estimate of the error in the measurement stated as a range of values that contain the true value within a certain confidence level.

- Seebeck coefficient: +/–5%

- Electrical resistance: +/–5%

- Thermal conductance: +/–10%

- Peak power: +/–5%

The uncertainty in thermal conductance is assumed to be higher owing to the high uncertainty in power measurements.

Device sizes

The size range was taken directly from the laboratories. Forty millimeters was decided as the upper limit to accommodate low temperature validation for the module.

- 1–20 leg pairs (note there is no characterization of a single leg)

- 5–14mm device thickness (3–10mm leg lengths with 1–2mm substrates)

- 4–40mm device side lengths

Temperatures and environmental conditions

- All isothermal surfaces within +/−1°C

- Hot side temperature to be controlled from 100–650°C

- Cold side temperature to be controlled from 50–550°C

- No vacuum is required, but the ability to have a fully inert environment (i.e., argon or nitrogen purged) is necessary

- All temperatures are to be controllable to within 20°C

4.2 Build Overview

The greatest difficulty in testing the modules at the specified temperatures is the measurement of heat rates. A couple of alternatives were described in the literature review, with the first one being characterization of heat losses. At high temperatures, the radiation losses become dominant. These are very difficult to characterize, especially the surface-to-surface radiation component, which result in a large measurement uncertainty.

Another option is to use a heat meter in the form of a reference material placed in the path of the heat flow. This method has better accuracy and a comparatively lower uncertainty, but is not without issues. The biggest problem is the inherent uncertainty in published values of reference materials. Even for well-researched materials, the standard deviation in values is 5–10%. Calculating exact heat fluxes using a reference material relies on the measurement of the exact temperature difference along the sample length. Even the most reliable thermocouples have an uncertainty of ±2°C. This uncertainty propagates through to the heat flux measurement.

The last difficulty is predicting heat losses from the reference material. This can be minimized by placing the reference material or heat meter on the cold side so that losses are reduced. It was

decided that this method would be incorporated into the setup on the cold side as a check in the measurement of the heat flux, but not as the main source of heat flux measurement.

To overcome the potential errors of the above two approaches, a guard heater arrangement as described by Rauscher et al. [36,37] is used in the system. A guard heater arrangement is basically a smaller heater surrounded by a larger heater. The only exposed surface of the main heater is the face in contact with the thermoelectric module. The remaining sides of the main heater are enclosed by a guard heater. The main and guard heaters are maintained at the same temperature so that, theoretically, there will be no temperature difference between the main heater and guard heater and therefor no heat loss from the main heater block to the guard heater block. This also ensures 1-D conduction from the main heater to the module.

To enable control of the cold side of the module, a cold side heater arrangement is developed. This are explained in detail in sections 4.3 – 4.5.

Figure 4.1 depicts an overall schematic of the developed system. A thermoelectric module (4) is sandwiched between two heater blocks that maintain the temperatures on the hot and cold sides. Each heater block consists of a base heater (2) and swappable extension plate (3 and 5) to accommodate different-sized modules. The guard heater (1) surrounds the hot side heater block, ensuring 1-D conduction and eliminating heat losses from the main heater block. On the cold side, the cold side heater block (5) is connected to a spacer (6), which is connected to a water-cooled chiller plate (7). The assembly is supported on four linear bearings. Both heater blocks are insulated using alumina silica ceramic. A load cell (8) measures the pressure applied on the module by a hand crank (9).

Loading Assembly

Cold Side Assembly

Hot Side Assembly
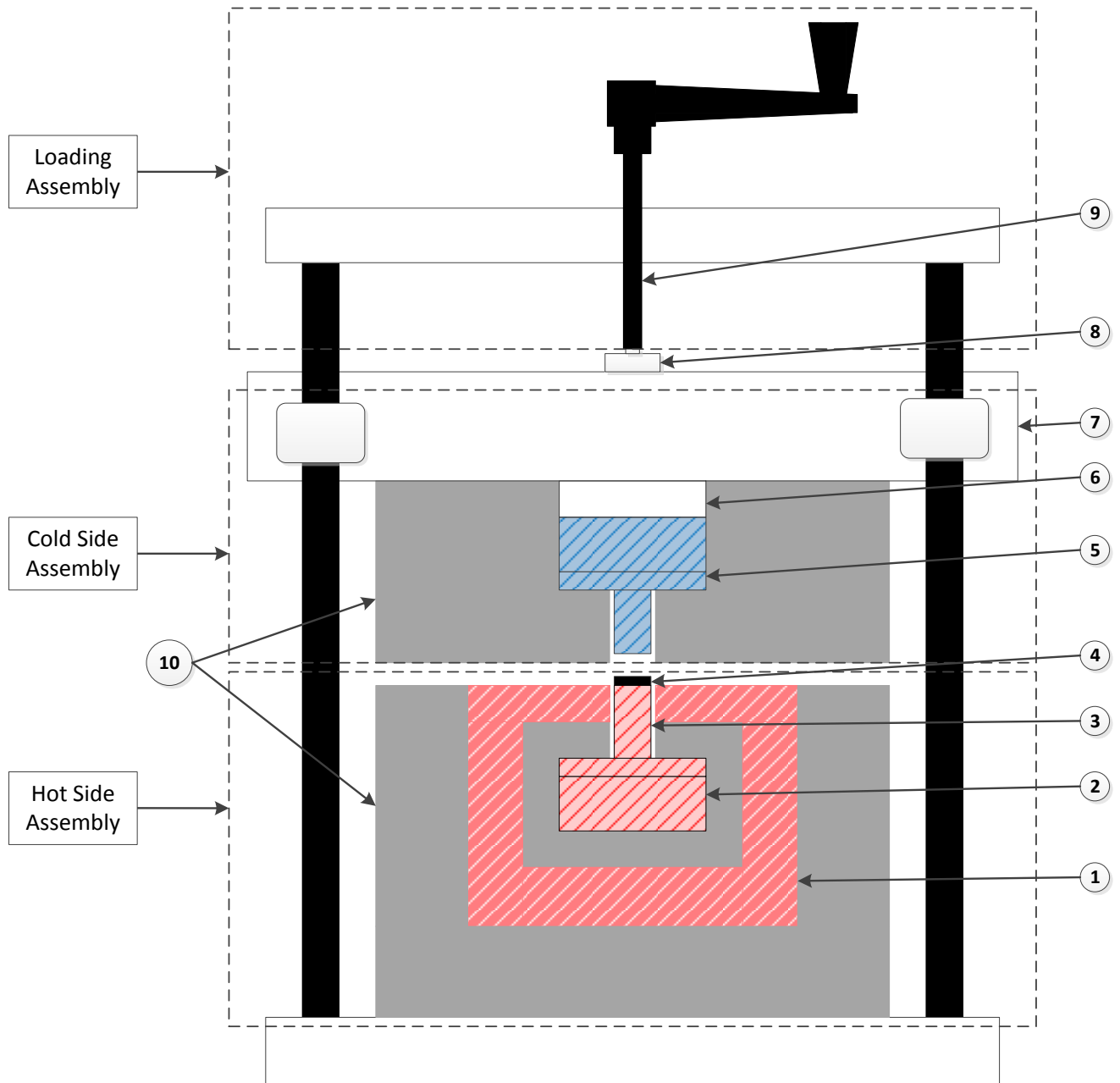
1 – Guard Heater Block
2 – Main Heater Block
3 – Main Heater Height Extension
4 – Thermoelectric Module
5 – Cold Side Heater

6 – Spacer Material
7 – Water Cooled Plate
8 – Load Cell
9 – Loading Screw
10 - Insulation

Figure 4.1: Schematic of the entire setup

4.3 Thermal Modeling

In order to quantify and then minimize the losses from the main heater block and ensure isothermal surfaces for a range of thermoelectric modules that might be tested, a thermal model of the concept system was developed. What follows is a description of the models developed for the various subsystems of the concept test stand.

Main heater assembly

The size of the main heater was decided upon by keeping in mind the maximum size of the module to be tested. As proof of concept, the existing modules, which have been previously categorized, will be tested on the setup. The size of these modules is 40mm x 40mm. Hence, the size of the main heater block is 40mm x 40mm x 20mm. The height selected will ensure an isothermal surface in contact with the module. Discussions with our industrial partners helped to identify a range of physical dimensions of the new modules, which the setup should be able to accommodate. Based on these values, four extreme cases were studied, and the specifications were developed. According to the dimensions, the device thickness could vary from 3–14mm and the number of leg pairs would vary from 1–20. When the module is not the same size as the heater, a small extension will be attached to the surface of the heater. The guard heater plate will surround the smaller extension, as shown in Fig. 4.4.

This configuration ensures that the heat from the heater flows only to the module and that there are no other losses. This extension will be thermally coupled with the heater and will be made of the same high-conductivity material. Consequently the surface of the extension block will also remain isothermal.

The setup is designed to test a thermoelectric module that contains multiple thermoelectric leg pairs. Going by this definition, the smallest thermoelectric module that can be tested by the setup would contain at least one leg pair. Testing of individual legs will not be possible. Feedback from the laboratories developing these modules helped define the size of each leg as 2mm x 2mm. Thus, the minimum size of the module that can be tested will contain one leg pair, with each leg having a 2mm square side. The overall size of the module can be varied by increasing the gap between the legs. The maximum size of a module that will be developed in the near future was estimated to have 20 leg pairs, also with each leg having a square side of 2mm.

Another limiting factor is the amount of current flowing through the system. High currents require expensive instrumentation, increasing the overall cost. As the leg pairs are electrically in series, the number of leg pairs does not affect the total current. The thickness or length of the legs is inversely proportional to the current flowing through them. Thus, the shorter the leg, the more the current flowing through it, assuming the area of each leg is constant. By keeping the maximum allowable value of the current as 15A, the minimum leg length for testing was calculated as 3mm.

The leg length also affects the amount of heat flowing through it—the longer the leg, the lower the heat rate flowing through it. For a particular temperature difference, the heat losses from the main heater block can be assumed to be constant regardless of the module size. As the leg length increases, the heat rate through the module becomes so low that they almost equal the heat losses from the main heater block. This leads to large uncertainties in the measured values. To avoid this situation, the maximum length was capped at 10mm.

Based on these values, the four extreme cases were considered:

- Case A: 1 leg pair with 3mm leg length

- Case B: 20 leg pairs with 3mm leg length

- Case C: 1 leg pair with 10mm leg length

- Case D: 20 leg pairs with 10mm leg length

For all cases, the dimensions of each leg were 2mm x 2mm.

To model the heat flux requirement of the main heater, the properties required were the thermal conductivity (λ) and the physical dimensions of the thermoelectric module. The module level Seebeck coefficient and the module level electric resistances were also calculated by using the Seebeck coefficients of the individual leg pairs (α) and the electric resistivity (ρ).

The schematic of the thermoelectric leg pair is shown in Fig. 4.2.
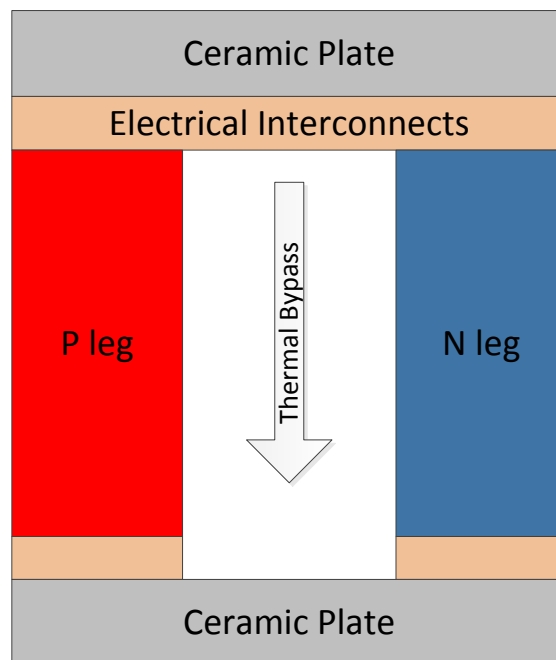
Figure 4.2 Schematic of a thermoelectric leg pair

Modeling

The heat flux calculation was done using the thermal resistances of the individual components of the thermoelectric module. The components formed a circuit, as shown in Fig. 4.3.
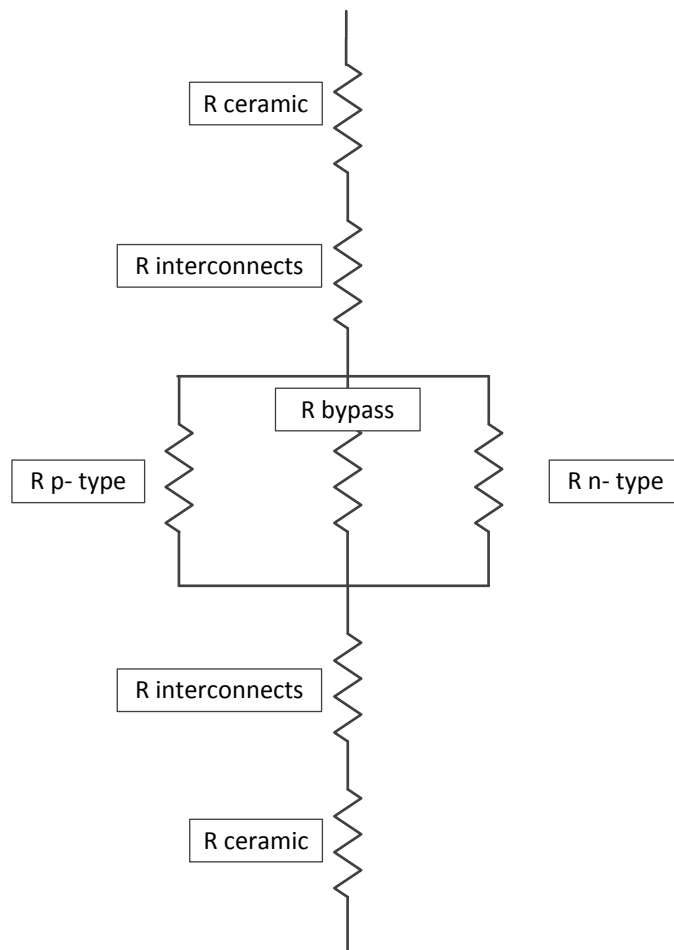
Figure 4.3: Thermal circuit of the module

Thermal resistances

1. *Ceramic plate*

To calculate the thermal resistance of the ceramic plate, the thermal conductivity was assumed to be 22W/mK. The dimensions of the plate were calculated assuming a 50% fill ratio, which

means that 50% of the module area was covered with thermoelectric material, while the remaining 50% was an air (or inert gas) gap. The length was assumed to be a constant of 1mm. The thermal resistance of the ceramic plate is

$$(R_{TH})_{cer} = \frac{L_{cer}}{K_{cer}A_{cer}}$$ (4.1)

2. *Electrical interconnects*

The interconnect material was assumed to be copper with a conductivity of 370W/mK. The dimensions of the substrate were also calculated using a 50% fill area, with a constant thickness of 0.5mm.

$$(R_{TH})_{int} = \frac{L_{int}}{K_{int}A_{int}}$$ (4.2)

3. *Leg pairs*

Using the material properties provided, the thermal resistances of the legs were calculated:

$$(R_{TH})_p = \frac{L_p}{K_p N A_p}$$ (4.3)

$$(R_{TH})_n = \frac{L_n}{K_n N A_n}$$ (4.4)

where the subscripts p and n represent positive-majority-carrier doped and negative-majority-carrier doped materials respectively.

4. *Thermal bypass*

Thermal bypass is the amount of heat that flows through the gaps between the leg pairs. As the gap is very small, there will be no heat transfer due to convection. But radiation and conduction

will be present in parallel. Using the conductivity of argon, the thermal resistance can be calculated as

$$(R_{TH})_{bypass} = \left(\frac{L_{bypass}}{K_{bypass}A_{bypass}}\right)^{-1} + \left(\frac{\sigma A_{bypass}(T_h+T_c)(T_h^2+T_c^2)}{\frac{1}{\varepsilon_1}+\frac{1}{\varepsilon_2}-1}\right)^{-1} \quad (4.5)$$

where ε_1 and ε_2 are emissivities of the two surfaces, assuming a large parallel-plates case.

Using the thermal circuit from Fig. 4.3, the overall thermal resistance is calculated as

$$(R_{TH})_{EQ} = 2 \times (R_{TH})_{cer} + 2 \times (R_{TH})_{sub} + \left(\frac{1}{(R_{TH})_P} + \frac{1}{(R_{TH})_N} + \frac{1}{(R_{TH})_{bypass}}\right)^{-1} \quad (4.6)$$

The module level conductance can be calculated as

$$K = (R_{TH})_{eq}^{-1} \quad (4.7)$$

The module level Seebeck coefficient is calculated as

$$\alpha_{p,n} = N(\alpha_p - \alpha_n) \quad (4.8)$$

And the module level resistance is calculated as

$$R = N\left[\left(\frac{\rho L}{A}\right)_p + \left(\frac{\rho L}{A}\right)_n\right] \quad (4.9)$$

Using the power equation for a module,

$$P_{TEM} = I\alpha_{p,n}(T_H - T_c) - I^2 R \quad (4.10)$$

Dividing both sides by the current (I), the module voltage can be obtained:

$$V = \alpha_{p,n}(T_H - T_c) - IR \quad (4.11)$$

Thus, for an open-circuit condition,

$$V_{oc} = \alpha_{p,n}(T_H - T_c) - IR \tag{4.12}$$

For a short-circuit condition, substitute $V_{sc} = 0$ in Equation (5.10). Thus,

$$I_{sc} = \frac{\alpha_{p,n}(T_H - T_c)}{R} \tag{4.13}$$

From Eqns. (5.11) and (2.7), the heat entering the module in a short-circuit condition is

$$(Q_H)_{sc} = I_{sc}\alpha_{p,n}T_H + K(T_H - T_c) - I^2{}_{sc}{}^R/_2 \tag{4.14}$$

This is the heat flux in a short-circuit condition, assuming a constant temperature difference.

If we substitute $I = 0$, which is the open-circuit condition, the heat entering the module is then

$$(Q_H)_{oc} = K(T_H - T_c) \tag{4.15}$$

Assuming that the module operates from 923K at the hot side to 373K at the cold side, the heat flux for the two extreme cases in short and open circuits can be obtained, then used to explore the range of heat rates needed and the relative impact of error in the main heater power losses.

Using Eqns. (4.7) - (4.9) and (4.12) - (4.15), module parameters can be determined as well as the range of required heat transfer rates to maintained the desired temperature differences for the four extreme cases of thermoelectric modules that might be tested in the current setup. The material properties used for this simulation can be seen in table 4.1.

Table 4.1: The Material Properties Used in Simulation of Extreme CasesTable

Property	p-type	n-type
α (V/K)	1.26E-04	-1.68E-04
ρ (Ω-m)	1.0E-05	1.0E-05
λ (W/m-K)	1.5	1.5

The results are summarized as seen in Table 4.2.

Table 4.2: Properties of Four Extreme Sizes of Thermoelectric Modules

Parameter	A	B	C	D
α (V/K)	0.00029	0.0059	0.00029	0.0059
R (Ω)	0.015	0.3	0.05	1
K (W/K)	0.004	0.08	0.001	0.03
Qsc (W)	4.30	86.08	1.38	27.53
Qoc (W)	2.25	45.01	0.76	15.21
I (A)	10.78	10.78	3.23	3.23
Voc (V)	0.16	3.23	0.16	3.23

The values of the current, voltage, and heat rates provide a basis for selection of instrumentation and heaters. Even though the voltages are quite small, the currents can be quite large for some modules.

Guard heater assembly

In the previously published literature, the guard heater was used to mainly minimize losses from the base of the guard heater. The losses through the size were assumed to be negligible by making the main heater as thin as possible. Even though this is a good approximation, it could lead to large errors at high temperatures. In the new system, the guard heater block covered all

sides of the main heater block. The proposed shape of the heater is shown in Fig. 4.4. The guard heater block is divided into four zones, depending upon its orientation and the materials with which it is in contact. Zone 1 is the base of the guard heater block, Zone 2 constitutes the sides, Zone 3 is the top plate of the guard heater block with the outer surface in contact with the insulation over the cold plate, and Zone 4 is the part of the guard plate exposed to the cold side heater through the insulation.

Insulation is present on both the inside and outside surfaces of the guard heater. The insulation on the inside will reduce thermal coupling of the guard heater and the main heater, which will reduce the heat loss to the guard heater block. The insulation on the outside will prevent excessive losses to the environment and therefore reduce the required guard heater power, as well as ensure more uniform temperatures throughout the guard heater.
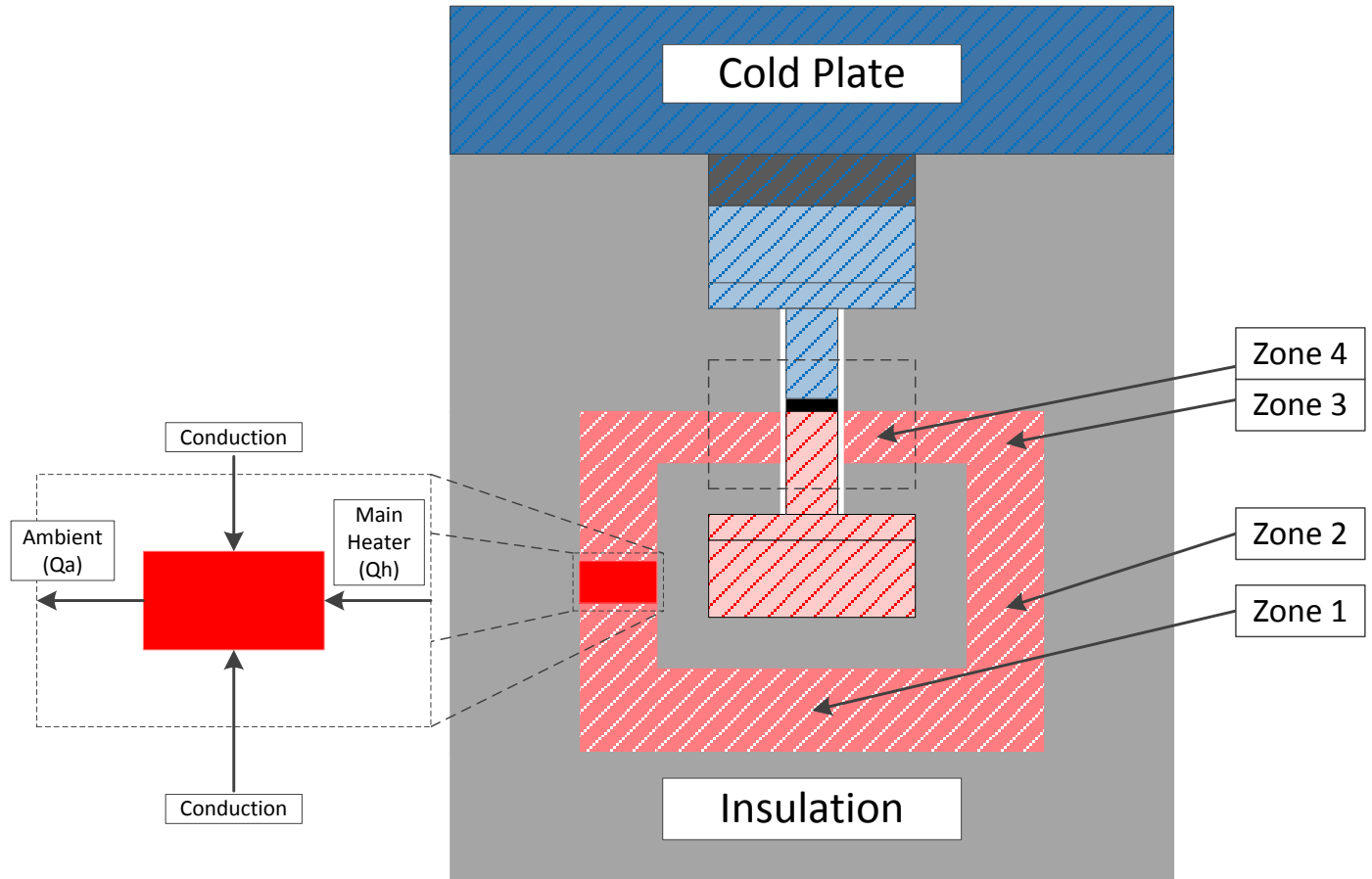
Figure 4.4: Guard heater schematic showing the various zones. Also shown is the discretization method of the guard heater

The overall dimensions were based on the insulation used as well as the material of the heater. A simulation in Excel was used to obtain the dimensions and an estimate of the losses, followed by a COMSOL and ANSYS simulations to predict the heat losses. With the Excel simulation, a finite difference method was used to calculate losses along the length of the guard heater. The fluxes were calculated for each section of the guard heater, then summed up.

For the analysis, it was assumed that the guard heater element was conducting heat to and from its adjoining elements and simultaneously losing heat to the main heater as well as the ambient

environment. Each element was assumed to be isothermal and constant conductivities and a

steady state for the entire system was assumed. To calculate the heat lost to the ambient

surroundings, the thermal circuit shown in Fig. 4.5 was used.
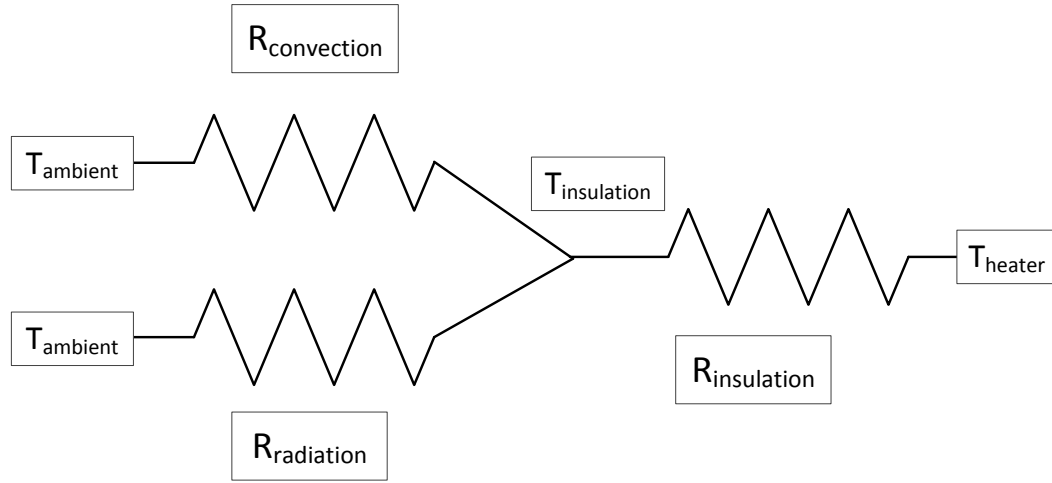
Figure 4.5: Thermal circuit for calculating insulation losses

Insulation losses for each discrete section are calculated by

$$(Q_a)_i = \frac{(T_{guard\ heater})_i - (T_{ambient})_i}{(R_{eq})_i} \qquad (4.16)$$

$$\text{where } (R_{eq})_i = \left(\frac{L_{outer}}{KdA}\right)_{insulation} + \left(\frac{1}{hdA + h_r dA}\right) \qquad (4.17)$$

$$\text{where } h_r = \varepsilon\sigma(T_{in} + T_{amb})(T_{in}^2 + T_{amb}^2) \qquad (4.18)$$

$$(Q_h)_i = \frac{(T_{main\ heater})_i - (T_{guard\ heater})_i}{(R_{th})_i} \qquad (4.19)$$

$$\text{where } (R_{th})_i = \left(\frac{L_{inner}}{KdA}\right)_{insulation} \qquad (4.20)$$

Furthermore, to keep the simulation 1-D, certain assumptions were made. It was assumed that for

the entire length of the guard heater, heat would be lost to the surroundings from the outer

surface and there would be heat gain from the main heater at the inner surface. The second

assumption was that the base of the guard heater is isothermal, and is the same temperature as the

main heater. Thus, there is no heat lost from the main heater to the top part of the guard heater.

The contact resistance between the guard heater block and the top plate was assumed to be

negligible. These assumptions make the simulation a little liberal. To compensate for this, it was

assumed that the main heater block is isothermal along its length, effectively overestimating the

heat losses. This assumption is valid for heater materials of high conductivity.

A simulation was run for an extreme case where the module is at 923K on the hot side and 373K

on the cold side. The module selected was with a single 4mm x 4mm x 10mm leg pair. It was

observed that for this case, almost 30% of the main heater power was being lost to the guard

heater. A simple fix to this is to maintain the guard heater block at a higher temperature than that

of the main heater block. The results obtained by holding the guard heater block at 1°C higher

than the main heater block can be seen in Table 4.3.

Table 4.3: Heat Losses Calculated (to the Main Heater and to Surroundings)

	Qh (W)	Qa (W)
Zone 1	0.13	18.61
Zone 2	-0.04	55.05
Zone 3	-0.09	13.91
Zone 4	-0.03	8.86
Total	-0.03	96.44

The negative sign for Q_h indicates that heat is gained by the guard heater. For the above case, the

losses dropped to 2% when the guard heater was held at a higher temperature. Also, as expected,

the heat loss to the main heater is much smaller than the heat loss to the environment. In the

subsequent sections, the heat flux required for such a small thermoelectric module is also calculated.

The simulation helped to determine the dimensions of the guard heater and the insulation. In the insulation design, the outer part was not as critical as the inner insulation. It was initially planned to have no insulation between the main and the guard heater blocks. This worked well at low temperatures, but as the temperature increased radiation losses also increased. Placing insulation between the two heater blocks made the radiation losses negligible. The thickness of the outer insulation was governed more by the overall mechanical design rather than the thermal design. A thickness of 20mm was selected for the outer insulation to maintain a safe outside surface temperature and keeping in mind the various design aspects.

For the inner insulation, it was observed that for thicknesses over 8mm, the radiation losses without the insulation were greater than conductive losses through the insulation. A 10mm thickness was selected for the inner insulation. Another advantage of insulating the inner surface is that the position of the main heater is secured.

There were two main objectives in selecting a thickness for the guard heater: the heat losses to the ambient environment should be as low as possible, and the temperature gradient along the length of the guard must be as low as possible. However, these objectives contradict each other. As the size of the guard heater block decreases, the heat losses to the ambient surroundings also decrease, so it is desirable to make the guard as small as possible. But as the guard becomes smaller, the temperature gradient along the length increases. This not only contradicts the second objective, but also increases the heat loss from the main heater to the guard. To optimize both objectives, a thickness of 15mm was selected for the guard heater.

The dimensions of the insulation and guard heater obtained from this simulation were used as a starting point for further analysis.

Cold side heater assembly

The cold side heater assembly includes the cold side heater, a spacer, and a liquid-cooled cold plate. A spacer is basically a block made of a material with enough thermal resistance that the liquid in the cold plate (water) stays below its boiling point. The spacer is designed for the expected heat rate exiting the cold side of the module under short-circuit conditions. This will ensure that the cold side heater is held at the required temperature even in the short-circuit condition. For the above case, (T_{hot}= 973K and T_{cold} = 373K), the cold plate was assumed to be at 323K (T_{cp}). The assembly can be seen in Fig. 4.6.

The thermal resistance of the spacer can be calculated as

$$R_{th} = \frac{T_c - T_{cp}}{(Q_C)_{sc}} \tag{4.21}$$
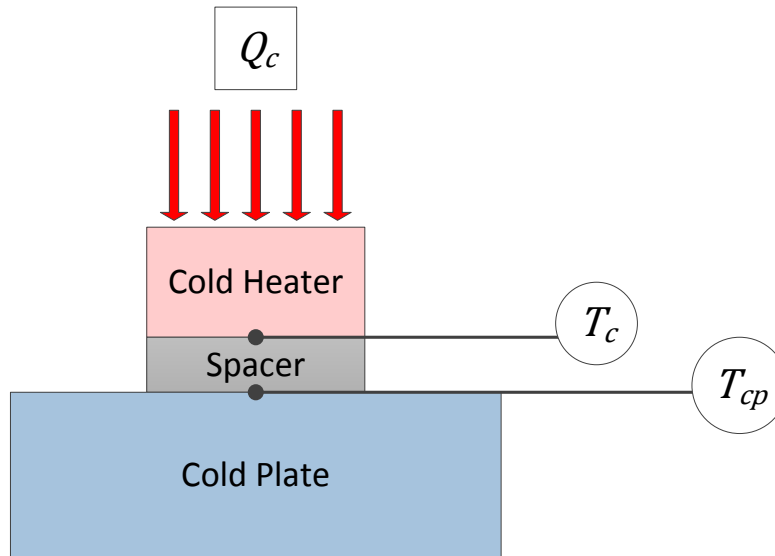
Figure 4.6: Cold side heater assembly

One drawback of the spacer design is that it is designed according to a fixed temperature difference. As the temperature difference changes, the cold side heater will have to compensate for the difference in heat flux. This can be seen in Table 4.4. The table is for the extreme module case under different operating temperature differences.

Table 4.4: Cold Plate Heat Flux for Different Temperature Differences

	Case A		
Th (K)	923	923	473
Tc (K)	373	823	373
Qh SC (W)	4.30	0.91	0.65
Qc SC (W)	0.00	42.13	3.65
Q_{cold} (W)	4.30	43.04	4.30

There is a large increase in the heat rate when the cold side temperature approaches that of the hot side. To accommodate such a large range, spacers of different thermal resistances will be needed. This can be achieved by varying the material of the spacer.

4.4 COMSOL and ANSYS Models

A numerical study was conducted in COMSOL and ANSYS to verify the values from the simple 1-D approach described above. A second objective was to verify that the surfaces adjacent to the thermoelectric module are isothermal.

Modelv

The overall dimensions for the guard heater, main heater, and insulation were taken from the preliminary model. The thermoelectric module was assumed to be 4mm x 4mm x 4mm. As stated earlier, the main heater was 40mm x 40mm x 20mm. The guard heater has a base

thickness of 20mm and a side thickness of 15mm. The top plate of the guard heater is 10mm thick and surrounded by high-temperature insulation of 20mm on all sides. The cold side insulation is 30mm to accommodate the cold side heater and the spacer. The insulation between the main heater and the guard heater was 20mm.

Materials

There were three different materials used in the simulation: the heater material, the insulation material and the spacer material.

To determine the best heater and guard heater materials, a material search was conducted, which resulted in nine options, shown in Table 4.5. The main criteria for selection are the three properties of thermal conductivity, specific heat, and density. The most important property required for the heater material is thermal conductivity. Because the heater blocks would be heated with the help of cartridge heaters, high conductivity will help reduce the temperature difference across the heater blocks and the height extensions. Secondly, as an important part of the experiment is based on the transients of the system, low specific heat and low density are also essential.

In the table, the maximum temperature refers to the maximum operating temperature of the materials without oxidization. Where oxidization temperatures were unavailable, the melting temperatures denoted by (MP) are stated.

Table 4.5: Material Options for Heaters

Name	Conductivity	Sp Ht	Max Temp	Density
	W/mk	J/kgK	°C	kg/m3
Potovell II: machinable nitride [53]	50	-	1000	2560
Aluminium nitride [54,55]	170	740	800	3260
Copper [56]	380	384.4	400	8960
Nickel [57]	91	445	1450	8908
Boron nitride [58]	71	1470	1300	1900
Silicon carbide [59]	120	750	1400	3100
Molybdenum [60]	139	251	800	10280
Beryllium oxide (Berlox)	265	1047	1800 (MP)	2850
Beryllium copper [61]	144	419	1100 (MP)	8800

With the complex geometries that need to be machined, coupled with machining ease and cost, copper was the best candidate. Unfortunately, copper does have oxidation properties at elevated temperatures. Copper starts oxidizing around 400°C and readily oxidizes above 500°C [56,62], limiting the range of testing temperatures. Thus, this was selected only for the first prototype of the setup, which would be used for low-temperature validation. For testing at 650°, the best choice of material was aluminum nitride owing to its high conductivity and relative ease of machining.

For the insulation material, cost and ease of machining were the two main criteria for selection, apart from the operating temperature. Alumina silica ceramic foam was selected, which has an operating temperature of 1650°C. It is easily machined and resistant to oxidization within its

operating temperature range. The spacer material was selected using the simulation. Stainless steel was selected as the material as it was the closest to the requirement in terms of thermal conductivity.

Boundary conditions

The material properties for copper and stainless steel were taken from the built-in materials library in COMSOL. The properties for the insulating materials were taken from the values provided by Cotronics Corp. for alumina silica ceramic. The material properties for the thermoelectric module itself, especially the conductivity, were calculated using the module level conductance from the preliminary model. Temperature boundary conditions were applied on the main heater block, guard heater block, and the cold heater block. The main heater and the guard heater were held at 923K and the cold heater at 323K. All the external surfaces of the insulation were assumed to be losing heat to the environment via convection and radiation. An overall heat transfer coefficient of 5W/mK and a surface emissivity of 0.5 was assumed.

Mesh

The results in COMSOL are extremely sensitive to the mesh size: the finer the mesh, the more accurate are the results. But as the mesh becomes finer, the computational time also significantly increases. To reduce the number of elements in the mesh, only half of the model was used for the simulation. Unfortunately, because there is a large variation in the sizes of the components of the setup, the number of elements in the mesh is numerous. Based on the resources available, only a medium overall mesh was possible, because of the high computational time required for rendering the fine meshes. To optimize resources, the local mesh for the heater height extensions and the thermoelectric module were made to be fine.

Post-processing

The problem was set up to simulate the working of a 4mm x 4mm module, operating at 923K on the hot side and 373K on the cold side. The solver selected was the standard generalized minimum residual (GMRES) solver, with 10,000 iterations and a termination damping factor of 1E-6. The resulting thermal contours can be seen in Fig. 4.7. Post-processing was useful in determining whether the surfaces were isothermal and calculating the heat losses.

The first step confirmed that the surfaces were isothermal, using the surface min and surface max functions for temperature. The values obtained for the hot side were 922.88K as the minimum and 923.27K as the maximum, giving an uncertainty of 923.1 ± 0.2°C. For the cold side, the minimum temperature was 373.27K and the maximum was 373.97K, giving an uncertainty of 373.6 ± 0.4°C. This is within well our specification of ±1°C.

The calculation of heat flux was slightly trickier. Due to the way the finite element method calculates the result, there is a significant error caused when the geometry domain changes shape drastically.
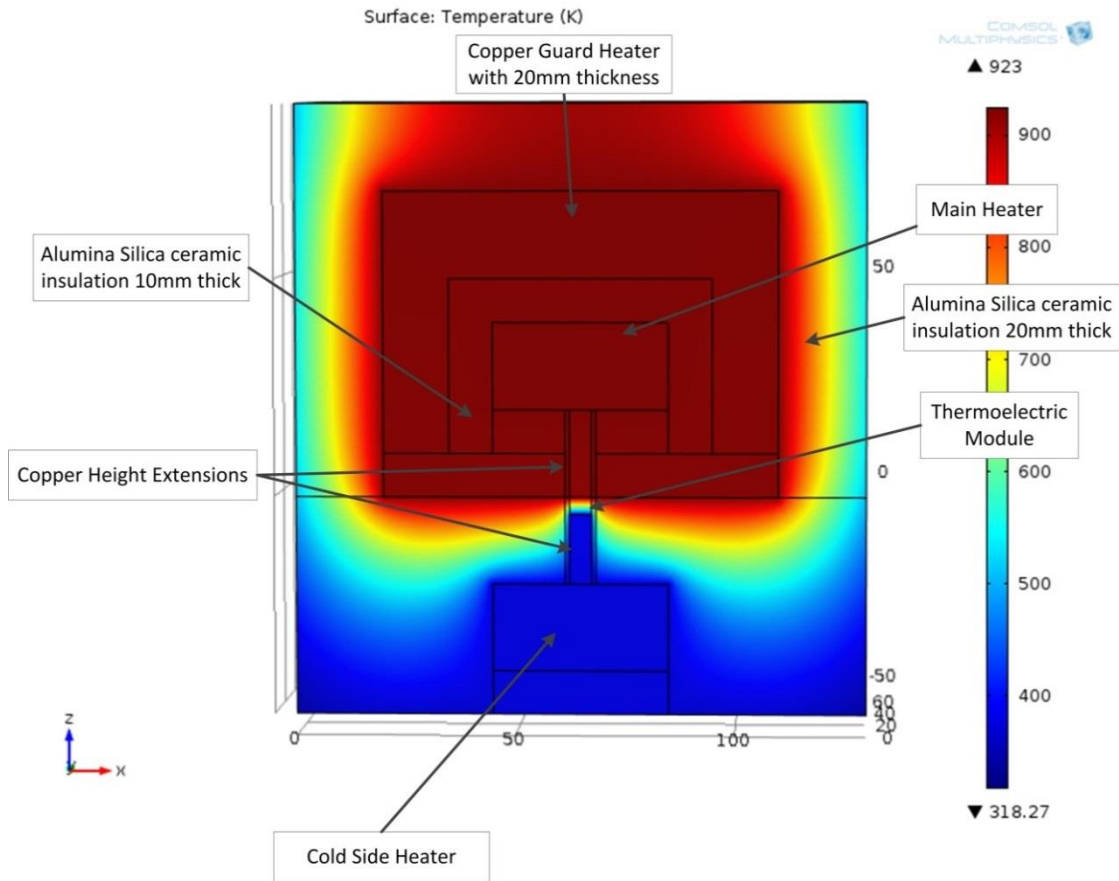
Figure 4.7: COMSOL simulation temperature distribution

Because the heat flux results were not exactly clear, the losses were calculated separately using a separate ANSYS simulation.

ANSYS modelling

A steady-state thermal system was used for the simulation. The geometry, material properties, and boundary conditions were kept same as those in the COMSOL simulation.
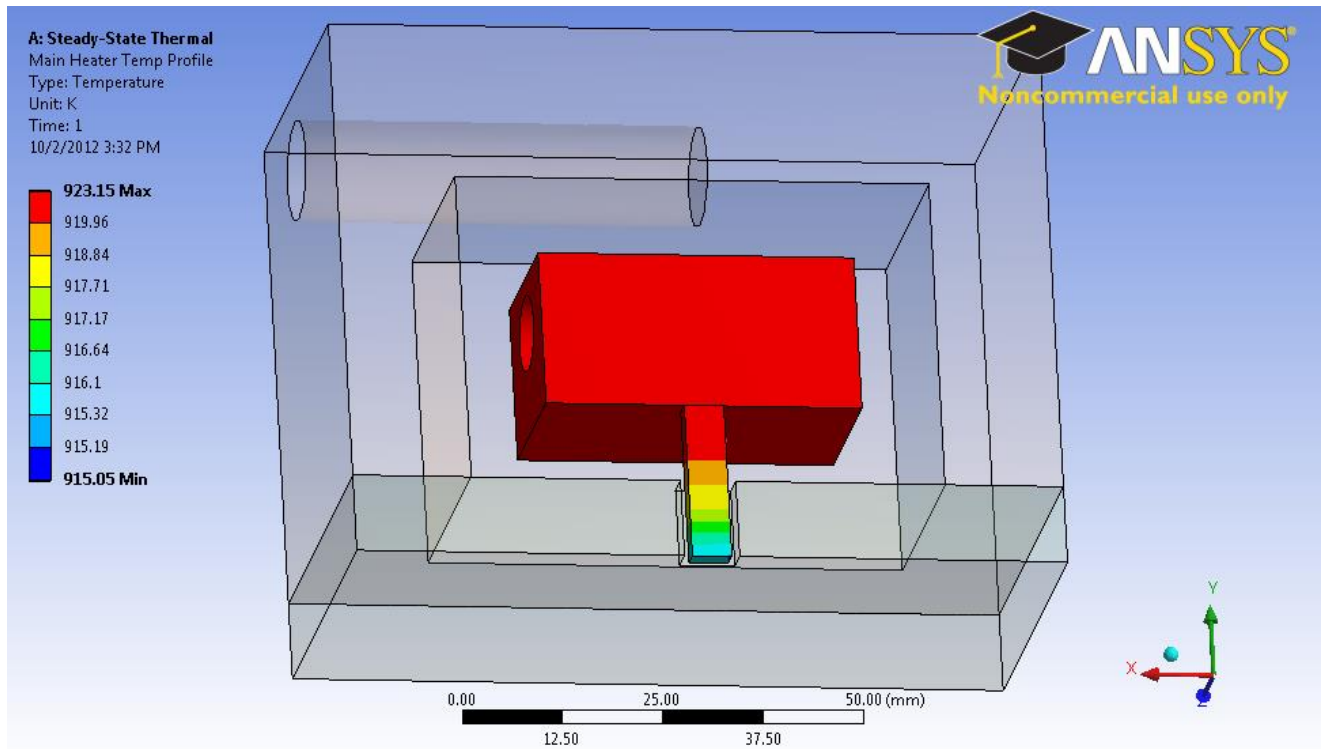
Figure 4.8: Temperature distribution across the main heater

Even at 923K, the surface of the height extension is isothermal within 0.5°C. Analysis performed on the main and guard heater assemblies indicated a temperature gradient of less than 8°C across the entire guard heater block under the worst case conditions, specifically when the hot side temperature is 650°C and the cold side temperature is 50°C. These temperature profiles were compared with those from the COMSOL simulation to calculate the heat losses from the main heater. Under this extreme case, the maximum heat transfer between the main heater block and guard heater was less than 2% of the heater power.

A: Steady-State Thermal
Guard Heater Temp Profile
Type: Temperature
Unit: K
Time: 1
10/2/2012 3:28 PM

924.71 Max
922.1
919.5
916.9
914.78
912.88
910.98
909.08
907.17
906.3 Min
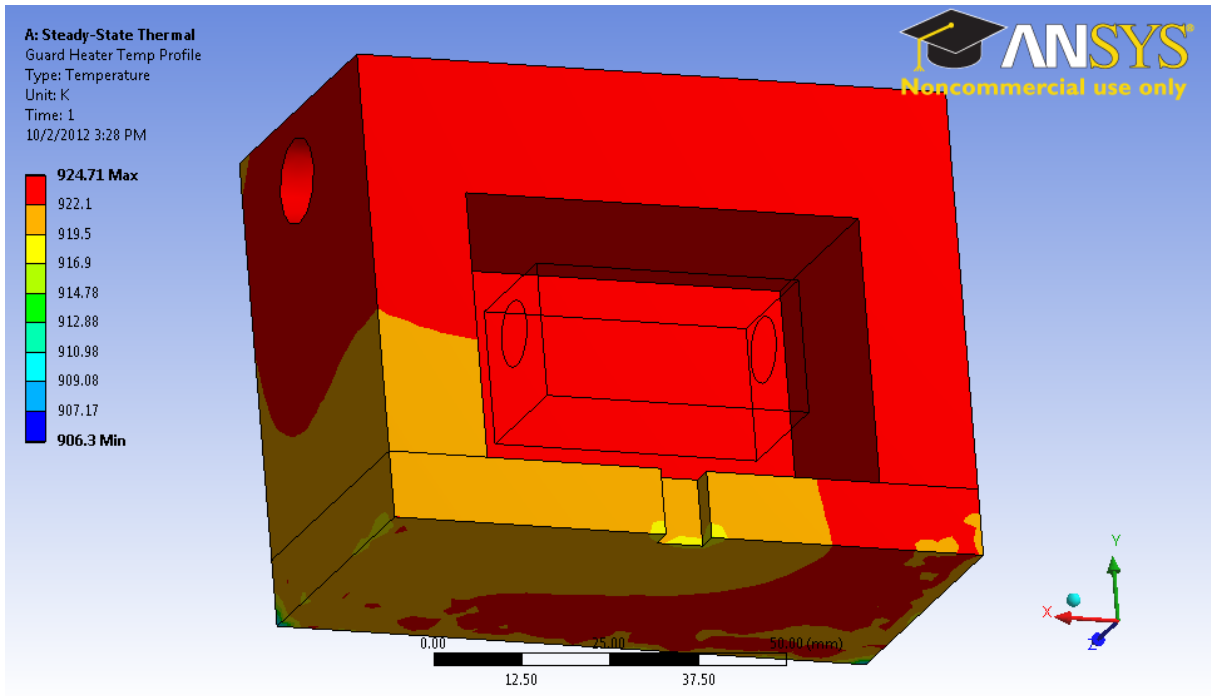
Figure 4.9: Temperature distribution across guard heater

The analysis was also used in selection of the cartridge heaters' size and placement, as well as selection of appropriate insulation. The selection criterion for the cartridge heaters was to achieve an isothermal surface of the main heater block. Keeping the worst case scenario in mind, two 200W cartridge heaters were selected for each of the hot and cold side blocks and two 400W cartridge heaters for the guard block.

4.5 Build Description

Hot side assembly

The hot side temperature of the thermoelectric module is maintained by the main heater block. Because there was interest in having the ability to characterize modules of different sizes, the main heater block is a composite of two parts: the base heater and an extension plate. Two PID-controlled cartridge heaters are inserted into the base heater block. These heaters were selected

such that the surface in contact with the thermoelectric module is isothermal. It is assumed that the entire power input to the heater is passing through the module. Compared to measuring heat flow, measurement of electric power is much easier, and precise measurement of the output from a module is possible [38]. In order to accurately determine the heat flow through the module and to ensure 1-D conduction, it is imperative that the heater extension plate be the same size as the module. The extension plate is customized for each module and is attached to the main heater block, and allows for testing of 4 mm x 4 mm to 40 mm x 40 mm thermoelectric modules using the same base heater. The heater block was made of copper with a flatness of 0.05mm.
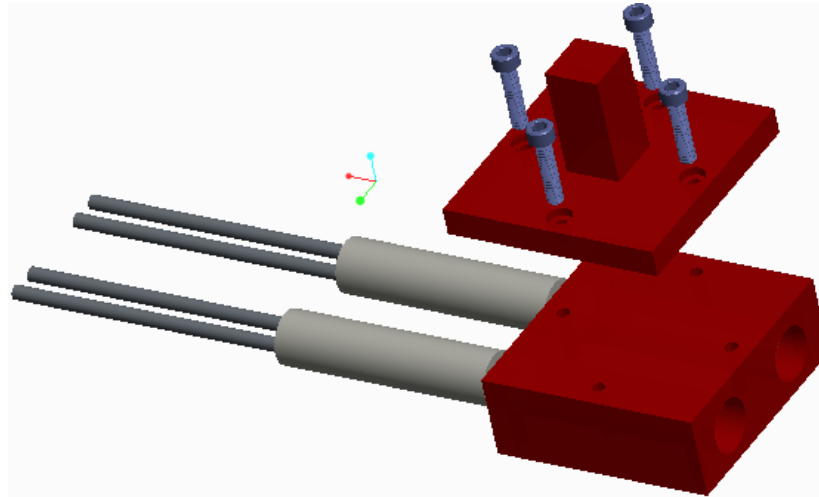
Figure 4.10: Main heater assembly

Because of its high thermal conductivity, copper was selected as the heater block material to ensure isothermal surfaces, ready availability, and ease of machining. Due to oxidation problems at higher temperatures [62], the next generation of the test stand will use boron nitride or AlN as the heater block material; both of which are stable up to 800˚C in air. Type K thermocouples, composed of chromel/constantan alloy and the most commonly used general-purpose

thermocouples, were used for all temperature control and measurements. These are stable in air or inert atmosphere up to 1260°C, have reasonable uncertainty, and are inexpensive.
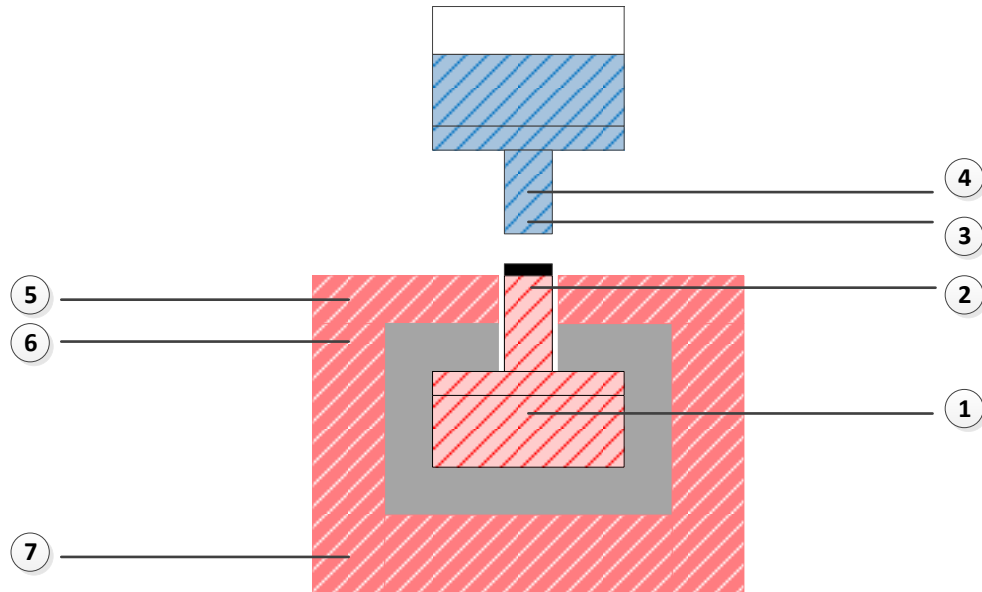
Figure 4.11: Sensing thermocouple placement in setup

Figure 4.11 depicts the placement of the sensing thermocouples in the setup. Thermocouples 1 and 2 measure the temperature gradient across the length of the main heater block. Thermocouple 2 is 2.5mm from the surface that contacts the module. Based on the heater power, a correction factor is applied to account for the temperature difference across the distance between the sensor and the surface. Thermocouples 3 and 4 measure the temperature difference along the length of the cold heater and are similarly corrected using correction factor. Thermocouples 6 and 7 measure the difference across the guard heater. Thermocouple 5 was placed in the guard plate to quantify any contact resistance between the guard heater block and the guard cover plate.

Figure 4.12 depicts the placement of the control thermocouples in the setup. Thermocouple A controls the temperature of the main heater, and is placed close to the heater cartridges to ensure that there is no temperature difference between the cartridges and the thermocouple. Thermocouples B and C are the guard heater control thermocouples. They are connected in a closed loop, and control the temperature of the guard heater by maintaining a constant temperature difference between the two thermocouples. Thermocouple D controls the temperature of the cold side heater and is also placed close to the heater cartridges.

Thermocouples E and F are emergency shutoff thermocouples and are placed on the main heater block and the cold plate. These are safety thermocouples, which shut down all power to the heaters if the temperature limit is reached. The hot side temperature limit is set to 450°C for preliminary testing, and the cold side temperature limit is 70°C to avoid boiling of the water.
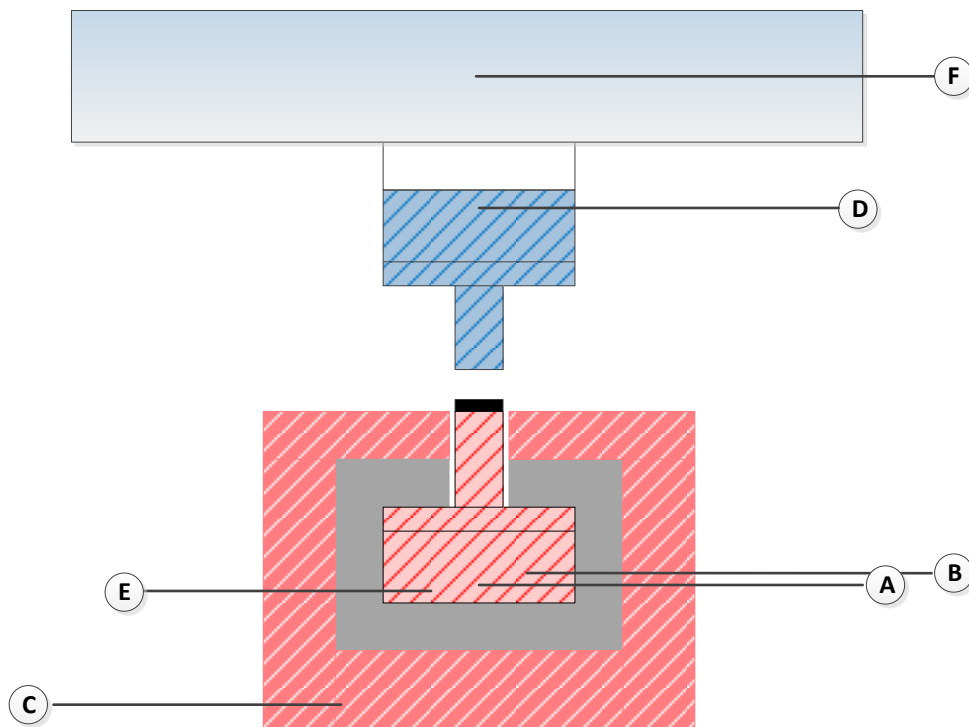
Figure 4.12: Control thermocouple placement in setup

Guard heater assembly

The guard heater, also made of copper, is shaped as a hollow cube, with a uniform thickness of 15mm around the sides and 20mm at the base, as seen in Fig. 4.12. It is mounted on the aluminum base with the help of four ANSI-304 screws, which are 20.5mm long. The screws help to secure the location of the guard heater block and also help to protect the insulation from breaking due to the thermal expansion of copper. The gap between the main heater block and the guard heater block is filled with alumina silica insulation to minimize thermal coupling, which is primarily due to radiation.

The top plate of the guard heater can be interchanged to facilitate different main heater extension sizes, and is sized so that the gap between the main heater extension and the plate is 1.5mm on each side. Thermocouples are placed along the length of the guard heater to calculate the temperature difference across the guard.

The guard heater arrangement was selected to achieve two main goals: to maintain an isothermal top surface of the main heater block and to prevent heat loss from the main heater block. During the experiment, a gradient of 2°C across the length of the guard was observed when the hot side temperature was maintained at 200°C and the cold side at 50°C. Due to this difference, there is a heat loss from the main heater block to the guard heater block. A suitable correction factor accounts for this loss while calculating the main heater power output. Because the heaters are most thermally coupled at the top plate, care was taken to maintain the top of the guard and main heater at the same temperature.

Cold side assembly

To enable control of the cold side of the module temperature between 75°C and 550°C, another heater block was placed on the cold side, similar in configuration to the main heater. The only difference between the hot and cold side heaters is that the height of the cold heater extension plate was adjusted to accommodate the thickness of the module. Modules varying from 2mm to 18mm thick can be tested. The size limits are stated keeping in mind the specifications provided by the manufacturers of the module. In reality, the setup can accommodate much thicker modules. A lower-conductivity spacer material, stainless steel, was placed between the heater and the water-cooled chiller plate to help maintain an appropriate thermal difference.

Like the hot side heater, two PID-controlled cartridge heaters were inserted into the heater block. Thermocouples 3 and 4 (Fig. 4.12) were placed at 10mm distance from each other with Thermocouple 3 being 2.5mm from the top of the cold heater block. These were used as a second method of measuring the heat rate passing through the module. In open-circuit conditions, the heat rate transferred to the module is equal to the heat rate leaving the module, which is measured using the thermocouples spaced at a known distance in a material with known thermal conductivity. This provides an additional check when calculating the heat rate.

Loading assembly

One of the important issues in module testing is to maintain a constant and even loading pressure and full surface contact across the entire thermoelectric surface. Four linear bearings guide the cold side assembly so that there is complete contact between the module and the heaters. The cold side assembly is supported by springs. The contact pressure is an important criterion to ensure repeatability in testing: therefore, a load cell is used to measure the pressure applied on the module. The movement of the assembly is controlled with the help of a threaded lead screw

that rests on the load cell. During the experiment it was observed that the optimal loading pressure is at or above 700kPa.

Inert environment

Testing in an inert environment is required for this stand, due to the susceptibility to oxidation exhibited by some high-temperature thermoelectric materials being considered for power generation devices. The stand was designed to be installed in a sealed enclosure to facilitate nitrogen or argon purging. The design incorporates the ability to easily remove the test stand from the enclosure for maintenance and to change the heater extensions.

There are four important parts: the enclosure, the gas tank, a pressure regulator, and an exhaust valve. The general schematic of the system can be seen in Fig. 4.13.
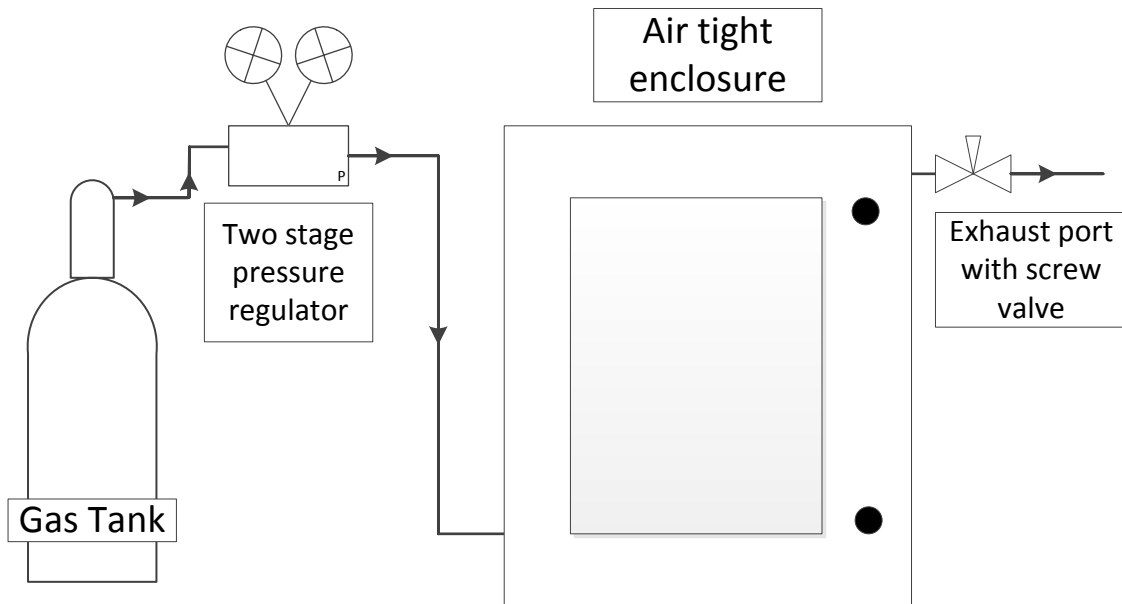
Figure 4.13: Schematic of the argon purging system

The figure shows an inert gas tank (either argon or nitrogen) connected to an airtight enclosure via a two-stage pressure regulator. Argon is preferred over nitrogen because of its purity. Nitrogen is generally produced by reverse osmosis of air and as such can contain some traces of oxygen, which may cause oxidation of the thermoelectric module. Another advantage of argon is that it is heavier than air. This reduces the number of air changes required to set up the inert atmosphere for testing. The two-stage pressure regulator converts the high-pressure liquid (over 400 psi) from the gas tank to low-pressure gas (about 3 psi) required at the enclosure. The inlet port for the argon gas is connected near the base of the enclosure, causing the lighter air inside the box to move to the top. An exhaust port consisting of a screw valve is attached near the top of the enclosure. This is used to exhaust any air inside the enclosure.

Of the four parts, the most important is the enclosure and it should meet the following criteria: The enclosure should be airtight so that gas does not leak; the steel grade should be high enough to withstand the internal pressure; the enclosure must be sturdy enough to allow passage of multiple electrical and plumbing connections through the wall; and it should be able to withstand ~80°C without failure. The enclosures that satisfy all these conditions fall into two categories, desiccators and NEMA boxes. Desiccators are basically industrial dryers that can withstand up to 250°C and have a large range of gas flow speeds. Their primary purpose is to purge nitrogen/inert gas. Although very well suited for the application, there is significant difficulty in making external connections. Thus, these have to be mostly custom-made by the manufacturer, raising the cost.

NEMA boxes are mainly electrical boxes available in various grades, with the airtight/watertight grade being NEMA 4/4X. These boxes come lined with a gasket material on the inside of the doors that will reduce leakages from the box. The NEMA 4 boxes are also made of 16-gauge

galvanized steel, so it can easily handle the resultant pressure. Additionally, they are easily customized post-purchase, and also have a viewing window to check for any leaks in the system. Keeping these factors in mind, a NEMA 4 enclosure of dimensions $30" \times 24" \times 12"$ was purchased. For electrical and water connections a side plate was mounted, with cutouts for the various connections. The side plate can be seen in fig. 4.14.
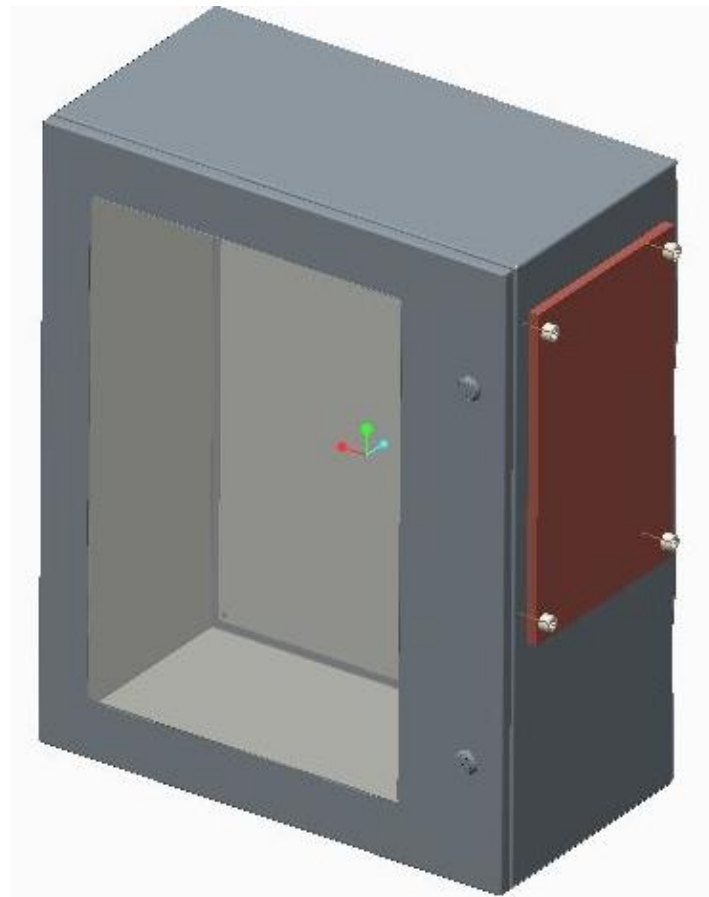
Figure 4.14: Inert gas purging enclosure

4.6 Troubleshooting

Base plate

The guard heater is supported on the base plate with the help of standoff screws. Even though these are made up of ANSI steel, which has a comparatively low thermal conductivity, the thermal coupling of the guard heater and the base caused the base plate to heat up. To avoid this, the base was fitted with a rectangular finned base. The fins selected ran along the entire length of the base plate. This reduced the temperature considerably to safe levels by increasing the heat dumped to the air. Figure 4.15 shows the standoffs the guard heater is mounted on, as well as the finned base attached.
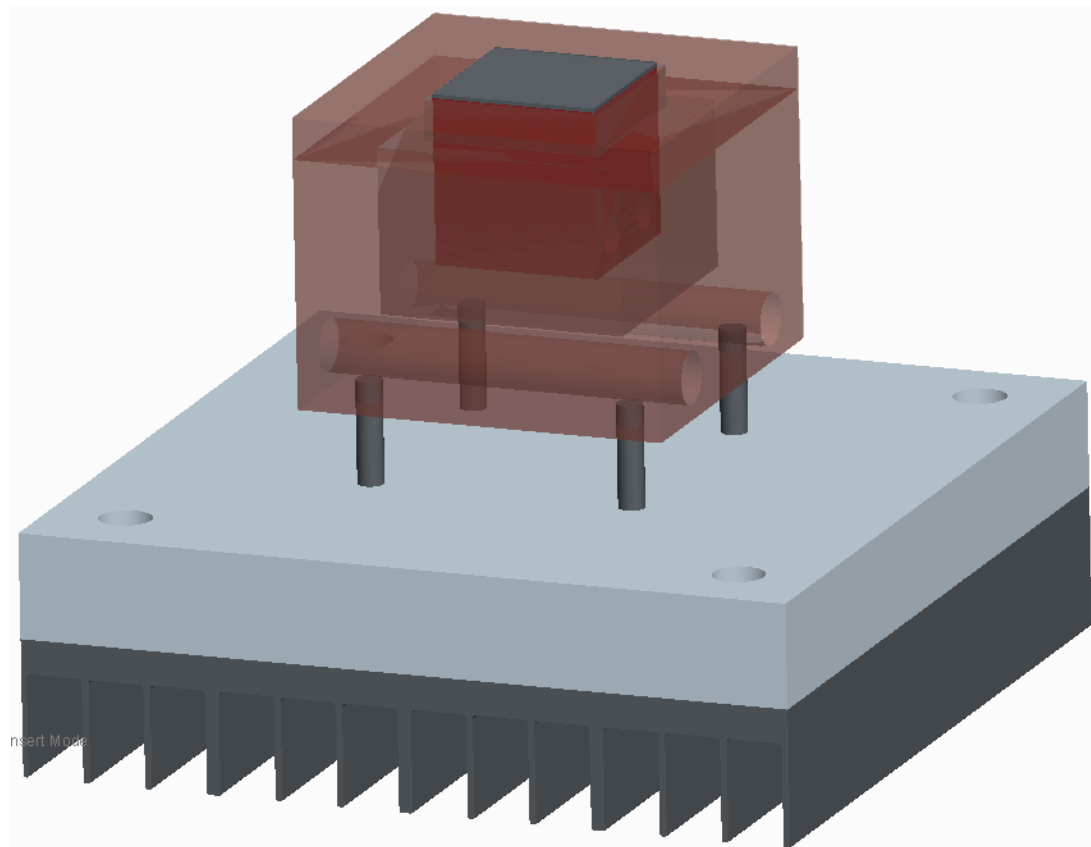
Figure 4.15: Guard heater arrangement with finned base

Guard heater

One of the changes in design was that of the guard heater. The need for a change rose when then cartridge heater's lead wires turned out to be too stiff to bend along the surface of the guard heater. To rectify this, two vertical slots needed to be machined on the side surface so that the heaters could slide in place. The design of the new guard heater is seen in Fig. 4.16.
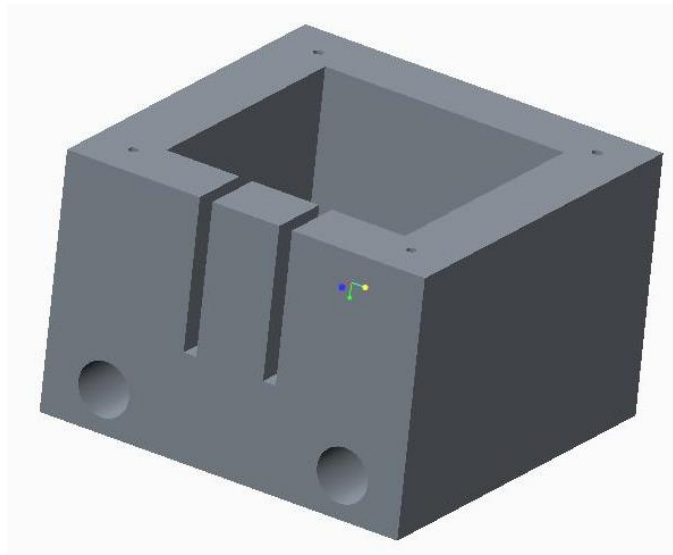
Figure 4.16: New design for the guard heater

The two slots enabled the guard heater to act as an extended fin surface. To account for heat lost from this surface, thermal analysis was performed in ANSYS. The boundary conditions were kept the same as described in section 4.4. The temperature contours for the guard heater showed that even with the slots in place, the temperature difference remained unaffected, as seen in Fig. 4.17.
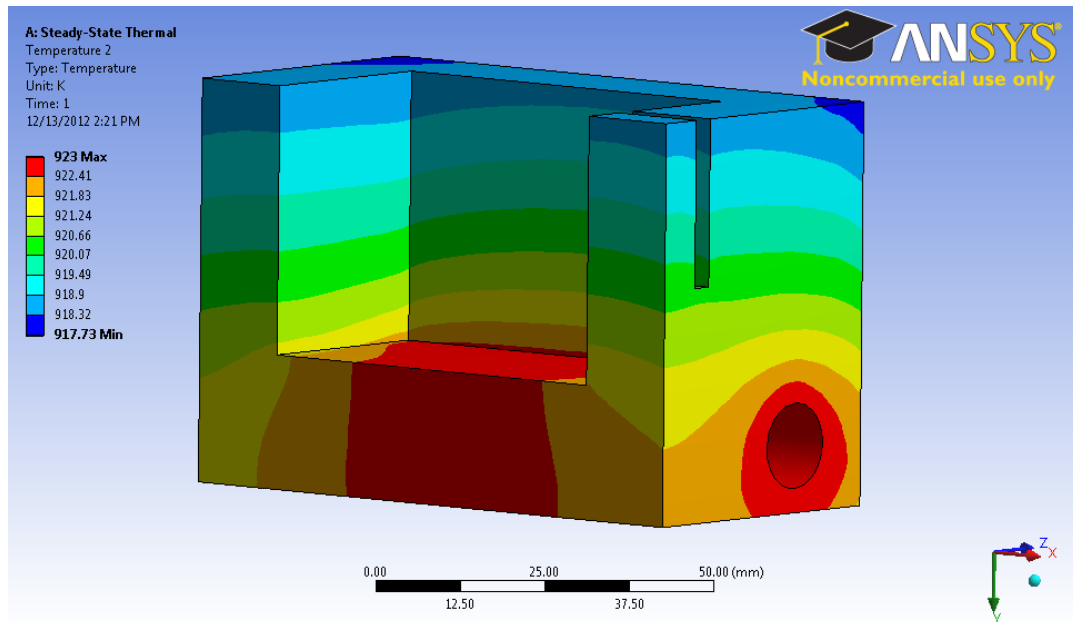
Figure 4.17: Thermal analysis on redesigned guard heater

Linear bearings

The linear bearings selected earlier were self-aligning bearings that had an allowable shaft misalignment of 1/2° in any direction. The combined effect of four such shafts resulted in the cold plate assembly not remaining perfectly horizontal while lowering. The perfect alignment of the cold plate assembly with the main heater was critical in the setup. To overcome this, a fixed alignment bearing was selected and installed.

Main heater assembly

The main heater consisted of two parts: the heater block into which the cartridge heaters were inserted, and the height extension plate, which was screwed in to the heater block. The arrangement was selected so that different module sizes may be tested using the same setup and only switching out the height extension plate. The main heater block was designed to use size 0-80 screws, which resulted in the maximum allowable size of the module to be 32mm. Due to the

physical constraints of copper, the 0-80 screws were switched to 4-40s. The larger screws reduced the maximum allowable size of module to 27mm.

Spacer material

In order to maintain the cold side at the required temperature, a spacer material was introduced between the cold plate and the cold heater. Analysis suggested selecting a material of thermal conductivity of 15W/mK. Thus, stainless steel, which has a comparable thermal conductivity of 16.23W/mK, was selected. Unfortunately, contact resistance was not taken into account in the analysis. Because of the large contact resistance between the surfaces, a higher conductivity material was required. For low-temperature testing, an aluminum spacer was selected.

Guard heater plate

After seeing the effects of contact resistance, it was decided to test for the same effects on the interface between the guard heater and the guard plate. A thermocouple was placed just below the plate and another was placed in the plate itself. Had there been a presence of a large contact resistance, a significant temperature drop would be expected across it. However, after running multiple tests, the temperature difference was observed to be less than 1˚C when the guard heater was held at 200˚C and the cold side was held at 70°C.

Heater controls

The control thermocouples for the main and guard heater blocks were near their respective cartridge heaters. As the main heater was in contact with the thermoelectric module, a temperature drop was developed from the control thermocouple to the sensing thermocouple, which was placed very close to the surface. In order to maintain the surface temperature at the required level, the control temperature was suitably increased. Similarly, the guard temperature

control was set with respect to the sensing thermocouple in the guard plate. This ensured that the top of the guard plate and the top of the main heater were at the same temperature.

Calibration of thermocouples

All K-type thermocouples have a minimum uncertainty of ±2°C. In order that all the thermocouples read the nearly the exact temperature over a large temperature range, it was necessary to calibrate them. A simple setup was used for the calibration: an aluminum block was fitted with a cartridge heater with the sensing thermocouples inserted into holes drilled on its face. The aluminum block was heated at 50°C intervals from 50–400°C and fully insulated to ensure negligible temperature differences in the block. All readings were imported into LABVIEW and the temperatures then calibrated based on the readings from an unused thermocouple, which was recently purchased and used as a master reference thermocouple. The setup can be seen in Fig. 4.18.
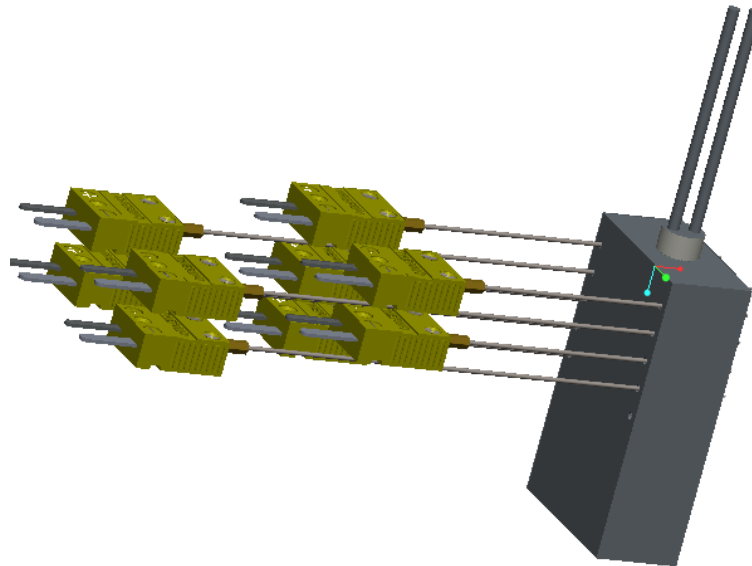
Figure 4.18: Thermocouple calibration setup

4.7 Rapid Steady-State Test

The approach used for testing is based on the steady-state approach, similar to the one used by Sandoz-Rosado and Stevens [34]. The difference lies in measuring the electrical characteristics of the module. The new method proposed uses a rapid steady-state testing approach, in which the module is electrically loaded and unloaded over a very short time span to avoid the thermal response due to Peltier cooling and a thermal drift. The loading is done using a Kukusi PLZ164WA programmable electronic load. By scanning multiple loading points while measuring the module current and voltage, the hot side and cold side temperatures, and the input thermal power, the device level Seebeck coefficient, the electrical resistance, thermal conductance, peak power, efficiency, and module level thermoelectric figure of merit can be determined. Tests were carried out at various loading pressures and temperatures, and a platform for characterizing module performance was developed.

Thermoelectric model

The thermoelectric module hot side heat transfer rate is modeled by assuming 1-D heat flow and steady-state conditions [34] and can are given by Eqns. (2.7), (2.8), and (2.10).

The voltage response of a module can be obtained by dividing the power equation of a module, Eqn. (2.10), by the current, I:

$$V = \alpha(T_H - T_C) - IR \qquad (4.22)$$

Once a steady state is reached, the rapid scan at different electrical loads can be performed. The three device level parameters that fully characterize the device can be extracted by using only two points on the scan: a short-circuit current and an open-circuit voltage, along with the hot side

heat rate under open-circuit conditions. However, a scan over many operating points along the voltage-current curve improves confidence in device parameter measurements, especially around the peak power point, which occurs at half the open-circuit voltage or at the middle point of a typical scan.

Electronic load

Changes in the load voltage will cause a change in the temperature difference due to the Peltier cooling and heating at the module junctions. For steady-state testing, the practical consequence is that for a traditional steady-state test approach, time must be allotted for each step change in electrical load applied to the module. Each change to the electrical loading condition will result in a different level of Peltier cooling or heating on both sides of the module, and therefore impact the local temperature at the junction until the temperature control system adjusts the heater power to bring the temperature gradient back to the one prescribed. Although changes in the electronic load happen almost instantaneously, the change in temperature difference is gradual. This is the principle behind transient test methods [26]. The rapid steady-state method avoids this thermal drift issue by using very short load durations. Models and experiments confirmed that for steps of less than 20ms in length, the thermal drift and therefore error of the measurement of thermoelectric properties is negligible. This transient thermal drift can be seen in Fig. 4.19, when the load current was changed for two different step sizes. In the 300ms step, the Peltier cooling caused a change in the voltage because of the change in junction temperature, while in the 10ms step there is a negligible change.
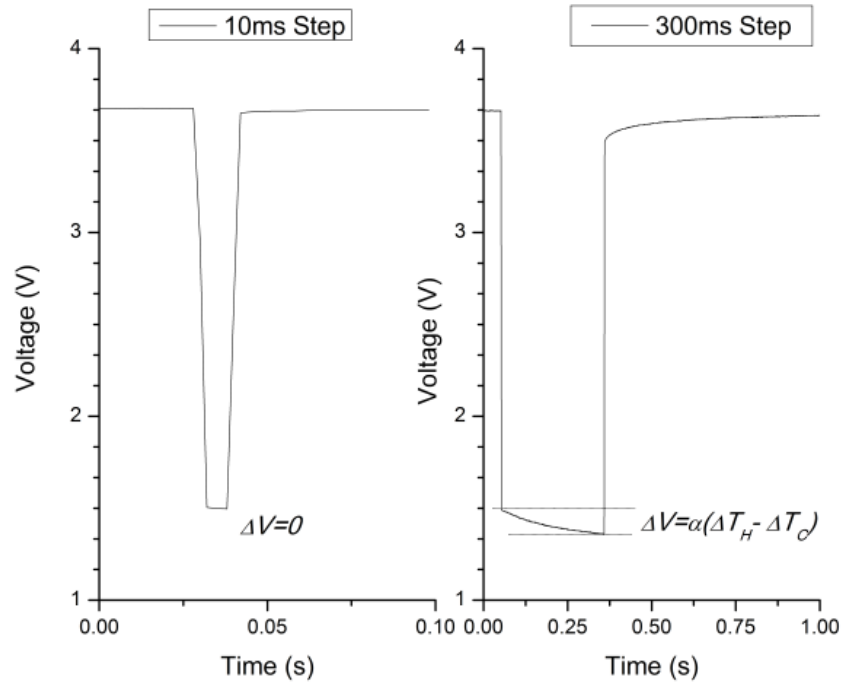
Figure 4.19: Temperature dependence of voltage with an increase in time step

To scan the voltage-current relationship for a module, an electronic load with constant current control is used. A scan consists of sweeping through a specified number of current values from 0A to the short-circuit current, which is measured before the scan by operating the module at zero voltage for a short period of time. At each probe point, the electronic load is programmed to apply each current of interest for a short time (e.g., 10ms), then return to the initial load. Figure 4.20 shows the voltage response to several applied current steps for a typical sweep. The first step in the figure is the short-circuit loading condition.
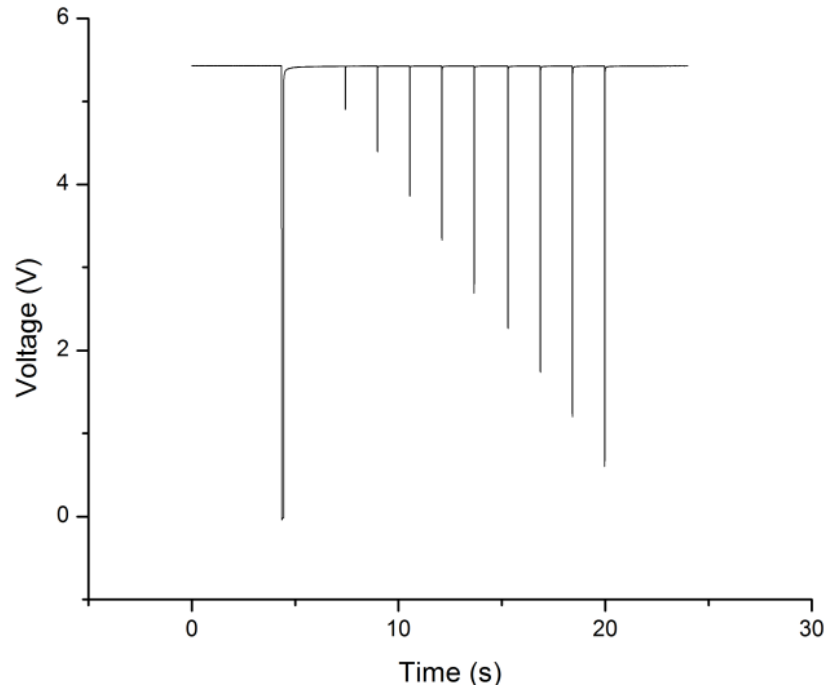
Figure 4.20: Voltage response for applied current at 10ms time step

The applied current and its corresponding voltage response are plotted and a linear function is fitted to the data. From Eqn. (4.22) it is clear that when the temperature difference applied across the module is constant, the electrical resistance can be calculated using the slope of this fit. The y-intercept and temperature difference are used to calculate the Seebeck coefficient. A typical plot can be seen in Fig. 4.21.

$$\alpha = \frac{V_{OC}}{\Delta T} \tag{4.23}$$
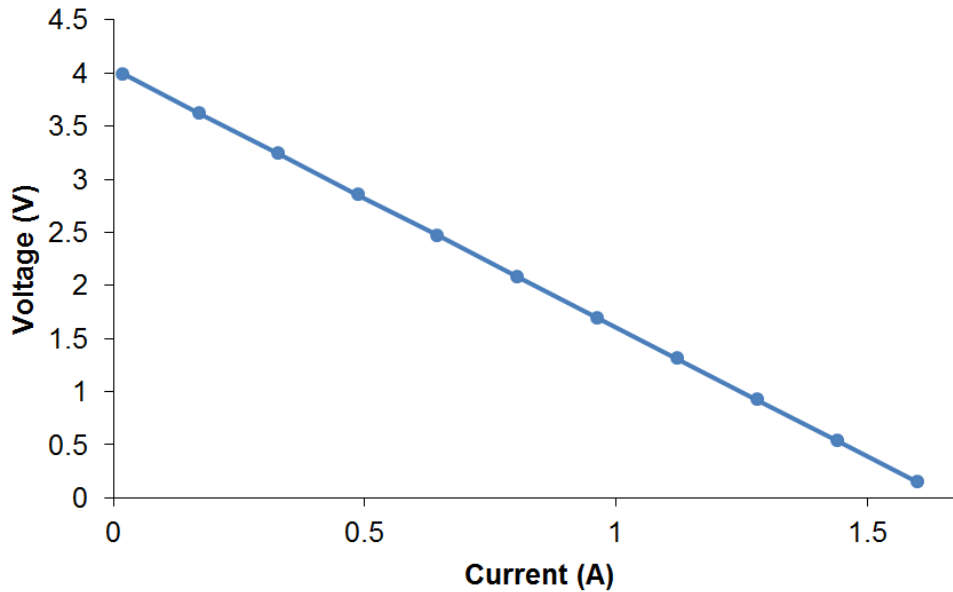
Figure 4.21: Current-voltage scan and linear curve fit for a 100°C temperature difference, with the hot side and cold side temperatures being 170°C and 70°C, across a typical BiTe module

The thermal conductance for the module can be expressed as the ratio of the actual heat rate delivered to the module to the temperature difference across the module when the module is in the open-circuit state, given by Eqn. (4.24).

$$K = \frac{Q_H}{T_H - T_C} \qquad\qquad (4.24)$$

Electronics

The main component of the rapid steady-state testing is the electronic load. For quick switching of loads, a Kukusi PLZ164WA programmable electronic load was selected. For this model, the switch time between loads is 10μs, enabling the user to program sequences, which is essential in performing a scan. LABVIEW drivers are readily available for this unit and it has the capability of measuring voltage using a separate set of wires to avoid voltage drops that will occur in the current carrying conductors. As its current range is 0–30A, it satisfies the high current requirement for the extreme cases. Most electronic loads do not go to 0V, which is required for

the short-circuit condition. With the Kukusi PLZ164WA, it was possible to reach 0V exactly, thus making testing of the Gao Min method possible for future testing.

The input power was monitored by measuring the instantaneous current and voltage supplied to the main heater using a 10mΩ shunt resister and a 25:1 DC voltage transducer. An Ohio Semitronics VT7-006D DC transducer was selected because of its ability to handle 60Hz speed and drop the voltage to under 10 VDC, which is assessable by the selected DAQ system. The product of the instantaneous voltage and current provides instantaneous power, which is averaged over several minutes to ensure an accurate average power measurement.

For temperature control, a Watlow EZ-Zone PM controller-6C1CA was selected. This PID controller can control temperatures remotely via LABVIEW and maintain the temperature within 0.1°C. The main advantage of this unit was the control of the guard heater, as it allowed the guard heater to be controlled either by a temperature level, a temperature difference, or a set power level. The switching of the heaters was controlled by a Continental Industries SVDA/3V10 solid-state relay. The two limit switches selected were Watlow EZ-Zone LV limit Controller-LVCDLW00001000s. These were connected to an LED light to indicate that temperatures have crossed acceptable limits. Tripping the limit switches also shut off power to all heaters.

To measure the loading pressure, a compression load cell made by Measurement Specialities Inc., model MSP6953-ND was used. The load cell had a capacity of 500 pounds with a maximum shock loading of 1000 pounds. It was selected because of its compact size, high reliability, and sensitivity.

Finally, to calibrate all instrumentation, a Kiethley model 2000 digital multimeter was selected. It provides 6½ digit accuracy and offers exceptional measurement speed at any resolution, and has a voltage range of 100nV–1kV and a DC resistance range of 100μΩ–100MΩ [63]. The multimeter is factory calibrated for the first two years.

Data acquisition

To record temperatures, a National Instruments USB-9213 16-channel thermocouple reader was used. It was selected because of its high accuracy and built-in cold side compensation. A National Instruments Series X USB-6341 with 32 analog input channels also was selected for all other data acquisition because of its excellent precision, high sampling rate, ability to excite load cell bridge, and has a wide range of voltage measurement options. Both NI instrumentation had full collections of LABVIEW drivers making them easy to incorporate in a fully integrated data acquisition system. A LABVIEW virtual instrument program was created to control and record data. Figure 4.22 shows a screenshot of the VI created for the test. Box 1 contains the heater ontrols for the main heater block, guard heater block, and the cold heater block.
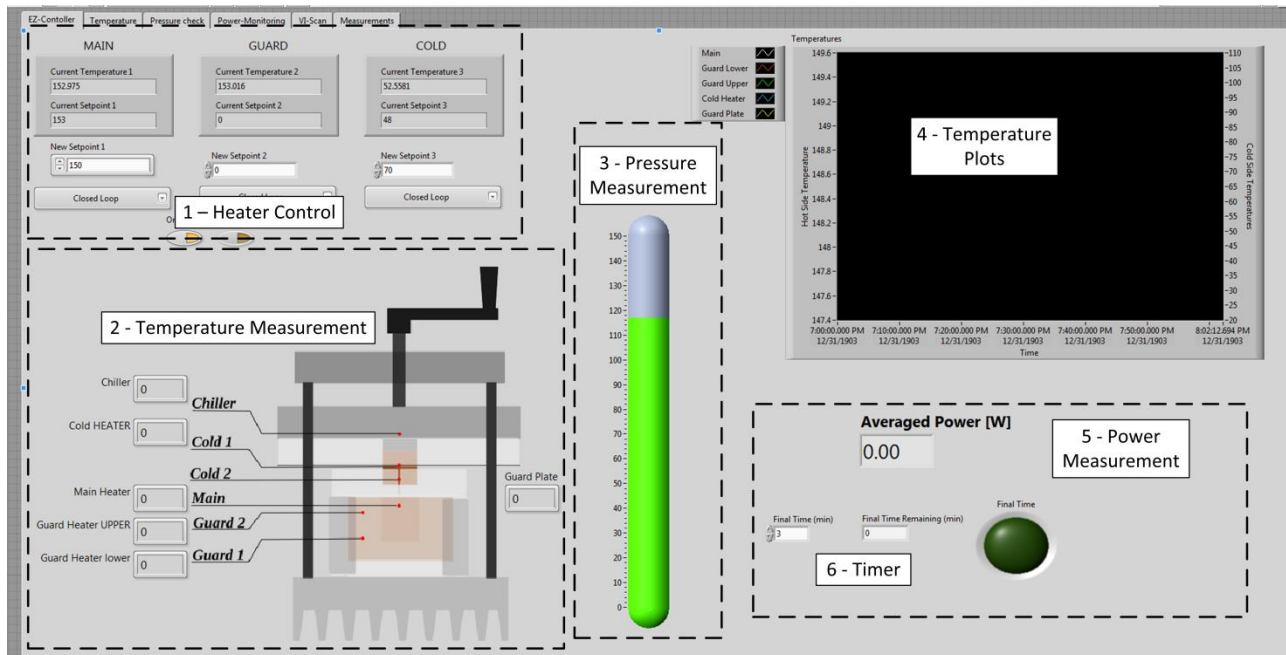
Figure 4.22: Screenshot of the LABVIEW program

Three options for temperature control are provided: by temperature, by temperature difference, or by power level. An off switch turns off the power to all of the heaters. Box 2 represents a temperature measurement box and provides the instantaneous temperature for all of the attached thermocouples. The temperatures are displayed in degrees Celsius. The data is also stored simultaneously in a data file.

Box 3 shows the instantaneous pressure acting on the module. The pressure is displayed in kPa and the standard loading pressure is 700kPa. As a warning, the pressure display turns red above 900kPa to provide a visual cue that the module is being overloaded.

Box 4 shows plots of the temperatures seen in Box 2 to observe any trends in the measurements. Box 5 shows the power measurement averaged over a period of time. Experimental data has shown that the power measurement is constant after a couple of minutes. To ensure that spikes in measurement are averaged out, the power displayed is averaged over three minutes.

The timer box is the time set by the user to allow the test stand to reach a steady state. The main heater block and the cold heater block reach a steady state very quickly;, the guard block takes a long time. For the experiment, a time of 30 minutes was assumed to be long enough to reach a steady state. When the timer reaches zero, the module scan is started automatically. On finishing the module scan, the power measurement is triggered.

The test is started by setting the required temperature difference in Box 1, and setting the time in the timer box. When the time runs out, the module scan and the subsequent power measurements along with the temperature are written to an Excel file. This data is used in calculating the module properties. The testing procedure is explained in detail in appendix A.

The new testing approach can be used for modules as well as materials. Due to the rapid loading and unloading during the scan, the test time was reduced from about 20 minutes (in case of a steady state) to about 20 seconds after the module reaches steady state conditions.

Figure 4.23 shows the test stand in the center placed inside an inert gas enclosure. The control box on the right helps maintain the desired temperatures and also includes the emergency shut offs. The DAQ devices and the electronic load are placed on the left. And finally, the Kiethley multimeter was used to calibrate the instrumentation.
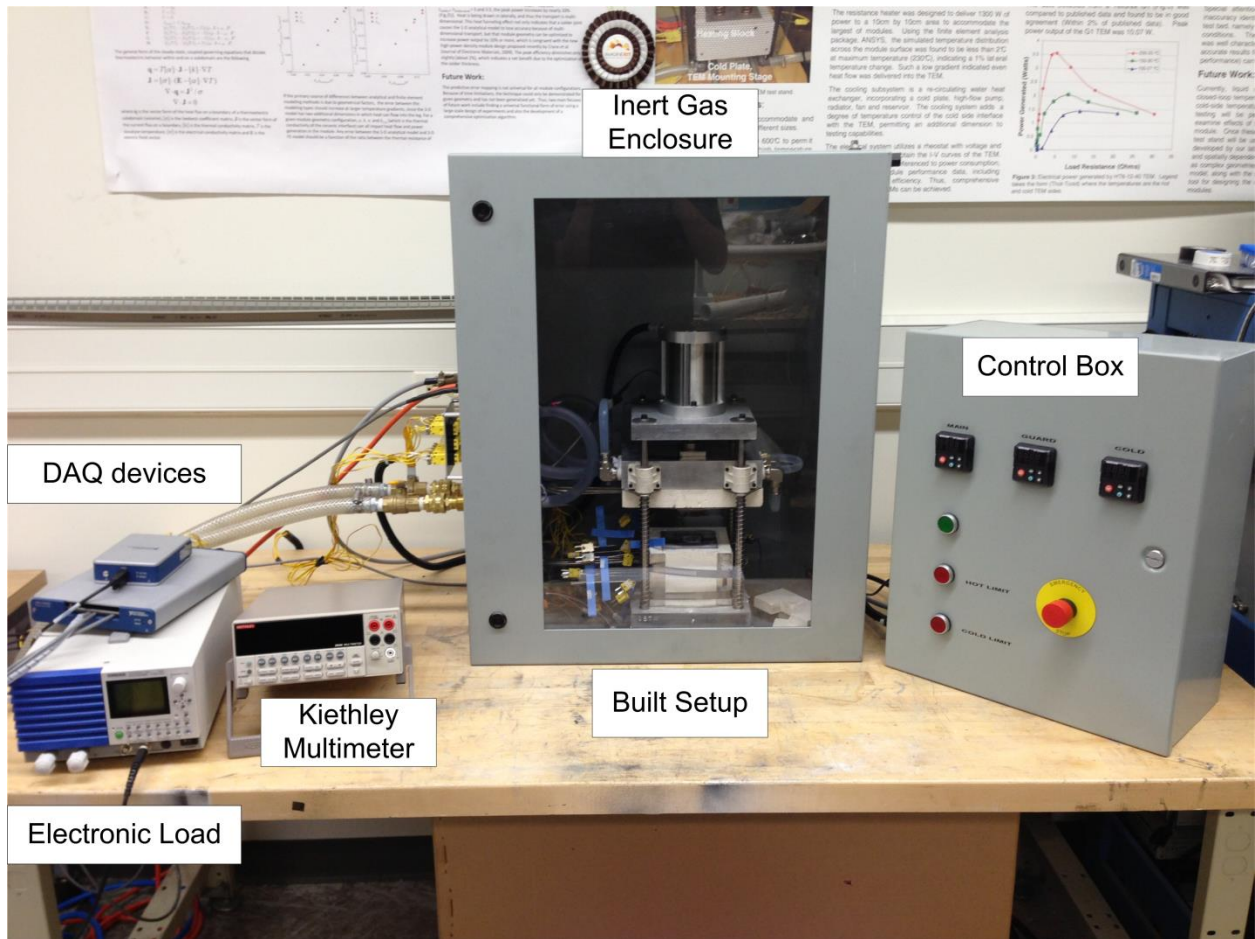
Figure 4.23 - Picture of Completed Setup

Chapter 5.   Validation and Uncertainty

The most important goal of the thesis is to design and develop a test setup to test thermoelectric modules at high temperatures. To determine the legitimacy of the results obtained from the new setup, it is necessary to perform validation and uncertainty analysis. The initial test results show that the testing procedure is repeatable and agrees well with the characterization of a typical BiTe module using a traditional steady-state approach [34]. The heat rate measurement approach was validated at low temperatures by measuring the thermal conductivity of Borofloat glass. Future testing will validate thermal conductivity measurements up to 650°C and incorporate both an inert environment, to avoid oxidization of both the heater blocks, and new high-temperature modules obtained from device developers. What follows is a detailed description of the validation and uncertainty analysis.

5.1 Comparison With the Old Setup

The three module characteristic parameters are plotted as a function of the hot side temperature, as seen in Fig. 5.1. The solid lines are properties measurements using the rapid steady-state approach, while the dotted lines represent the traditional steady-state approach.

When compared with a traditional steady-state approach using the test stand developed by Sandoz-Rosado [34], similar trends were observed. They were also similar to the bulk material trends, as seen in previously published literature. The error bars were set at ±5%; this was the

error in the traditional approach as reported by Sandoz-Rosado [49]. While some discrepancy appeared in the results, this fell within the uncertainty of the measurements. Much of the differences could be due to deviations in the thermal contact resistances. With the Sandoz-Rosado setup, it can be challenging to ensure that the hot heat plate is perfectly parallel with the module, which could introduce slight deviations in the Seebeck and thermal conductance measurements due to deviation in the junction temperatures. Another explanation may lie in the error in estimating the heat losses using the traditional test setup.
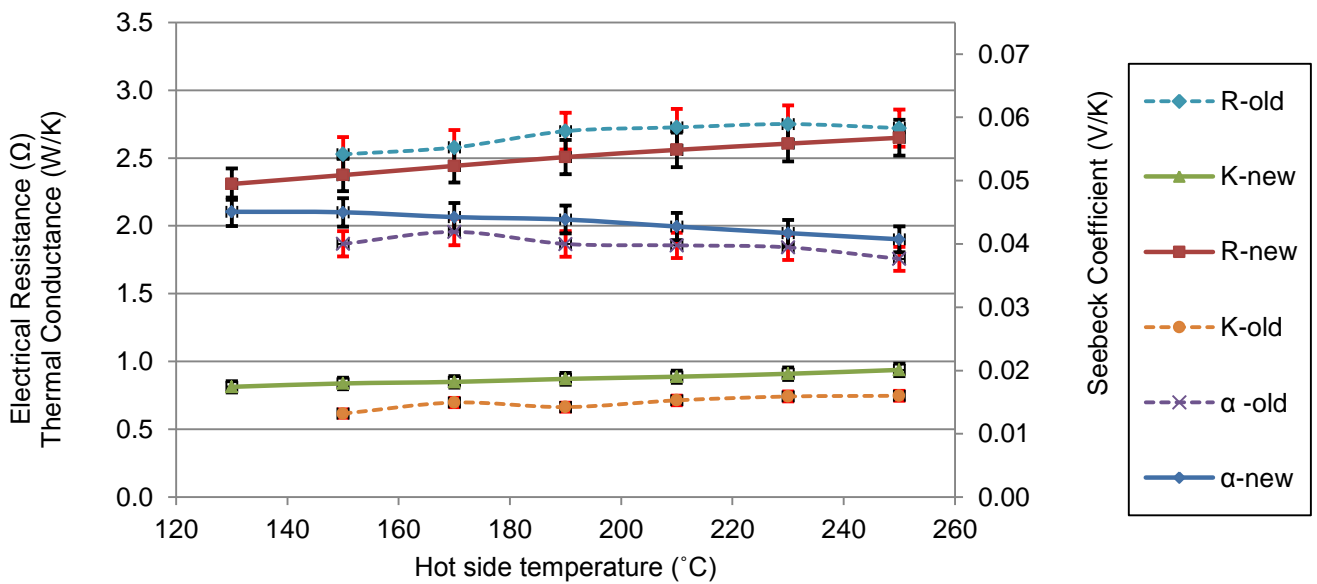
Figure 5.1: Comparison of the characteristic module properties measured by the rapid steady-state approach and the regular steady state approach [34]

5.2 Repeatability Testing

For module testing, a BiTe module (Thermonamic Electronics TEP1-1264-1.5) with 126 leg pairs was used. Tests were conducted at a constant loading pressure of 700kPa with thermal grease on both sides of the module. A series of tests was conducted at a range of temperature differences, starting with the hot side at 130˚C and the cold side at 70˚C. The hot side was then incremented by 20˚C up to a final hot side temperature of 250˚C. The open-circuit voltage (V_{OC})

was recorded when the module reached a steady state at the set temperature. The current-voltage sweep was then applied across the module, and the resulting load voltages were measured. Figure 5.2 is a plot of the power versus the voltage to an open-circuit voltage ratio. The maximum power occurred at approximately half the value of V_{OC}, which corresponds to the predictions of the thermoelectric model used. Figure 5.3 shows the current and voltage values measured at each point.
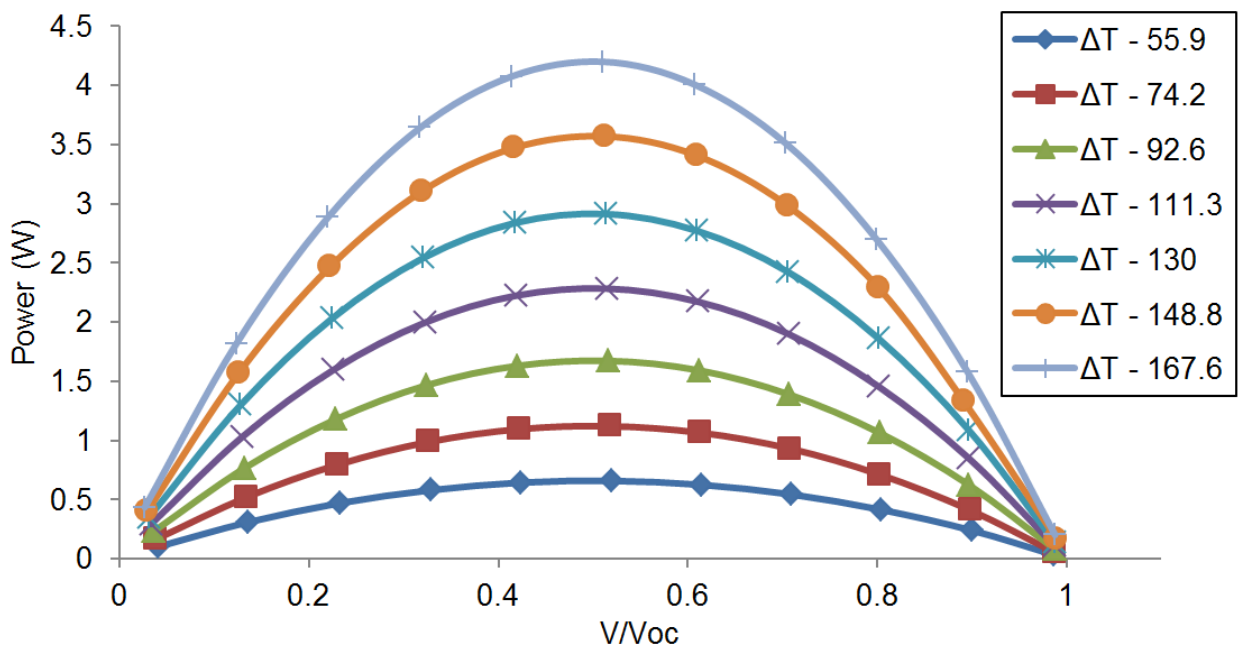
Figure 5.2: Comparison of power output vs. load voltage for different temperature differences

The repeatability tests were carried out on the same module at different days. Between each test, the module was unloaded, cleaned, and loaded again. Cleaning is required to remove any remnants of thermal grease used in the previous experiment. Thermal grease was applied on both sides of the module at the start of every test to reduce any contact resistance between the surfaces.

The tests were repeated on the same module over the entire temperature range multiple times. The standard deviation was calculated at each temperature difference tested and then averaged

for the temperature range. The averaged standard deviation in the calculated properties was at most 1.2%, proving that the approach is highly repeatable.
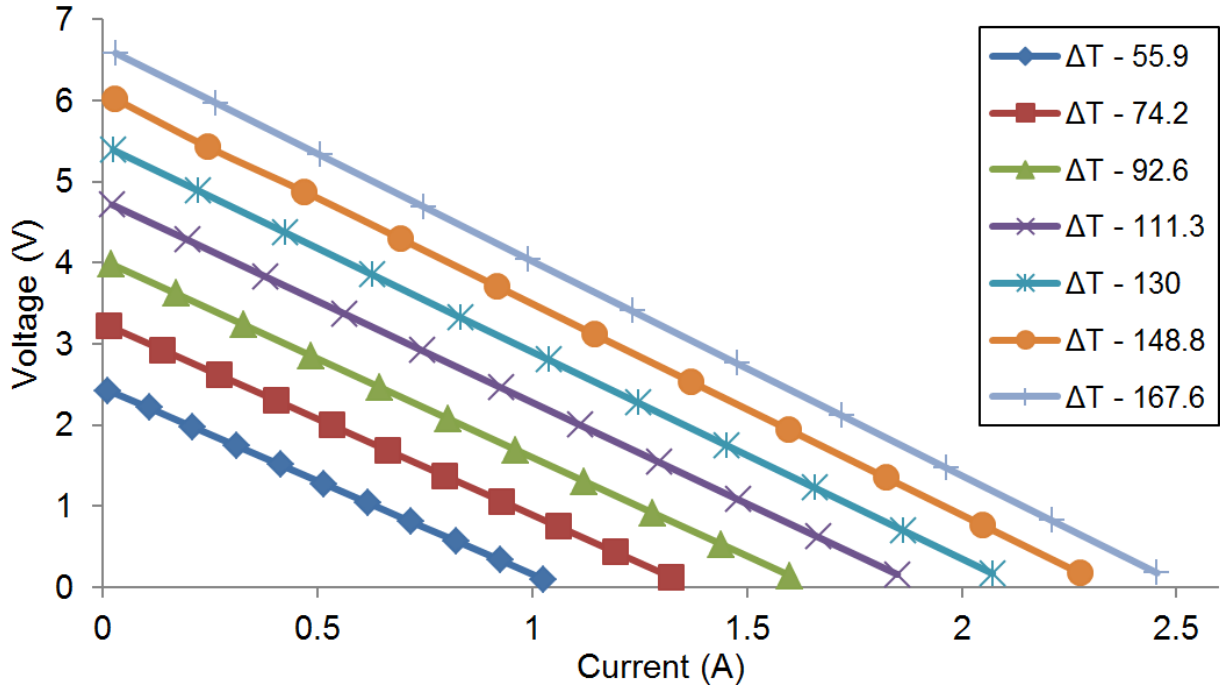
Figure 5.3: Comparison of voltages and current measurements for different temperature differences

5.3 Validation Using Reference Materials

To verify the heat transfer measurements, a reference material with a known conductivity is required. Ideally, the reference material must have a comparable thermal resistance and size of a typical thermoelectric module that might be encountered in the new setup. The reference material must also be able to withstand the range of testing temperatures that might be used. Based on a literature search and NIST recommendations [64], three candidate materials were selected as candidates for validation testing: borosilicate glass (Pyrex® 7740); fused quartz or fused silica; and Pyroceram® 9606 (PC9606) [65,66]. Of these three, only the latter two are suitable for high temperatures, although the borosilicate glass can be used for low-temperature validation. Initial validation was performed with Borofloat® 33, a borosilicate glass, from

SCHOTT North America Inc., because samples were available from the validation of an earlier test stand [34]. Thermal conductivity from the manufacturer was used as a comparison. Fused quartz was selected for future high-temperature validation due to the high cost of Pyroceram® 9606. Manufacturer data from Heraeus Quarzglas GmbH agrees well with published data by Seeman [67] from 500 to 1000K, departing from the data published by Abdulgatov [68] at lower temperatures. Due to this discrepancy among published values, the uncertainty in published values is assumed to be +/–10%.

The Borofloat sample was tested for a range of mean temperatures from 100–160˚C. The tests were conducted by keeping the cold side temperature constant at 70°C and incrementing the hot side temperature by 20°C from 130–250°C. For each temperature difference, the temperature and power measurements were taken after the sample reached a steady state.

The hot side and cold side temperatures were measured using Type K thermocouples inserted just below the surface of the heater blocks. The heat rate was calculated by measuring the heater input power averaged over ten minutes. By keeping a constant load pressure of 700kPa on the sample, all effects due to contact resistance were assumed to be constant for all temperature differences.

Thermal grease was used on both sides of the sample to reduce contact resistance. The test was conducted by applying a fixed temperature difference across the sample, and measuring the heat rate transferred through the sample. Using error analysis on measurements used in calculating the conductivity resulted in an uncertainty of 5%. The results from the experiment were compared to the values available in literature and are found to be in good agreement, as seen in Fig. 5.4. For high-temperature validation, a quartz sample was tested over the entire range of test stand

operating temperatures.

Conductivity Results for Borofloat
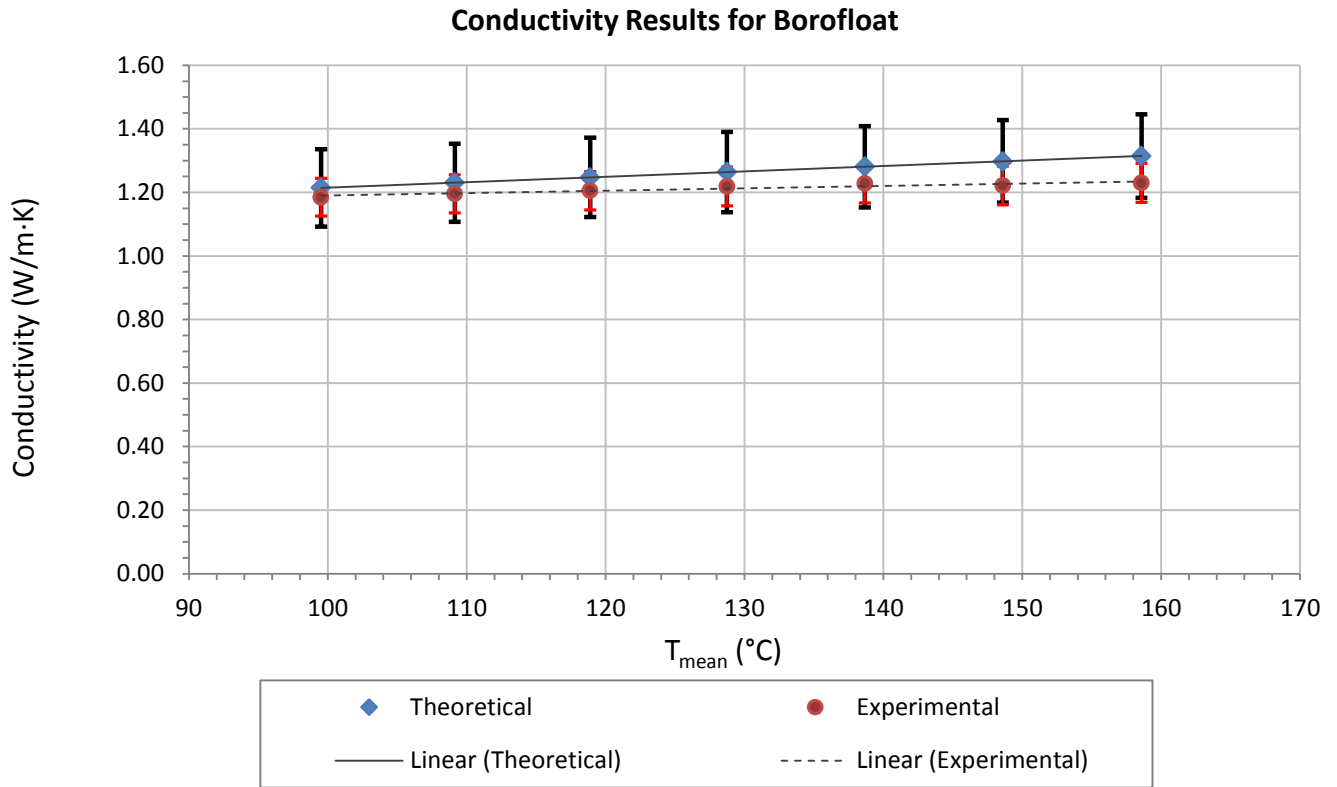
Figure 5.4: Comparison of measured conductivity of borofloat and reference values

High-temperature validation was performed with fused quartz from GM Associates, Inc. Thermal conductivity from the manufacturer was used as a comparison.

The quartz sample was tested for a range of mean temperatures from 125–435°C. The tests were conducted by changing both the hot side and cold side temperatures to ramp the mean temperature. The maximum hot side temperature reached was 650°C, which caused the hot side blocks to start oxidizing. To observe the effect of oxidization on the conductivity results, tests were also carried out as the average temperature was reduced. For each temperature difference, the temperature and power measurements were taken after the sample reached a steady state.

The pressure was kept constant at 700kPa, and power and temperature measurements were taken in the same way as those with the Borofloat. No thermal grease was used, as the grease was rated only up to 300°C. In the future, grafoil sheets should be used to reduce the effect of contact resistance for high-temperature testing.

Using error analysis on the measurements used in calculating the conductivity resulted in an uncertainty of 10%. The increase in uncertainty was mainly due to not accounting for the effect of contact resistance. The results from the experiment were compared to the values available in literature and are found to be in general agreement, as seen in Fig. 5.5.
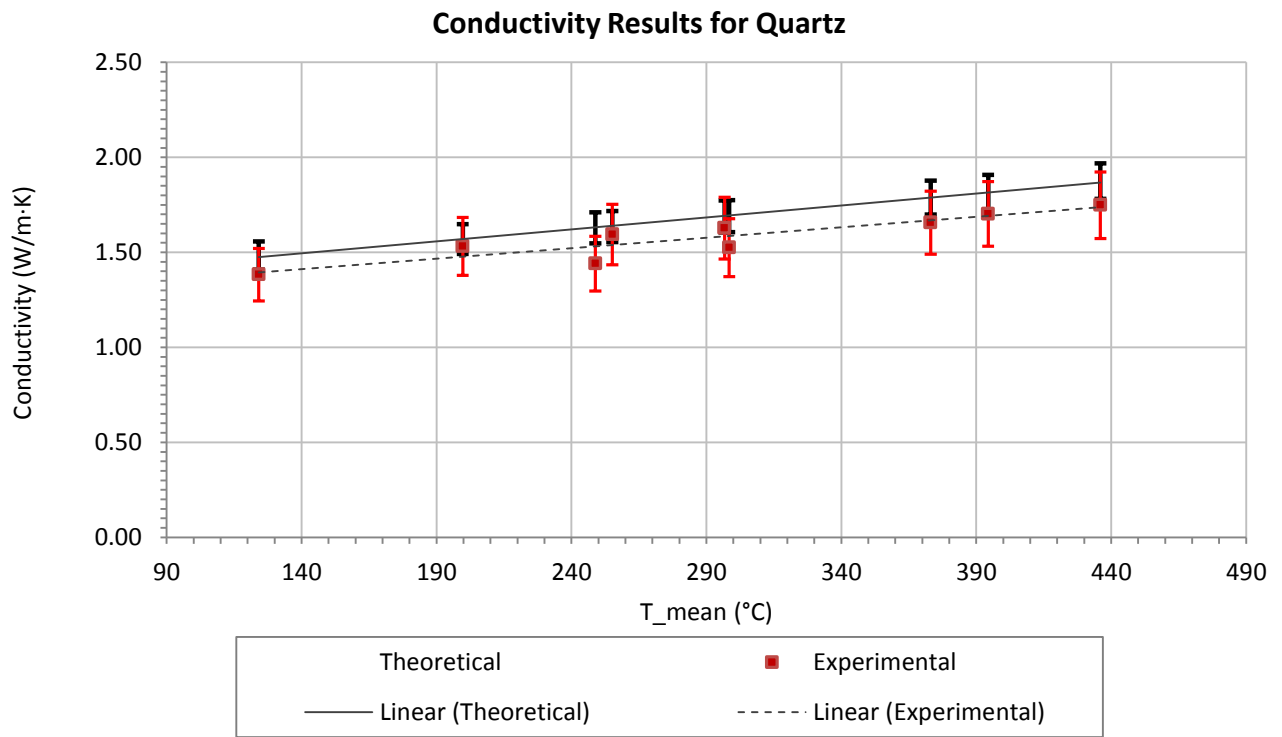

Figure 5.5: Comparison of measured conductivity of quartz glass and reference values

Effects of oxidization on the results are also clear, as the error starts increasing at higher temperatures. These errors continue even as the temperature is reduced. The maximum deviation was observed when the tests were carried out as the heater cooling down from the maximum

temperature. This confirms that the copper had oxidized, and the module was cleaned to remove any oxidized layers.

In conclusion, for quartz the conductivity results were found to be in good agreement up to 400°C, beyond which the copper heater blocks started oxidizing. The effect of oxidization was also observed on cooling, causing large deviations from the theoretical values.

5.4 Uncertainty Analysis

Uncertainty is a non-negative parameter characterizing the dispersion of the values attributed to a measured quantity. In practical testing, no measurement, however carefully made, can be completely free of uncertainties. To reduce errors in measurement, the ability to measure and minimize these uncertainties is extremely important.

The focus of this section is to accurately quantify the uncertainty in measuring the module parameters based on the uncertainties of its constituent measurements. After knowing the uncertainty values, steps can be taken to reduce overall uncertainty in the system. The uncertainty analysis also helps accurately compare two results and differentiate between noise and actual errors.

Measurement uncertainties are classified into two types by the National Institute of Standards and Technology [69]:

- Type A: These include uncertainties due to statistical analysis of data, such as finding the standard deviation of a series of measurements. Type A errors, also known as random errors, can be minimized by increasing the number of measurements.

- Type B: These include uncertainties due to all other factors apart from the measured data, such as calibration data or manufacturer's data. Type B errors, also known as systematic errors, are independent of the number of measurements but can be minimized by calibration of instruments.

To calculate the uncertainty due to random errors, the standard deviation of the mean of the measured set of values is calculated. In its simplest form, the standard deviation of the mean denoted by $(\sigma_{\bar{x}})$ for N readings can be given as

$$\sigma_{\bar{x}} = \frac{1}{\sqrt{N}} \times \sqrt{\frac{1}{N}\sum_{i=1}^{N}(x_i - \bar{x})^2} \qquad (5.1)$$

where $\bar{x}$ is the average value for all terms (x_i) given by $\bar{x} = \frac{\sum x_i}{N}$ $\qquad (5.2)$

The uncertainty due to standard deviation $(\sigma_{\bar{x}})$ can be expressed in percentage as

$$U_{\bar{x}} = \frac{\sigma_{\bar{x}}}{\bar{x}} \qquad (5.3)$$

To calculate uncertainty due to systematic errors, the values of standard deviation are obtained directly from the manufacturer or vendor. These are normally given as an absolute error $(x \pm dx)$ or a percent error $(dx = 5\%)$. The uncertainty can then be calculated by Eqn. (5.3).

The total uncertainty from both Type A and type B components, known as standard uncertainty, can be calculated by the root sum square method as

$$U_{std} = \sqrt{(U_1)^2 + \cdots (U_N)^2} \qquad (5.4)$$

The standard uncertainty calculated in Eqn. (5.4) is calculated at one standard deviation. Assuming that all the readings are normally distributed, this would mean that only 68% of

measurements would lie between $(x \pm \sigma_{\bar{x}})$. To improve the confidence in measurements, the uncertainty can be calculated at $(2\sigma_{\bar{x}})$ or even $(3\sigma_{\bar{x}})$, which would cover 95% or 99% of measurements. To account for this, the standard uncertainty is multiplied by a coverage factor (K). To avoid confusion with thermal conductance, the coverage factor will be noted as (K^*).

In the rapid steady-state approach there are four quantities that are measured: the Seebeck coefficient (α), electrical resistance (R), the thermal conductance (K), and figure of merit (ZT). These are given as

$$\alpha = \frac{V_{OC}}{T_H - T_C} \tag{5.5}$$

$$R = \frac{\Delta V}{\Delta I} \tag{5.6}$$

$$K = \frac{Q_H}{T_H - T_C} \tag{5.7}$$

$$ZT = \frac{\alpha^2 \bar{T}}{RK} \tag{5.8}$$

The current measurement in Eqn. (5.6) is actually calculated using the voltage reading across a shunt resistor .In Eqn. (5.7), the heat rate can be measured as the average product of voltage and current over some time period. Thus, it is observed that in all four parameters, the main measurements are those of temperature and voltage. The focus of this section is on the study of uncertainty measurements of these two measurements, and their effect on the uncertainty of the module parameters.

Voltage measurement

For voltage measurement, the data acquisition device used was a NI–USB 6341. There are three main causes of uncertainty in this measurement:

- Uncertainty due to calibration standard (U_{v1}),

- DAQ uncertainty (U_{v2})

- Random uncertainty in measurements (U_{v3})

Another possible source of error is the potential voltage drop across the wires used for measurements. This is minimized by using smaller-gauge wires.

To minimize (U_{v1}), the voltage measurements were calibrated against a recently factory-calibrated Kiethley 2000 Multimeter. The DAQ calibration was performed accurately, and it is assumed that there is no uncertainty in the calibration. Thus, uncertainty due to calibration can be given as

$$U_{v1} = 0 \tag{5.9}$$

The DAQ uncertainty (U_{v2}) includes errors induced in measurement due to gain error, offset error, and noise uncertainty. These are directly calculated in the manufacturer's manual [70] as $(10 \pm 0.002\text{V})$ for a coverage factor of 3.

$$U_{v2} = 0.02\% \tag{5.10}$$

The random error (U_{v3}) was calculated for open-circuit voltage for 10 tests each on three different days. Equation (5.1) yields an uncertainty of (0.18%) at a coverage factor of 1, so for a range of 10V (U_{v3}) can be written as $(10 \pm 0.054\text{V})$:

$$U_{v3} = 0.54\% \tag{5.11}$$

Using Eqns. (5.8), (5.9), and (5.10) the total uncertainty in voltage U_v was calculated using Eqn. (5.4), which came out to 0.15%:

$$U_v = 0.54\% \hspace{4cm} (5.12)$$

Temperature measurement

For voltage measurement, the data acquisition device used was a NI–USB 9213. The report by Nakos [71] for Sandia National Laboratories gives a detailed account of uncertainties observed in thermocouple measurements. The main causes of uncertainty in this measurement are:

- Thermocouple mounting error (U_{t1})

- Type K thermocouple accuracy (U_{t2})

- Thermocouple connector uncertainty (U_{t3})

- Uncertainty due to the thermocouple extension cable (U_{t4})

- Uncertainty due to the calibration standard (U_{t5})

- DAQ uncertainty (U_{t6})

- Random uncertainty in measurements (U_{t7})

Thermocouple mounting error (U_{t1}) is the error induced when the area to be measured is joined to the thermocouple. Common mounting techniques include the use of thermal grease or soldering, but due to the high test temperatures, both these techniques were incompatible in the setup. Coupling in the setup was achieved by metal contact. The holes drilled for the thermocouples were designed to have a transition fit to enable removal of thermocouples when required and also to ensure good contact. Nakos [71] estimated this error as 0.75% or 2°C with

95% confidence, whichever is higher for all temperatures above 0°C. For an average temperature

of 650°C, the error is 0.75%.

$$U_{t1} = 0.75\% \tag{5.13}$$

The Type-K thermocouple is one of the most commonly used thermocouple types. The National

Institute of Standards and Technology estimated the uncertainty in measurement as 0.75% or

±2.2°C, whichever is higher [72]. For 150°C measurement, the error is 0.75%.

$$U_{t2} = 0.75\% \tag{5.14}$$

The uncertainty due to the connector arises when the material of the connector pins is not exactly

the same as the material of the thermocouple. An example of this would be an extension box

which works with multiple types of thermocouples. The system developed uses one such

extension panel. Nakos [71] estimated this error as ±0.5°C.

$$U_{t3} = 0.3\% \tag{5.15}$$

Uncertainty in the thermocouple cable has the same limitations as the thermocouple. The setup

developed uses a K-type extension cable.

$$U_{t4} = 0.75\% \tag{5.16}$$

To minimize (U_{t5}), the temperature measurements were calibrated using the setup described in

Section 4.6. After calibration, it was assumed

$$U_{t5} = 0 \tag{5.17}$$

The DAQ uncertainty (U_{t6}) includes errors induced in measurement due to gain error, offset error, and noise uncertainty. Using the values from the manufacturer's manual [73], the overall uncertainty was calculated using the formula in the manual as

$$Overall\ accuracy = Range \times Gain\ error + Range \times Offset\ error + \frac{Random\ Noise}{\sqrt{10000}} \times 3$$

(5.18)

The values provided in the manual were a gain error of 0.07%, an offset error of 6μV or 0.008%, and noise of 200nV. All values were at full range (78.125mV). The error due to noise was calculated using a coverage factor of 3 and using 10,000 measurements.

$$U_{t6} = 0.13\%$$ (5.19)

The random error (U_{t7}) was calculated for steady-state conditions for temperature readings at 20°C intervals from 130–250°C. It was found that the random error was the same, regardless of the temperature. The sample size was 4,000 points for each test. Equation (5.1) yields an uncertainty of (0.05%) at a coverage factor of 1, so for a range of 250°C, (U_{t7}) can be written as

$$U_{t7} = 0.15\%$$ (5.20)

Using Eqns. (5.12), (5.13), (5.14), (5.15), (5.16), (5.18), and (5.19) the total uncertainty in voltage U_v was calculated using Eqn. (5.4), which came out to

$$U_t = 1.3\%$$ (5.21)

The uncertainty calculated was for all temperatures above 0°C using the information provided in the NIST standard [72].

Uncertainty in module parameters

1. Seebeck coefficient (α)

The uncertainty analysis of Seebeck coefficient is quite straightforward:

$$U_\alpha = \sqrt{\left(\frac{\partial \alpha}{\partial V_{OC}} U_{V_{OC}}\right)^2 + \left(\frac{\partial \alpha}{\partial T_H} U_{T_H}\right)^2 + \left(\frac{\partial \alpha}{\partial T_C} U_{T_C}\right)^2} \tag{5.22}$$

$$U_\alpha = 1\% \tag{5.23}$$

2. Electrical resistance (R)

In the rapid steady-state approach, the resistance is calculated using the slope of the voltage-current line. To calculate the uncertainty in the slope is slightly complicated. In the test, the module is loaded by stepping through different values of current. These values are assumed to have negligible uncertainty. The line formed by all the points is in the general form

$$y = A + Bx \tag{5.24}$$

where y is the voltage response, A is the y-intercept (V_{OC}), x is the current ,and B is the slope of the line and is the negative of the electrical resistance R.

This is a three-step process. The first step is to calculate the best values of A and B using the co-ordinates of points on the voltage-current line. These can be calculated as

$$A = \frac{\sum x_i^2 \sum y - \sum x \sum xy}{\Delta} \tag{5.25}$$

$$B = \frac{N \sum xy - \sum x \sum y}{\Delta} \tag{5.26}$$

where $\qquad \Delta = N \sum x^2 - \left(\sum x\right)^2 \tag{5.27}$

Step two is to use these values to estimate the uncertainty in y and calculate uncertainty in x:

$$\sigma_y = \sqrt{\frac{1}{N-2}\sum_{i=1}^{N}(y_i - A - Bx_i)^2} \qquad (5.28)$$

$$\sigma_x = B\sqrt{\sum_{j=1}^{M}(x_j - \overline{x})} \qquad (5.30)$$

where $\bar{x}$ is the average value of x when a test is repeated j times. The uncertainty in x is calculated independent of the other points on the line.

The overall uncertainty can be calculated as

$$\sigma_o = \sqrt{\sigma_x^2 + \sigma_y^2} \qquad (5.31)$$

Finally, uncertainties in A and B can be calculated as

$$\sigma_A = \sigma_o\sqrt{\frac{\sum x^2}{\Delta}} \qquad (5.32)$$

$$\sigma_B = \sigma_o\sqrt{\frac{N}{\Delta}} \qquad (5.33)$$

The random uncertainty in electrical resistance (R) was thus calculated as

$$U_{R-r} = 0.8\% \qquad (5.34)$$

The electrical resistance is calculated as

$$R = \frac{\Delta V}{\Delta I} = \frac{V_2 - V_1}{I_2 - I_1} \qquad (5.35)$$

The systematic uncertainty can be calculated as

$$U_{R-s} = \sqrt{\left(\frac{\partial R}{\partial V_2} U_{V_2}\right)^2 + \left(\frac{\partial R}{\partial V_1} U_{V_1}\right)^2 + \left(\frac{\partial R}{\partial I_2} U_{I_2}\right)^2 + \left(\frac{\partial R}{\partial I_1} U_{I_1}\right)^2} \qquad (5.36)$$

Where

$$I_1 = \frac{V_{r1}}{R_{shunt}} \qquad (5.37)$$

$$I_2 = \frac{V_{r2}}{R_{shunt}} \qquad (5.38)$$

Where $R_{shunt} = 50\Omega$ with 1% uncertainty

Thus uncertainty in I_1 and I_2 can be expressed as

$$U_{I_1} = \sqrt{\left(\frac{\partial I_1}{\partial V_{r1}} U_{V_{r1}}\right)^2 + \left(\frac{\partial I_1}{\partial R_{shunt}} U_{R_{shunt}}\right)^2} \qquad (5.39)$$

$$U_{I_2} = \sqrt{\left(\frac{\partial I_1}{\partial V_{r2}} U_{V_{r2}}\right)^2 + \left(\frac{\partial I_2}{\partial R_{shunt}} U_{R_{shunt}}\right)^2} \qquad (5.40)$$

The systematic uncertainty in electrical resistance (U_{R-s}) was thus calculated as

$$U_{R-s} = 1.7\% \qquad (5.41)$$

The overall uncertainty in electrical resistance (U_R) is calculated as

$$U_R = \sqrt{U_{R-r}^2 + U_{R-s}^2} \qquad (5.46)$$

$$U_R = 2\% \qquad (5.40)$$

3. Thermal conductance (K)

The uncertainty in thermal conductance can be separated into two parts: the uncertainty due to instrumentation, and the uncertainty due to heat loss. The power Q_H is calculated as the product of current and voltage. The current is calculated using a 10mΩ shunt resistor with 1% uncertainty. The power equation can be rewritten as

$$K = \frac{\frac{V_p}{R} V}{T_H - T_C} \tag{5.42}$$

where V_p is the voltage across the shunt resister used to measure power. Assuming that the uncertainty in voltage is same,

$$U_{K-r} = \sqrt{\left(\frac{\partial K}{\partial V_p} U_{V_p}\right)^2 + \left(\frac{\partial K}{\partial R} U_R\right)^2 + \left(\frac{\partial K}{\partial V} U_V\right)^2 + \left(\frac{\partial R}{\partial T_H} U_{T_H}\right)^2 + \left(\frac{\partial R}{\partial T_C} U_{T_C}\right)^2} \tag{5.43}$$

Using above calculated values,

$$U_{K-r} = 2.2\% \tag{5.44}$$

From thermal analysis, it was observed that at 650°C, the main heater power loss is around 2%. Assuming no other systematic errors,

$$U_{K-s} = 2\% \tag{5.45}$$

Total uncertainty in thermal conductance can be calculated as

$$U_k = \sqrt{U_{K-r}^2 + U_{K-s}^2} \tag{5.46}$$

$$U_k = 3\% \tag{5.40}$$

In all of the measurements, uncertainties caused due to environmental factors such as temperature, pressure, and humidity were assumed to be negligible. Thus, all of the measured parameters are within the acceptable range of uncertainties for the desired test stand specifications.

In this chapter, the preliminary data was reported and the test stand was validated by measuring the thermal conductivity of known reference materials. Uncertainty analysis was performed to estimate the deviation in values to be expected. Except for the thermal conductance, the preliminary data matches very well with the old setup based on the steady state approach. Similar trends are observed and the values of properties are within the uncertainty limits.

Where the thermal conductance is concerned, the main variation is in the heat rate values. Part of the reason may be because of the fundamental difference in its calculation. The steady state approach uses a passive approach in calculating heat losses by accounting and measuring all the heat losses whereas the "rapid" steady state uses active accounting, where a guard heater arrangement is used to minimize losses. Other reasons that may have caused the variation is the overestimation of the temperature difference in the old setup as well as incorrect calculation of heat losses. Further investigation is required to find out the cause of variation.

To validate the heat rate measurements, a reference material with known thermal conductivity was used. Borofloat was selected as the reference material for low temperatures (up to 250°C) and Quartz was selected for high temperatures (up to 400°C). The temperature was limited due to oxidation of copper. These results were found to match very well with the available literature.

Finally, uncertainty analysis was performed to estimate the standard deviation in the measurements. The resultant values were found to be well within the limits mentioned in the specifications.

Chapter 6.   Conclusion

6.1 Summary of Results

The overall goal of the project was to design and develop a test stand to evaluate properties of high-temperature thermoelectric modules up to 650°C. To achieve this goal, a new testing approach was developed for quick and accurate characterization. Three preliminary setups were also built, based on techniques available in the current literature, to compare issues observed in testing. A novel guard heater arrangement was used to minimize heat losses. To determine the size of the guard heater, a thermal model was developed The test setup was validated by comparing module properties from existing steady state setup as well as measuring thermal conductivity of a reference material. Uncertainty analysis on the measurements confirmed that the setup uncertainty is well within the specifications obtained from industrial partners and laboratories manufacturing modules to be tested.

Preliminary testing was essential to determine the viability of any testing approach at higher temperature. Based on a thorough review of previous published works, three classification of testing approaches are most commonly used; the steady state approach, the Harman approach and the Gao Min approach. For testing a module, researchers favored the steady-state approach, as it is preferable to test a module in actual working conditions. A similar conclusion was obtained from some preliminary experiments, which were carried out at low temperatures. The biggest issue in the steady-state testing was to quantify the exact amount of heat flowing through the module to determine the module's conductance. For high-temperature testing, it was concluded that accurate heat rate measurement would require active accounting of losses.

Active accounting of heat losses usually involves a shielding heater or a radiation shield. The shielding heater or guard heater arrangement consists of a smaller heater surrounded by a larger heater, both of which are maintained at the same temperature. In the literature, the main heater block was made thin so that losses through the sides can be neglected. To account for side losses, the guard heater block designed surrounds the main block on all sides. As both blocks are at the same temperature, there is no heat loss from the main to the guard, effectively ensuring 1-D conduction. Consequently, an important issue in steady-state testing was overcome.

Steady-state testing involves a scan of voltages and currents while a module is loaded with different electrical resistors. At each load point the module should reach a steady state to achieve good results. There is some difficulty in determining whether the module has reached a steady state, especially during the first step, which changes the load from open circuit to short circuit. This also causes long testing times. The new approach developed, called a rapid steady state, is based on the steady state and overcomes all of these issues. This novel approach is a new method, not appearing in the literature.

This rapid steady-state approach uses the same principle as the steady state in calculating the Seebeck coefficient and thermal conductance. The difference lies in measuring the electrical characteristics of the module. In the new method proposed, the module is electrically loaded and unloaded over a very short time span, which avoids the thermal response of the module due to Peltier cooling. By testing with different durations of the load steps, it was observed that the optimum step duration was 10ms. The results were compared and the setup was validated using a known reference material.

Three steps were taken for the validation of the setup. First, the results were tested for repeatability by taking 10 scans each day for three different days. The scans were found to be extremely repeatable and the standard deviation in properties averaged over a temperature range from 130°C to 250°C was 1.2% at most. The second step was to validate the heat rate measurements by calculating the thermal conductivity of a known reference material. Borofloat was selected as a reference material at low temperatures, and quartz at high temperatures. The measured values from both tests were comparable to those found in the literature up to 400°C, beyond which oxidization effects of copper increased the error in measurement. Finally, a detailed uncertainty analysis in measuring the module parameters was conducted. The uncertainties is in values were 1% for the Seebeck coefficient, 2% for electrical resistance, and 3% for thermal conductance.

6.2 Contributions to the Thermoelectric Field

Several contributions were made to the field of thermoelectrics metrology. First and foremost, a new testing approach was developed for testing of thermoelectric modules, called the rapid steady-state method. The new method requires only a short time for testing, overcoming the major drawback of the traditional steady-state approach. It is highly repeatable and is especially useful for long-term testing, as the operating conditions of the module are not disturbed. This versatile method can be used in the testing of both modules and bulk materials.

Additionally, the test setup designed is one of the first to be able to accurately test modules at 650°C. In previously published literature there are several setups that can test for material properties, but the main issue in developing a setup for modules is calculating thermal properties. This issue was overcome by using a novel guard heater arrangement to account for heat losses,

and thus accurately calculate the thermal properties. Another innovation in the test stand is the ability to change the heater size with respect to the module being tested. If the size were kept the same, it would cause large uncertainties in the test stand as the size of the module was reduced. Changing the heater size ensures that there are no losses from the heater even for small sizes of modules.

Furthermore, the test stand can be used for testing using the steady-state approach, the Harman approach, and the Gao Min approach just by making minor adjustments. This is another feature unique to the test stand.

6.3 Suggested Improvements and Future work

Some future work is recommended to resolve the various issues that were observed in developing the first generation of test stand. The most important issue was oxidizing of copper at high temperatures. The stand was built as a first prototype for high temperature testing. To keep material costs low and ease in fabrication, copper was selected as the heater material. With proven oxidation tendencies, using the same material for testing at 650°C will induce large uncertainties. This was also witnessed in module validation using quartz. Aluminum nitride was selected as the best candidate for testing at the full range and should be used in a future version of the test stand now that the copper based system has proven to be highly effective. The second material change suggested would be the insulation material. The material currently selected frequently flakes off if scraped during testing, requiring thorough inspection of the heater surface. If neglected, this can be a cause of large contact resistance between the surfaces. The replacement material selected is 99% pure fused Silica ceramic, which has an even lower thermal conductivity.

To reduce the effect of oxidization of the heater material as well as the thermoelectric module, a design for implementing an inert atmosphere was briefly discussed. Implementation of this design is an important next step required before testing at high temperatures. Enclosing the test stand in a closed box will lead to difficulties in the loading of module. Currently, a hand crank is used to maintain the loading pressure. This has to be moved frequently to account for the changes in pressure due to thermal expansion of the heater materials. A pneumatic loading assembly with external mounted controls is suggested for this purpose. This will enable the test stand to change the loading pressure while enclosed inside the inert gas chamber.

The results from the quartz validation are within accepted limits for temperatures up to 400°C. On incorporating the new heater material and inert gas enclosure, it is recommended to validate the setup using quartz for the full range of temperatures, up to 650°C.

For the guard heater arrangement, the preliminary thermal modeling estimated the heat losses at 650°C to be 2% of the heater power. This needs to be verified experimentally and can be done by changing the temperature difference applied across the module by a small value (ΔT) and observing the change in heater power. This will also help calculate the sensitivity of the setup.

An important component assumed to be negligible in testing is the contact resistance. The current method used to reduce contact resistance is to apply thermal grease. A focused study is required to calculate and minimize the contact resistance between surfaces at higher temperatures, where thermal paste cannot be used.

Finally, the test stand possesses the ability to test modules using different approaches. This has been mentioned briefly as one of the contributions to the field of thermoelectrics. The natural progression of this project would be to test and compare module properties using all of the

methods found in literature. Such a study would help make this test stand a benchmark in module characterization.

Chapter 7.   REFERENCES

[1]   Energy Information Administration, 2011, International Energy Outlook 2011.

[2]   U.S Department of Energy, 2008, Waste Heat Recovery: Technology and Opportunities in U.S. Industry.

[3]   United States Census, 2010, Total Midyear Population for the World.

[4]   Bechtel R., 2010, Multi-Mission Radioisotope Thermoelectric Generator, The National Aeronautics and Space Administration, Cleveland.

[5]   FerroTec, "Advantages of Thermoelectric Cooling" [Online]. Available: http://www.ferrotec.com/Technology/Thermoelectric/Thermalref04.

[6]   Gould C. a., Shammas N. Y. a., Grainger S., and Taylor I., 2011, "Thermoelectric cooling of microelectronic circuits and waste heat electrical power generation in a desktop personal computer," Materials Science and Engineering: B, **176**(4), pp. 316–325.

[7]   Gupta M. P., Sayer M.-H., Mukhopadhyay S., and Kumar S., 2011, "Ultrathin Thermoelectric Devices for On-Chip Peltier Cooling," IEEE Transactions on Components, Packaging and Manufacturing Technology, **1**(9), pp. 1395–1405.

[8]   Sieko, "Sieko World's First" [Online]. Available: http://www.seikowatches.com/heritage/worlds_first.html.

[9]   Kim I., 2000, "BiSb2 TeSe3 - based thin film thermoelectric generators," Materials Letters, **43**(May), pp. 221–224.

[10]   Custom Thermoelectric, "History of Thermoelectrics" [Online]. Available: http://www.customthermoelectric.com/History.html.

[11]   Kanatzidis M., 2009, New Thermoelectric Materials, Argonne National Laboratory, Lemont.

[12]   Tritt T. M., 2001, "Thermoelectric Materials : Principles, Structure, Properties, and Applications," Encyclopedia of Materials: Science and Technology, T.N. K.H.J. Buschow, Ph.D., University of Amsterdam, Van Der Waals-Zeeman Institute, C.U. Robert Cahn, M. Flemings, B. Ilschner, E. Kramer, S. Mahajan, and P. Veyssiere, eds., Elsevier Inc.

[13]   Muto A., 2008, "Device Testing and Characterization of Thermoelectric Nano Composites," MS Thesis, Mechanical Engineering, Massachusetts Institute of Technology.

[14]   Angrist S. W., 1961, "The Direct conversion of heat to electricity by means of a Nernst effect Thermoelectric Generator," PhD Dissertation, Mechanical Engineering Department, Ohio State University.

[15]   Hsu C.-T., Huang G.-Y., Chu H.-S., Yu B., and Yao D.-J., 2011, "Experiments and simulations on low-temperature waste heat harvesting system by thermoelectric power generators," Applied Energy, **88**(4), pp. 1291–1297.

[16]   Gou X., Xiao H., and Yang S., 2010, "Modeling, experimental study and optimization on low-temperature waste heat thermoelectric generator system," Applied Energy, **87**(10), pp. 3131–3136.

[17]   Garimella S., 2012, "Low-grade waste heat recovery for simultaneous chilled and hot water generation," Applied Thermal Engineering, **42**, pp. 191–198.

[18]   Stijepovic M. Z., and Linke P., 2011, "Optimal waste heat recovery and reuse in industrial zones," Energy, **36**(7), pp. 4019–4031.

[19]   Niu X., Yu J., and Wang S., 2009, "Experimental study on low-temperature waste heat thermoelectric generator," Journal of Power Sources, **188**(2), pp. 621–626.

[20]   Chen G., Dresselhaus M. S., Dresselhaus G., Fleurial J.-P., and Caillat T., 2003, "Recent developments in thermoelectric materials," International Materials Reviews, **48**(1), pp. 45–66.

[21]   Minnich A. J., Dresselhaus M. S., Ren Z. F., and Chen G., 2009, "Bulk nanostructured thermoelectric materials: current research and future prospects," Energy & Environmental Science, **2**(5), p. 466.

[22]   Ponnambalam V., Lindsey S., Hickman N. S., and Tritt T. M., 2006, "Sample probe to measure resistivity and thermopower in the temperature range of 300–1000 K," Review of Scientific Instruments, **77**(7), p. 73904.

[23]   Nakama T., Burkov A. T., Heinrich A., Oyoshi T., and Yagasaki K., 1998, Experimental set-up for thermopower and resistivity measurements at 100-1300 K, Ieee.

[24]   Martin J., Tritt T., and Uher C., 2010, "High temperature Seebeck coefficient metrology," Journal of Applied Physics, **108**(12), p. 121101.

[25]   Harman T. C., 1958, "Special Techniques for Measurement of Thermoelectric Properties," Journal of Applied Physics, **29**(9), pp. 1373–1374.

[26]   Buist, Richard J., 1992, "A New Method for Testing Thermoelectric Materials and Devices," 11th International Conference on Thermoelectrics, Arlington, Texas, p. 15.

[27]   Mitrani D., Tomé J. A., Salazar J., Turó A., García M. J., Chávez J. A., and The A., 2005, "Methodology for Extracting Thermoelectric Module Parameters," **54**(4), pp. 1548–1552.

[28]   Fujimoto S., Kaibe H., Sano S., and Kajitani T., 2006, "Development of Transient Measurement Method for investigating Thermoelectric Properties in High Temperature Region," Japanese Journal of Applied Physics, **45**(11), pp. 8805–8809.

[29]   Lau P. G., "Convection correction factor determination for use with the transient test method for thermoelectric modules," Eighteenth International Conference on Thermoelectrics. Proceedings, ICT'99 (Cat. No.99TH8407), pp. 252–255.

[30]   Vazquez J., Palacios R., Sanz-Bobi M. a., and Arenas A., 2003, "Test bench for measuring the electrical properties of commercial thermoelectric modules," Proceedings ICT'03. 22nd International Conference on Thermoelectrics (IEEE Cat. No.03TH8726), pp. 589–593.

[31]   Tanji Y., Nakagawa Y., Kisara K., Yasuoka M., Moriya S., Kumagai T., Niino M., and Sato R., "Electric and thermal contact resistances of the new type thermoelectric module assembled by a screwing method," Eighteenth International Conference on Thermoelectrics. Proceedings, ICT'99 (Cat. No.99TH8407), (1 999), pp. 260–265.

[32]   Hsu C.-T., Huang G.-Y., Chu H.-S., Yu B., and Yao D.-J., 2011, "An effective Seebeck coefficient obtained by experimental results of a thermoelectric generator module," Applied Energy, **88**(12), pp. 5173–5179.

[33]   Anatychuk L. I., and Havrylyuk M. V., 2011, "Procedure and Equipment for Measuring Parameters of Thermoelectric Generator Modules," Journal of Electronic Materials, **40**(5), pp. 1292–1297.

[34]   Sandoz-Rosado E., and Stevens R. J., 2009, "Experimental Characterization of Thermoelectric Modules and Comparison with Theoretical Models for Power Generation," Journal of Electronic Materials, **38**(7), pp. 1239–1244.

[35]   Muto a, Kraemer D., Hao Q., Ren Z. F., and Chen G., 2009, "Thermoelectric properties and efficiency measurements under large temperature differences.," The Review of scientific instruments, **80**(9), p. 093901.

[36]   Rauscher L., Kaibe H. T., Ishimabushi H., Sano S., Muller E. W., and Platzek D., 2003, "New approach for highly accurate efficiency determination of thermoelectric generator modules," Proceedings ICT'03. 22nd International Conference on Thermoelectrics (IEEE Cat. No.03TH8726), pp. 508–511.

[37]   Rauscher L., Fujimoto S., Kaibe H. T., and Sano S., 2005, "Efficiency determination and general characterization of thermoelectric generators using an absolute measurement of the heat flow," Measurement Science and Technology, **16**(5), pp. 1054–1060.

[38]   Takazawa H., Obara H., Okada Y., Kobayashi K., Onishi T., and Kajikawa T., 2006, "Efficiency measurement of thermoelectric modules operating in the temperature difference of up to 550K," 2006 25th International Conference on Thermoelectrics, pp. 189–192.

[39]   Min G., and Rowe D. M., 2001, "A novel principle allowing rapid and accurate measurement of a dimensionless thermoelectric figure of merit," Measurement Science and Technology, **12**(8), pp. 1261–1262.

[40]   Min G., Rowe D. M., and Kontostavlakis K., 2004, "Thermoelectric figure-of-merit under large temperature differences," Journal of Physics D: Applied Physics, **37**(8), pp. 1301–1304.

[41]   Min G., 2010, "ZT Measurements Under Large Temperature Differences," Journal of Electronic Materials, **39**(9), pp. 1782–1785.

[42]   Middleton A. E., and Scanlon W. W., 1953, "Measurement of the Thermoelectric Power of Germanium at Temperatures above 78°K," Physical Review, **92**(2), pp. 219–226.

[43]   Sharath Chandra L. S., Lakhani A., Jain D., Pandya S., Vishwakarma P. N., Gangrade M., and Ganesan V., 2008, "Simple and precise thermoelectric power measurement setup for different environments.," The Review of scientific instruments, **79**(10), p. 103907.

[44]   Paul B., 2011, "Simple apparatus for the multipurpose measurements of different thermoelectric parameters," Measurement.

[45]   Ahiska R., and Ahiska K., 2010, "New method for investigation of parameters of real thermoelectric modules," Energy Conversion and Management, **51**(2), pp. 338–345.

[46]   Ciylan B., and Yilmaz S., 2007, "Design of a thermoelectric module test system using a novel test method," International Journal of Thermal Sciences, **46**(7), pp. 717–725.

[47]   Iwasaki H., Yokoyama S., Tsukui T., Koyano M., Hori H., and Sano S., 2003, "Evaluation of the Figure of Merit of Thermoelectric Modules by Harman Method," Japanese Journal of Applied Physics, **42**(Part 1, No. 6A), pp. 3707–3708.

[48]   Iwanaga S., Toberer E. S., LaLonde A., and Snyder G. J., 2011, "A high temperature apparatus for measurement of the Seebeck coefficient.," The Review of Scientific Instruments, **82**(6), p. 063905.

[49]   Sandoz-Rosado E. J., 2009, "Investigation and Development of Advanced Models of Thermoelectric Generators for Power Generation Applications," Rochester Institute of Technology.

[50]   Buist, Richard J., 1995, "Methodology for Testing Thermoelectric Materials and Devices," CRC Handbook of Thermoelectrics, pp. 189–209.

[51]   Rowe D. M., 2006, Thermoelectric s Handbook: Macro to nano, CRC/Taylor & Francis.

[52]   Taylor J. R., 1997, An Introduction to Error Analysis, University Science Books, Sasalito, California.

[53]   Ferrotec Coorporation, "Photoveel II and Photoveel II-S - Machinable Nitride Ceramics" [Online]. Available: http://www.ferrotec.com/products/ceramics/machineable/nitride/.

[54]   Slack G. A., 1987, "The Intrinsic Thermal Conductivity of AIN," Journal of Physics and Chemistry of Solids, **48**(7), pp. 641–647.

[55]   Edgar J. H., Gu Z., Taggart K., Chaudhuri J., Nyakiti L., Lee R. G., and Witt R., 2006, "Oxidation of Aluminum Nitride for Defect Characterization," Material Research Society Meeting, **892**, pp. 1–6.

[56]   Zhu Y., Mimura K., and Isshiki M., 2002, "Oxidation Mechanism of Copper at 623-1073 K.," Materials Transactions, **43**(9), pp. 2173–2176.

[57]   Haugsrud R., 2003, "On the high-temperature oxidation of nickel," Corrosion Science, **45**(1), pp. 211–235.

[58]   Lavrenko V. A., and Alexeev A. F., 1986, "High-temperature oxidation of boron nitride," Ceramics International, **12**(1), pp. 25–31.

[59]   Miller, Warren J., 1972, "High Temperature oxidation of Silicon Carbide," Air Force Institute of echnology.

[60]   Gulbransen E. A., Andrew K. F., and Brassart F. A., 1963, "Oxidation of Molybdenum 550°C to 1700°C," Journal of the Electrochemical Society, **110**(9), pp. 952–959.

[61]   Guha A., 1982, "Properties of CuBe C17510 for High Conductivity Applications," Stillwater, Oklahoma.

[62]   Park J.-H., and Natesan K., 1993, "Oxidation of copper and electronic transport in copper oxides," Oxidation of Metals, **39**(5-6), pp. 411–435.

[63]   Kiethley, 2002, Model 2000 DMM.

[64]   Flynn D. ., 2013, "Thermophysics consultant, National Institute of Standards and Technology, USA.", Private Communication

[65]   Müller E., Stiewe C., Rowe D., and Williams S., 2006, "Precision Thermal Conductivity Measurements of materials," Thermoelectrics Handbook Macro to Nano, pp. 26–8 – 26–9.

[66]   Buzovkina T., and Men' A., 1972, "Use of fused quartz as a reference standard in comparative methods of thermal conductivity measurements," Journal of Engineering Physics.

[67]   Seemann H. E., 1928, "The Thermal and Electrical Conductivity of Fused Quartz as a Function of Temperature," Physical Review, **31**(1), pp. 119–129.

[68]   Abdulagatov I. M., Emirov S. N., Tsomaeva T. A., Gairbekov K. . A., Askerov S. Y. Y., and Magomedova N. A., 2000, "Thermal conductivity of fused quartz and quartz ceramic at high temperatures and high pressures," Journal of Physics and Chemistry of Solids, **61**(5), pp. 779–787.

[69]   Taylor B. N., and Kuyatt C. E., 1994, Guidelines for Evaluating and Expressing the Uncertainty of NIST Measurement Results, Physics Laboratory, National Institute of Standards and Technology, Gaithersburg, MD.

[70]   National Instruments, 2013, NI 6341/6343 Specifications.

[71]   Nakos J. T., 2004, Uncertainty Analysis of Thermocouple Measurements Used in Normal and Abnormal Thermal Environment Experiments at Sandia's Radiant Heat Facility and Lurance Canyon Burn Site, Sandia National Laboratories, Albuquerque, New Mexico.

[72]   Nationa Institute of Standards and Technology, 2011, Type K thermocouple reference Table, N.I.S.T.

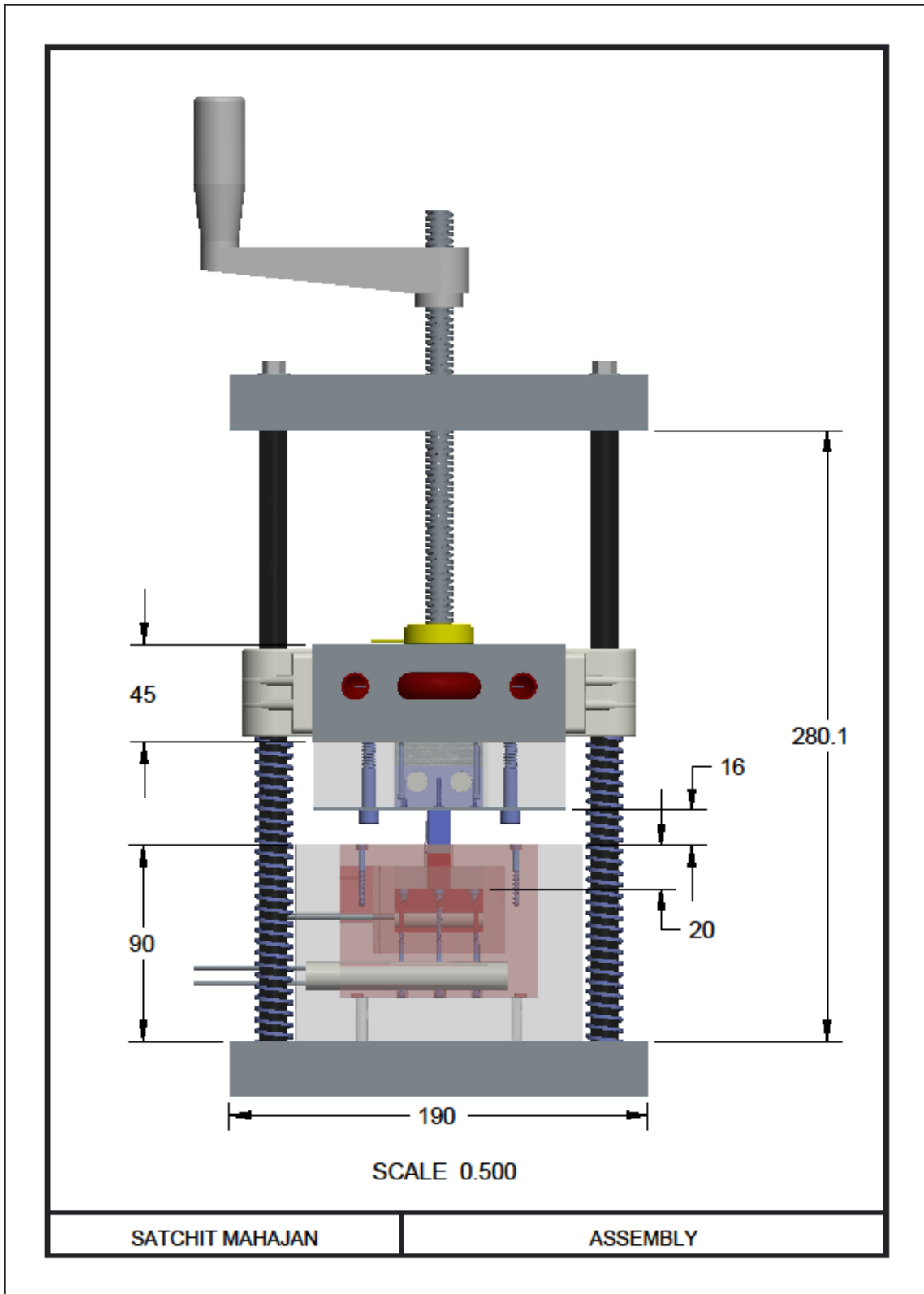[73]   National Instruments, 2013, NI USB 9213 Manual, National Instruments.

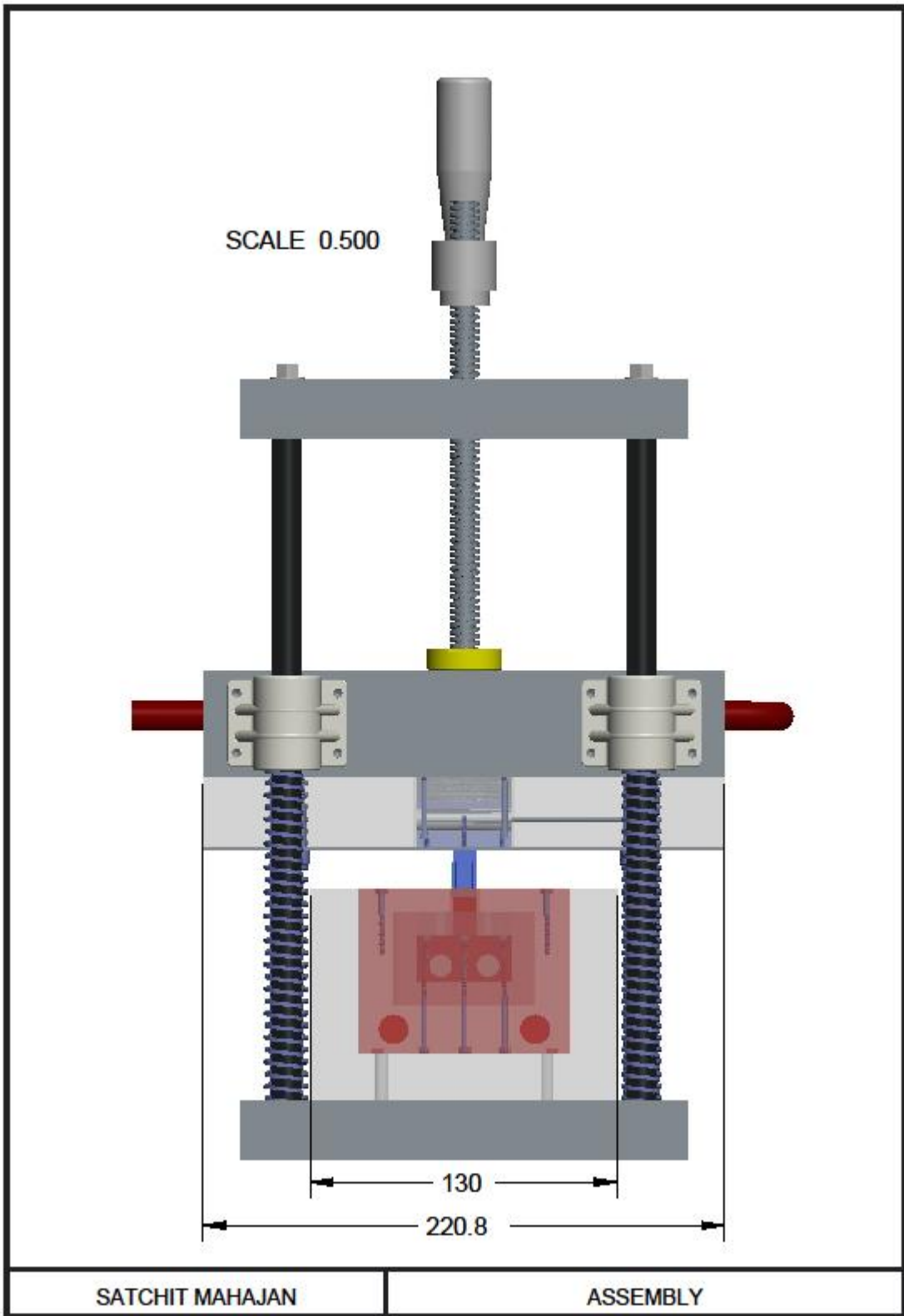# Appendix A

Test Procedure:

The test begins by cleaning the thermal grease on the module from the previous test as well as cleaning the surfaces of the heaters. On a clean module, a new layer of thermal grease is applied. The module is placed on the main heater block and the cold side assembly is lowered with the help of a lead screw. When the system will be placed in an inert environment, the lowering will be performed with the help of a pneumatic cylinder. The lead screw rests on top of a load cell which measures the applied pressure. Two pieces of insulation are then slid into position to reduce heat loss.

Once optimal loading pressure is reached, the chiller is turned on. This controls the temperature of the cold plate and removes heat dumped by the system. Using the VI created in LABVIEW, the temperatures for main heater block, guard heater block and the cold side heater block are set. The temperatures for the main and cold heater blocks are set as values in Celsius, whereas the guard heater block temperature is set as a difference with respect to the main heater temperature.

The entire setup takes about 30 minutes to reach steady state. Once the system reaches the set temperatures, a scan is performed and the data is recorded and exported to Excel. Post processing converts this data into required parameters.
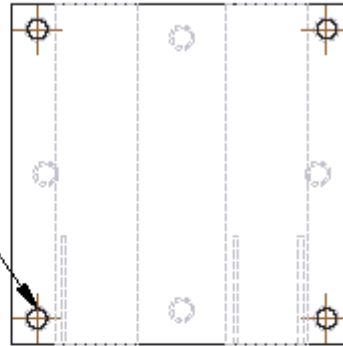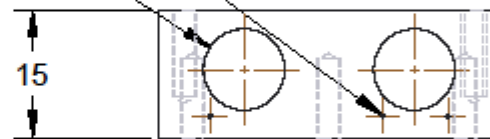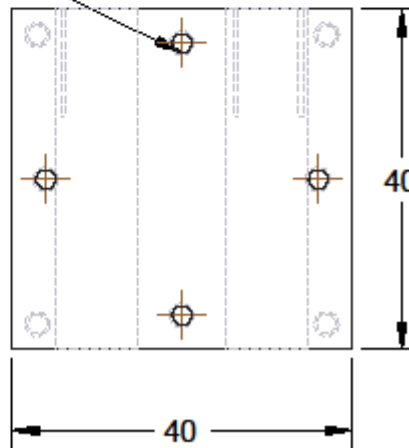
Appendix B

SCALE 0.500

| SATCHIT MAHAJAN | ASSEMBLY |

SCALE 0.500

130

220.8

SATCHIT MAHAJAN

ASSEMBLY

SCALE 0.750

90

90

90

Ø 5.11

4-40
UNC - 2B
Drill #43 DRILL
(2.261)   THRU
-(1) HOLE

2x Ø 12.7 THRU
2x Ø 1.52 ⊽ 0.787

38.1

15

90

60

50

25.4

3.18

60

60

R3.18

SATCHIT MAHAJAN   GUARD HEATER
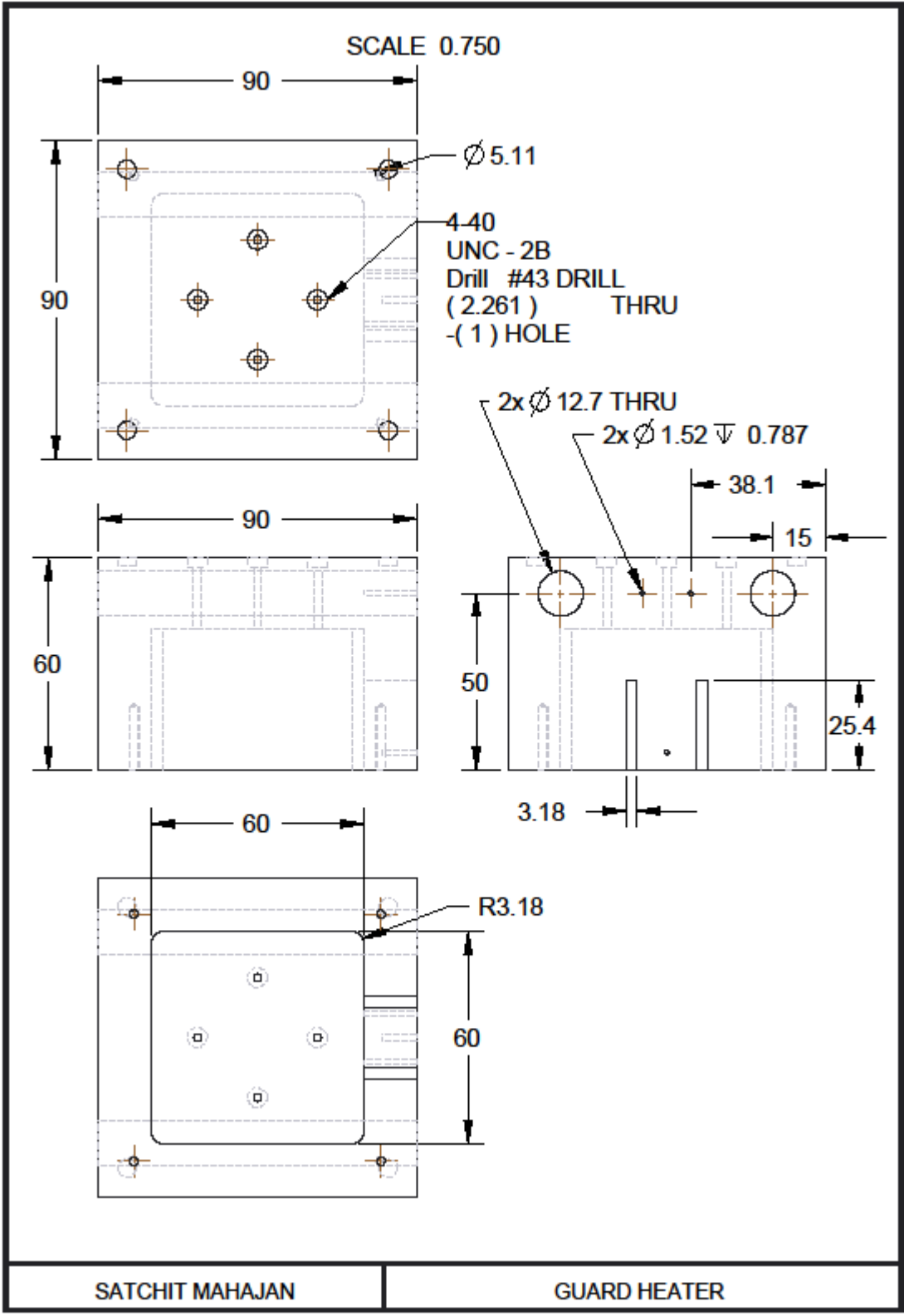
4-40
UNC - 2B TAP
⊽ 10.280 #43
DRILL (2.261) ⊽
10.280 -(4) HOLE

3X Ø 0.51 ⊽ 12.7

2X Ø 9.53 THRU

15

4-40
UNC - 2B TAP
⊽ 9.250 #43 DRILL
(2.261) ⊽ 9.250
-(4) HOLE

40

40

SCALE 1.500

| SATCHIT MAHAJAN | MAIN HEATER BLOCK |

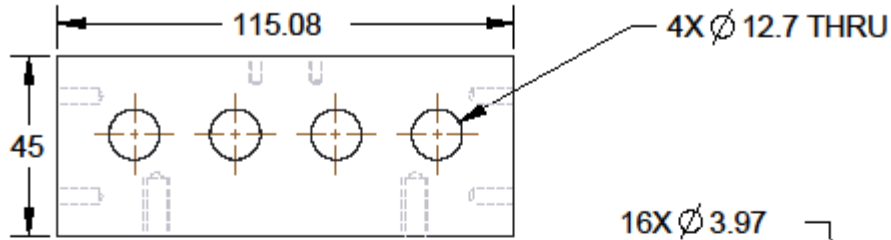4-40
UNC - 2B TAP
THRU #43 DRILL (
2.261) THRU -(4)
HOLE

10

10

40

40

SCALE 1.500

40

5

16
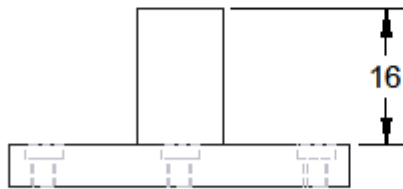
| SATCHIT MAHAJAN | HEIGHT EXTESNTION |

SCALE 0.700

115.08

45

4X Ø 12.7 THRU

16X Ø 3.97

1/4-20 UNC -
2B TAP ⊽ 14.450 #7 DRILL (5.105
) ⊽ 14.450 -(1) HOLE

220.8

SATCHIT MAHAJAN	CHILLER